

การประเมินการใช้ไวรัสไลน์ฟอร์มเช็ชเตอร์ในแหล่งกักเก็บก๊าซธรรมชาติเหลว



นาย วิสุทธิ์ โชคนาคะวโร

ศูนย์วิทยทรัพยากร
จุฬาลงกรณ์มหาวิทยาลัย

วิทยานิพนธ์นี้เป็นส่วนหนึ่งของการศึกษาตามหลักสูตรปริญญาวิศวกรรมศาสตรมหาบัณฑิต

สาขาวิชาวิศวกรรมปิโตรเลียม ภาควิชาวิศวกรรมเหมืองแร่และปิโตรเลียม

คณะวิศวกรรมศาสตร์ จุฬาลงกรณ์มหาวิทยาลัย

ปีการศึกษา 2553

ลิขสิทธิ์ของจุฬาลงกรณ์มหาวิทยาลัย

EVALUATION OF WIRELINE FORMATION TESTER IN GAS CONDENSATE
RESERVOIR



Mr. Wisut Choknakawaro

ศูนย์วิทยทรัพยากร
จุฬาลงกรณ์มหาวิทยาลัย
A Thesis Submitted in Partial Fulfillment of the Requirements
for the Degree of Master of Engineering Program in Petroleum Engineering

Department of Mining and Petroleum Engineering

Faculty of Engineering

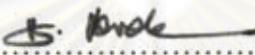
Chulalongkorn University

Academic Year 2010


Copyright of Chulalongkorn University


Thesis Title EVALUATION OF WIRELINE FORMATION
TESTER IN GAS CONDENSATE RESERVOIR
By Mr. Wisut Choknakawaro
Field of Study Petroleum Engineering
Thesis Advisor Assistant Professor Suwat Athichanagorn, Ph.D.
Thesis Co-Advisor Saifon (Daungkaew) Sirimongkolkitti, Ph.D.

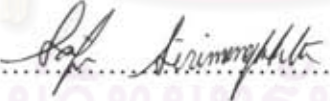
Accepted by the Faculty of Engineering, Chulalongkorn University in
Partial Fulfillment of the Requirements for the Master's Degree


..... Dean of the Faculty of Engineering
(Associate Professor Boonsom Lerdkhironwong, Dr.Ing.)

THESIS COMMITTEE


..... Chairman
(Associate Professor Sarithdej Pathanasetpong)


..... Thesis Advisor
(Assistant Professor Suwat Athichanagorn, Ph.D.)


..... Thesis Co-Advisor
(Saifon (Daungkaew) Sirimongkolkitti, Ph.D.)


..... External Examiner
(Witsarut Thungsuntonkhun, Ph.D.)

วิสุทธิ์ โชคนาคะวโร : การประเมินการใช้ไวร์ไลน์ฟอร์มชันทดสอบในแหล่งกักเก็บก๊าซธรรมชาติเหลว (EVALUATION OF WIRELINE FORMATION TESTER IN GAS CONDENSATE RESERVOIR) อ. ที่ปรึกษาวิทยานิพนธ์หลัก: ผศ. ดร. สุวัฒน์ อธิษนากร, อ. ที่ปรึกษาวิทยานิพนธ์ร่วม: ดร. สายฝน (ดวงแก้ว) สิริมังคลกิติ, 164 หน้า.

ในปัจจุบัน มีงานวิจัยมากมายที่ทำการศึกษาพฤติกรรมของความดันจากการทดสอบหลุมในแหล่งกักเก็บก๊าซธรรมชาติเหลว อย่างไรก็ตามยังไม่มีรายงานว่ากราฟการเปลี่ยนแปลงความดันที่ได้จากการทำไวร์ไลน์ฟอร์มชันทดสอบสามารถตรวจสอบก๊าซธรรมชาติเหลวรอบๆหลุมได้ งานวิจัยนี้ทำการศึกษาผลกระทบของก๊าซธรรมชาติเหลวต่อพฤติกรรมของความดันจากการทำไวร์ไลน์ฟอร์มชันทดสอบในแหล่งกักเก็บก๊าซธรรมชาติเหลว โดยใช้การสร้างแบบจำลองของแหล่งกักเก็บแบบชั้นเดียวที่เป็นเนื้อเดียวกันของก๊าซธรรมชาติเหลวเพื่อคำนวณค่าความดันที่ได้จากการทำไวร์ไลน์ฟอร์มชันทดสอบ จากนั้น ใช้โปรแกรมประเมินค่าจากการทำทดสอบหลุมมาประยุกต์ใช้ในการประเมินค่าคุณสมบัติของชั้นหิน กรณีศึกษาเบื้องต้น เป็นการศึกษาโดยใช้แบบจำลองของแหล่งกักเก็บชั้นเดียวที่เป็นเนื้อเดียวกันของก๊าซธรรมชาติเหลวแบบเบ้า ทำการศึกษาพฤติกรรมของความดันระหว่างผลิตและระหว่างปิดหลุมผลิตทั้งแบบที่ความดันระหว่างผลิตมีค่าสูงกว่าและต่ำกว่าความดันที่จุดน้ำค้าง จากนั้นทำการศึกษาแหล่งกักเก็บชั้นเดียวที่เป็นเนื้อเดียวกันของก๊าซธรรมชาติเหลว โดยศึกษาผลกระทบของอัตราการผลิตในการทดสอบหลุม องค์ประกอบเริ่มต้นของของไหลระยะเวลาของการทดสอบหลุม ขนาดของเครื่องมือทดสอบความดัน ตำแหน่งของอุปกรณ์ในการเก็บข้อมูล ความดันเริ่มต้นของแหล่งกักเก็บ อัตราส่วนของค่าความชื้นได้ของหินในแนวตั้งต่อแนวนอน และค่าความสามารถในการซึมผ่านของของไหลในชั้นหินในแนวนอน ทั้งนี้จากการศึกษาทั้งหมด เพื่อประเมินว่าค่าคุณสมบัติต่างๆ ที่ได้จากการทำไวร์ไลน์ฟอร์มชันทดสอบในแหล่งกักเก็บก๊าซธรรมชาติเหลวนั้นสามารถให้ค่าที่ยอมรับได้ ณ สภาวะการผลิตบ้าง ภายใต้ข้อจำกัดของอุปกรณ์

ภาควิชา วิศวกรรมเหมืองแร่และปิโตรเลียม..... ลายมือชื่อนิสิต..... วิสุทธิ์ โชคนาคะวโร
สาขาวิชา วิศวกรรมปิโตรเลียม..... ลายมือชื่อ.ที่ปรึกษาวิทยานิพนธ์หลัก..... สุวัฒน์ อธิษนากร
ปีการศึกษา 2553..... ลายมือชื่อ.ที่ปรึกษาวิทยานิพนธ์ร่วม..... สายฝน (ดวงแก้ว) สิริมังคลกิติ

5171616821: MAJOR PETROLEUM ENGINEERING

KEYWORDS: PERMEABILITY / WIRELINE FORMATION TEST / GAS
CONDENSATE / CONDENSATE BANK

WISUT CHOKNAKAWARO : EVALUATION OF WIRELINE
FORMATION TESTER IN GAS CONDENSATE RESERVOIR. THESIS
ADVISOR: ASSISTANT PROFESSOR SUWAT ATHICHANAGORN,
Ph.D., THESIS CO-ADVISOR : SAIFON (DAUNGKAEW)
SIRIMONGKOLKITTI, Ph.D., 164 pp.

Currently, the pressure behavior study from well tests in gas condensate reservoir has been the subject of much research. However, it has not been reported that the pressure derivative from wireline formation test is used to detect condensate drop-out around wellbore. This study aims to investigate the effect of condensate drop-out on pressure transient data obtained from wireline formation test in gas condensate reservoir. A reservoir simulator was used to determine pressure responses from wireline formation tests for single layer homogeneous gas condensate reservoir. Then, the pressure transient analysis software was used to estimate reservoir parameters. A single layer homogeneous reservoir with lean gas condensate fluid was used as a base case to investigate the pressure and phase behavior during drawdown and build-up period when the flowing pressure is above and below the dew point pressure. After that, a single layer is investigated for the effects of drawdown rate, initial fluid composition, test duration, probe size, probe position, initial reservoir pressure, permeability anisotropy and horizontal permeability on the pressure behavior. All the investigations were performed to determine whether the results from WFT conducted in gas condensate reservoir can provide satisfactory information under different reservoir scenarios and tool limitation. The results show that with certain conditions, the condensate bank effect can be recognized as a spherical composite behavior on the pressure derivative obtained from WFT.

Department: Mining and Petroleum Engineering.... Student's signature: *Wisut Choknakawaro*
Field of study: Petroleum Engineering..... Advisor's signature: *Suwat Athichanagorn*
Academic Year: 2010..... Co-Advisor's signature: *Saifon Sirimongkolkitti*

Acknowledgements

I would like to express my appreciation toward Assistant Professor Dr. Suwat Athichanagorn, my advisor, for his guidance, advice, and encouragement throughout the course of the study. I am also grateful to Dr. Saifon (Daungkaew) Sirimongkolkitti, Reservoir Domain Champion (Schlumberger BMP.), my co-advisor, for creative suggestion and invaluable advice.

I would like to thank Schlumberger Overseas S.A. (Thailand) for providing me with the opportunity to use simulation software (ECLIPSE) and interpretation software (Saphir) through internship period, especially all DCS, Data Consulting Services section, staffs for your warm welcome and your support.

I would like to thank the thesis committee members for their comments and recommendations.

I would like to thank all faculty members in the Department of Mining and Petroleum Engineering who have offered petroleum knowledge, technical advice, and invaluable consultation.

Last, but not least, I am very grateful to my parents, Supphachok and Boonnom Choknakawaro, for their endless love, patient, encouragement and support.

ศูนย์วิทยทรัพยากร
จุฬาลงกรณ์มหาวิทยาลัย

Contents

	Page
Abstract (in Thai).....	iv
Abstract (in English).....	v
Contents.....	vii
List of Tables.....	ix
List of Figures.....	xi
List of Abbreviations.....	xviii
Nomenclature.....	xx
CHAPTER	
I. INTRODUCTION.....	1
1.1 Outline of Methodology.....	2
1.2 Thesis Outline.....	3
II. LITERATURE REVIEW.....	4
2.1 Well Test in Gas Condensate Reservoirs.....	4
2.2 Wireline Formation Test (WFT).....	6
III. THEORY AND CONCEPT.....	10
3.1 Basic Well Test Interpretation.....	10
3.1.1 Transient Flow Equation.....	12
3.1.2 The Derivative Plot.....	13
3.2 Wireline Formation Test.....	14
3.2.1 Wireline Formation Test Procedure.....	15
3.2.2 Wireline Formation Test Interpretation.....	18
3.2.3 Wireline Formation Test Flow Regimes.....	19
3.2.4 Wireline Formation Test Tools.....	24
3.3 Gas Condensate Reservoirs.....	32
3.3.1 Gas Condensate Phase Behavior.....	33
3.3.2 Compositions Changes when Condensate Drop-out.....	35

3.3.3	Condensate Banking.....	36
IV. SIMULATION RESERVOIR MODEL.....		40
V. SIMULATION RESULT AND ANALYSIS.....		48
5.1	Behavior above Dew Point Pressure (Model Validation).....	48
5.2	Behavior below Dew Point Pressure.....	52
5.2.1	Phase Behavior during Drawdown Period.....	58
5.2.2	Phase Behavior during Build-up Period.....	62
5.3	Effects of Drawdown Rate.....	64
5.4	Effects of Initial fluid Composition.....	70
5.5	Effects of Test Duration.....	78
5.6	Effects of Probe Size.....	84
5.7	Effects of Probe Position.....	87
5.8	Effects of Permeability anisotropy.....	90
5.9	Effects of Absolute Permeability.....	93
5.10	Effects of Initial Reservoir Pressure.....	97
VI. CONCLUSIONS AND RECOMMENDATIONS.....		101
6.1	Conclusions.....	101
6.2	Recommendations.....	103
References.....		104
Appendices.....		111
Vitae.....		164

List of Tables

	Page
Table 3.1: McCain’s Generalizations for Fluid Types.....	32
Table 4.1: Basic reservoir rock and fluid properties for the simulation run.	41
Table 4.2: Summary of grid geometry for the single layer radial model.....	42
Table 4.3: Fluid composition of Fluid A, Fluid B and Fluid C.	45
Table 4.4: Basic fluid properties of Fluid A, Fluid B and Fluid C.	46
Table 5.1: Interpreted results when the probe pressure is much higher than the dew point pressure.	52
Table 5.2: Summary of interpreted results when the probe pressure is below the dew point pressure.	58
Table 5.3: Case definition and pressure drop of each case.	65
Table 5.4: Interpreted results for different drawdown rates.	68
Table 5.5: Case definition and pressure drop for Fluid B.....	72
Table 5.6: Interpreted results for different drawdown rates using Fluid B.....	76
Table 5.7: Interpreted results for different drawdown rates using Fluid C.....	77
Table 5.8: Case definition for different test duration.....	79
Table 5.9: Block condensate saturation for different test duration.....	83
Table 5.10: Interpreted results for different test duration.	83
Table 5.11: Case definition for different probe size.	85
Table 5.12: Interpreted results for different probe size.....	85
Table 5.13: Interpreted results for different probe position.....	88
Table 5.14: Case definition for different permeability anisotropy.	91
Table 5.15: Interpreted results for different permeability anisotropy.....	91
Table 5.16: Case definition for different horizontal permeability.	94
Table 5.17: Interpreted results for different horizontal permeability.	95
Table 5.18: Interpreted results for different reservoir pressure.	100
Table A1: Time step used in the simulation.	112

Table A2: Grid size for large probe.	115
Table A3: Grid size for extra-large probe.	116
Table A 4: Grid size to set standard probe at 3 ft below the middle of the formation.	117



ศูนย์วิทยทรัพยากร
จุฬาลงกรณ์มหาวิทยาลัย

List of Figures

	Page
Figure 3.1: Inverse problem.....	11
Figure 3.2: Drawdown and build-up test sequence.....	12
Figure 3.3: Example of derivative plot.	14
Figure 3.4: Typical WFT pressure record.....	15
Figure 3.5: Repeated drawdown and buildup pretests.....	16
Figure 3.6: Theoretical diagnostic plot.	17
Figure 3.7: Spherical flow regime.	20
Figure 3.8: Pressure derivative of spherical flow.	21
Figure 3.9: Radial flow regime.	22
Figure 3.10: Pressure derivative of radial flow or cylindrical flow.....	22
Figure 3.11: Hemispherical flow regime.	23
Figure 3.12: Pressure derivative of hemispherical flow.	24
Figure 3.13: History of formation tester.	25
Figure 3.14: MDT basic tool modules.....	27
Figure 3.15: MDT tool with optional modules.	29
Figure 3.16: Sketch of OFA module with LFA.	31
Figure 3.17: Sketch of OFA with CFA.....	31
Figure 3.18: Typical gas condensate phase diagram.	34
Figure 3.19: Constant composition phase diagram of a gas-condensate system.	34
Figure 3.20: Phase diagram of a near critical point condensate system.....	35
Figure 3.21: Phase diagram of a near critical point volatile oil system.....	36
Figure 3.23: Regions around gas condensate wellbore.....	37
Figure 3.24: Condensate saturation profile with condensate drop-out and velocity stripping.	38
Figure 3.25: Pressure and derivative composite behaviors: (a) three-region composite; (b) two-region composite.....	39
Figure 4.1: Gas-oil relative permeability curve used in the simulations.	41
Figure 4.2: Side view of a single layer radial model.	43

Figure 4.3: Top view of a single layer radial model.....	43
Figure 4.4: 3D view of a single layer radial model.....	44
Figure 4.5: Liquid drop-out for Fluid A, B and C.	46
Figure 4.6: Phase behavior of Fluid A.	46
Figure 4.7: Phase behavior of Fluid B.	47
Figure 4.8: Phase behavior of Fluid C.	47
Figure 5.1: A schematic of reservoir to study behavior below dew point pressure.....	49
Figure 5.2: Pressure and flow rate profile of lean Fluid A when the flowing probe pressure is much higher than the dew point pressure.	49
Figure 5.3: Derivative plot of lean Fluid A when the probe pressure is much higher than the dew point pressure.....	50
Figure 5.4: Condensate saturation and pressure profile at the end of drawdown of lean Fluid A when the probe pressure is much higher than the dew point pressure.	51
Figure 5.5: Composition of C_1 at probe cell versus time during drawdown period of lean Fluid A when the probe pressure is much higher than the dew point pressure.....	51
Figure 5.6: Composition profile of C_1 at the end of drawdown of lean Fluid A when the probe pressure is much higher than the dew point pressure.	51
Figure 5.7: A schematic of reservoir to study behavior below the dew point pressure.	53
Figure 5.8: Pressure and flow rate profile of lean Fluid A when the flowing probe pressure is below the dew point pressure.....	53
Figure 5.9: Derivative plot of lean Fluid A when the probe pressure is below the dew point pressure.	54
Figure 5.10: Condensate saturation and pressure profile at the end of drawdown of lean Fluid A when the probe pressure is below the dew point pressure.....	55
Figure 5.11: Relative permeability profile at the end of drawdown of lean Fluid A when the probe pressure is below the dew point pressure.	56
Figure 5.12: Phase behavior of the block near the probe cell at the end of drawdown of lean Fluid A when the probe pressure is below the dew point pressure.....	56
Figure 5.13: Composition profile of C_1 and C_5 at the end of drawdown of lean Fluid A when the probe pressure is below the dew point pressure.	57

Figure 5.14: Condensate saturation profiles during drawdown period of lean Fluid A when the probe pressure is below the dew point pressure.	58
Figure 5.15: Compositions profile during drawdown period of lean Fluid A when the probe pressure is below the dew point pressure.....	59
Figure 5.16: Composition at the probe cell versus time during drawdown period of lean Fluid A when the probe pressure is below the dew point pressure.....	61
Figure 5.17: Phase behavior at the probe grid block before 46 sec (T31) of production of lean Fluid A when the probe pressure is below the dew point pressure.....	61
Figure 5.18: Phase behavior at the probe grid block after 46 sec (T31) of production of lean Fluid A when the probe pressure is below the dew point pressure.....	62
Figure 5.19: Phase behavior at the probe cell during build-up period of lean Fluid A.	63
Figure 5.20: Composition at the probe cell during build-up period of lean Fluid A. ..	63
Figure 5.21: Composition profile at the beginning of build-up period of lean Fluid A.	64
Figure 5.22: Block condensate saturation during build-up period of lean Fluid A.	64
Figure 5.23: A schematic of reservoir for different drawdown rates.....	65
Figure 5.24: Condensate saturation profile at the end of drawdown of lean Fluid A for different drawdown rates.	66
Figure 5.25: Derivative plot of lean Fluid A for case A-r1.	66
Figure 5.26: Derivative plots of lean Fluid A for case A-r2, A-r3, A-r4 and A-r5.	67
Figure 5.27: Derivative plots of lean Fluid A for case A-r6, A-r7 and A-r8.....	67
Figure 5.28: Phase behavior at the end of drawdown for different drawdown rates for Fluid A.	68
Figure 5.29: A schematic of reservoir for different initial fluid compositions.....	71
Figure 5.30: Derivative plots for case B-r1, B-r2, B-r3 and B-r4.....	72
Figure 5.31: Derivative plots for case B-r5, B-r6 and B-r7,.....	73
Figure 5.32: Derivative plots for case C-r1, C-r2 and B-r3.....	73
Figure 5.33: Derivative plots for case C-r4, C-r5, C-r6 and C-r7.....	74
Figure 5.34: Condensate saturation profile at the end of drawdown for different drawdown rates for Fluid B.	74

Figure 5.35: Condensate saturation profile at the end of drawdown for different drawdown rates for Fluid C.	75
Figure 5.36: Phase behavior at the end of drawdown using Fluid B.	75
Figure 5.37: Phase behavior at the end of drawdown using Fluid C.	76
Figure 5.38: Schematic of a single layer reservoir with different test durations.	79
Figure 5.39: Derivative plot for different test durations.	80
Figure 5.40: Derivative plot for different build-up duration.	80
Figure 5.41: Derivative plot for different drawdown duration.	81
Figure 5.42: Schematic of a single layer reservoir with different probe sizes.	84
Figure 5.43: Derivative plot for different probe sizes.	85
Figure 5.44: Condensate saturation profile at the end of drawdown for different probe sizes.	86
Figure 5.45: Schematic of a single layer reservoir with different probe positions.	87
Figure 5.46: Derivative plot for different probe positions.	88
Figure 5.47: Condensate saturation profile at the end of drawdown for different probe positions.	89
Figure 5.48: Schematic of a single layer reservoir for different permeability anisotropies.	91
Figure 5.49: Derivative plot for different permeability anisotropies.	92
Figure 5.50: Condensate saturation for different permeability anisotropies.	92
Figure 5.51: Schematic of a single layer reservoir for different horizontal permeabilities.	94
Figure 5.52: Derivative plots for different horizontal permeabilities.	95
Figure 5.53: Condensate saturation for different horizontal permeabilities.	96
Figure 5.54: Schematic of a single layer reservoir with different reservoir pressures.	97
Figure 5.55: Derivative plot for different reservoir pressures.	98
Figure 5.56: Initial condensate saturation for different reservoir pressures.	99
Figure 5.57: Condensate saturation profile at the end of drawdown for different reservoir pressures.	99
Figure C1: Compositions profile during drawdown of Fluid A with 1 Mscf/d.	146
Figure C2: Compositions profile during build-up of Fluid A with 1 Mscf/d.	149

Figure D1: Derivative plot with an analytical model for case A-r1.	152
Figure D2: Derivative plot with an analytical model for case A-r2.	152
Figure D3: Derivative plot with an analytical model for case A-r3.	152
Figure D4: Derivative plot with an analytical model for case A-r4.	152
Figure D5: Derivative plot with an analytical model for case A-r5.	153
Figure D6: Derivative plot with an analytical model for case A-r6.	153
Figure D7: Derivative plot with an analytical model for case A-r7.	153
Figure D8: Derivative plot with an analytical model for case A-r8.	153
Figure D9: Derivative plot with an analytical model for case B-r1.....	153
Figure D10: Derivative plot with an analytical model for case B-r2.....	153
Figure D11: Derivative plot with an analytical model for case B-r3.....	154
Figure D12: Derivative plot with an analytical model for case B-r4.....	154
Figure D13: Derivative plot with an analytical model for case B-r5.....	154
Figure D14: Derivative plot with an analytical model for case B-r6.....	154
Figure D15: Derivative plot with an analytical model for case B-r7.....	154
Figure D16: Derivative plot with an analytical model for case C-r1.....	154
Figure D17: Derivative plot with an analytical model for case C-r2.....	155
Figure D18: Derivative plot with an analytical model for case C-r3.....	155
Figure D19: Derivative plot with an analytical model for case C-r4.....	155
Figure D20: Derivative plot with an analytical model for case C-r5.....	155
Figure D21: Derivative plot with an analytical model for case C-r6.....	155
Figure D22: Derivative plot with an analytical model for case C-r7.....	155
Figure D23: Derivative plot with an analytical model for case A-t1.....	156
Figure D24: Derivative plot with an analytical model for case A-t2.....	156
Figure D25: Derivative plot with an analytical model for case A-t3.....	156
Figure D26: Derivative plot with an analytical model for case A-t4.....	156
Figure D27: Derivative plot with an analytical model for case A-t5.....	156
Figure D28: Derivative plot with an analytical model for case A-STD.	156
Figure D29: Derivative plot with an analytical model for case A-L.	157
Figure D30: Derivative plot with an analytical model for case A-XL.	157

Figure D31: Derivative plot with an analytical model when the probe is set at 4 ft above the middle of the formation.....	157
Figure D32: Derivative plot with an analytical model when the probe is set at 3 ft above the middle of the formation.....	157
Figure D33: Derivative plot with an analytical model when the probe is set at 2 ft above the middle of the formation.....	158
Figure D34: Derivative plot with an analytical model when the probe is set at 1 ft above the middle of the formation.....	158
Figure D35: Derivative plot with an analytical model when the probe is set at 0.5 ft above the middle of the formation.....	158
Figure D36: Derivative plot with an analytical model when the probe is set at 0.5 ft below the middle of the formation.....	158
Figure D37: Derivative plot with an analytical model when the probe is set at 1 ft below the middle of the formation.....	159
Figure D38: Derivative plot with an analytical model when the probe is set at 2 ft below the middle of the formation.....	159
Figure D39: Derivative plot with an analytical model when the probe is set at 3 ft below the middle of the formation.....	159
Figure D40: Derivative plot with an analytical model when the probe is set at 4 ft below the middle of the formation.....	159
Figure D41: Derivative plot with an analytical model for case A-0.5kz.....	160
Figure D42: Derivative plot with an analytical model for case A-1kz.....	160
Figure D43: Derivative plot with an analytical model for case A-2.5kz.....	160
Figure D44: Derivative plot with an analytical model for case A-4kz.....	160
Figure D45: Derivative plot with an analytical model for case A-5kz.....	160
Figure D46: Derivative plot with an analytical model for case A-1k.....	160
Figure D47: Derivative plot with an analytical model for case A-3k.....	161
Figure D48: Derivative plot with an analytical model for case A-5k.....	161
Figure D49: Derivative plot with an analytical model for case A-8k.....	161
Figure D50: Derivative plot with an analytical model for case A-10k.....	161
Figure D51: Derivative plot with an analytical model for case A-50k.....	161
Figure D52: Derivative plot with an analytical model for case A-100k.....	161

Figure D53: Derivative plot with an analytical model for case A-3474.....	162
Figure D54: Derivative plot with an analytical model for case A-3468.....	162
Figure D55: Derivative plot with an analytical model for case A-3460.....	162
Figure D56: Derivative plot with an analytical model for case A-3400.....	162
Figure D57: Derivative plot with an analytical model for case A-3000.....	162
Figure D58: Derivative plot with an analytical model for case A-2600.....	162
Figure D59: Derivative plot with an analytical model for case A-2200.....	163



ศูนย์วิทยทรัพยากร
จุฬาลงกรณ์มหาวิทยาลัย

List of Abbreviations

API	degree (American Petroleum Institute)
bbbl	barrel (bbl/d : barrel per day)
C ₁	methane
C ₂	ethane
C ₃	propane
i-C ₄ or I-C ₄	isobutane
i-C ₅ or I-C ₅	isopentane
n-C ₄ or N-C ₄	normal butane
n-C ₅ or N-C ₅	normal pentane
C ₆	hexane
C ₇₊	alkane hydrocarbon account from heptanes forward
CO ₂	carbon dioxide
CFA	composition fluid analyzer
D	darcy
DFA	downhole fluid analyzers
DST	drillstem test
FIT	formation interval tester
FMT	formation multi-tester
FT	formation tester
IFT	low interfacial tensions
LFA	live fluid analyzers
M	thousand
MDT	modular dynamic formation tester
MST	multiset formation sampler
N ₂	nitrogen
OFA	optical fluid analyzer
PTA	pressure transient analysis
RCI	reservoir characterization instrument
RDT	reservoir description tool
RFS	repeat formation sampler

RFT	repeat formation tester
scf	standard cubic foot
SFT	selective formation tester
SFTT	sequential formation tester
WFT	wireline formation test



ศูนย์วิทยทรัพยากร
จุฬาลงกรณ์มหาวิทยาลัย

Nomenclature

A	cross-section area
B	formation volume factor
c	compressibility
c_t	total compressibility
h	formation thickness
k	formation permeability
k_r	relative permeability
k_{rg}	gas relative permeability
k_{ro}	oil relative permeability
k_{xy}	horizontal permeability
k_{xyz}	spherical permeability
k_z	vertical permeability
k_z/k_{xy}	vertical to horizontal permeability ratio
p	pressure
p_{dew}	dew point pressure
p_i	initial reservoir pressure
q_{sc}	production rate
R_i	block number i in radial direction
r_{dew}	radial distance where pressure equal to dew point pressure
r_{inv}	radius of investigation
r_w	wellbore radius
s	skin factor
S_o	condensate saturation
$S_{o,c}$	critical condensate saturation
t	time
T_i	time step number i
T	temperature
V	total volume of fluid produced

GREEK LETTERS

ρ	density
Φ	porosity
μ	fluid viscosity
Δ	difference operator



ศูนย์วิทยทรัพยากร
จุฬาลงกรณ์มหาวิทยาลัย

CHAPTER I

INTRODUCTION

Gas condensate reservoirs exhibit a complex flow behavior when wells are produced below the dew point pressure due to the existence of a two-fluid system, reservoir gas and liquid condensate. The formation of this liquid condensate can lead to a severe loss of well productivity and therefore, lower gas recovery. Different mobility zones develop around the wellbore corresponding respectively to the decline in reservoir pressure.

Wireline formation testing (WFT) is an alternative technique to obtain cost effective information from the reservoir such as formation pressure, fluid gradient, formation fluid samples, fluid contact, and an estimation of near wellbore permeability without disturbing reservoir pressure. It has been deployed to collect formation fluid samples and to measure formation pressure at discrete depths along a wellbore. WFT data typically yield estimates of fluid mobility and initial reservoir pressure. Pressure transient analysis of WFT data yields much more additional information, including estimates of spherical permeability, vertical to horizontal permeability ratio, formation skin factor, and the radius of investigation of the WFT test. However, it has not been reported that the pressure derivative in WFT is used to detect condensate drop-out around wellbore. This is due to the fact that there is not enough understanding on PTA in WFT especially in gas condensate reservoir.

The objective of this thesis is to study the effect of condensate bank on pressure transient data and the applicability of wireline formation test in gas condensate reservoir whether it can detect the increasing size of condensate bank. A reservoir simulator is used to determine pressure responses from wireline formation tests for single layer homogeneous gas-condensate reservoir. Pressure Transient Analysis (PTA) is used to estimate the reservoir parameters such as permeability and skin factor. Then, we compare the interpretation with the actual value used in the simulation.

1.1 Outline of Methodology

1. Gather and prepare data for simulation model.
2. Use reservoir simulator to simulate pressure responses from single probe wireline formation test in a single layer reservoir using lean gas condensate when the flowing pressure is above the dew point pressure to confirm numerical solution with the analytical solution.
3. Investigate phase behavior changes and interpret pressure responses obtained from step 2 to estimate reservoir parameters using well test interpretation software.
4. Simulate pressure responses from single probe wireline formation test in a single layer reservoir using lean gas condensate when the flowing pressure is below the dew point pressure to observed pressure behavior.
5. Investigate phase behavior changes and interpret pressure responses obtained from step 4 to estimate reservoir parameters using well test interpretation software.
6. Simulate pressure responses from single probe wireline formation test in a single layer reservoir using lean gas condensates with different drawdown rates.
7. Interpret pressure responses obtained from step 6 to estimate reservoir parameters using well test interpretation software.
8. Simulate pressure responses from single probe wireline formation test in a single layer reservoir using two rich gas condensates.
9. Interpret pressure responses obtained from step 8 to estimate reservoir parameters using well test interpretation software.
10. Simulate pressure responses from single probe wireline formation test in a single layer reservoir using lean gas condensate with different probe sizes, probe positions, test durations, initial reservoir pressures, permeability anisotropies and horizontal permeabilities.
11. Interpret pressure responses obtained from step 8 to estimate reservoir parameters using well test interpretation software.
12. Compare results obtained from simulated model with input value to justify whether the results from wireline formation test model provide satisfying information.

1.2 Thesis Outline

This thesis paper consists of six chapters and the outlines of each chapter are listed below.

Chapter II reviews previous works related to well test in gas condensate reservoir and wireline formation test (WFT).

Chapter III introduces the theory and concept related to this study.

Chapter IV shows simulation grid model used in the simulation.

Chapter V presents the study results from simulations and interpretations.

Chapter VI provides conclusions of the study and recommendations for the further study.



ศูนย์วิทยทรัพยากร
จุฬาลงกรณ์มหาวิทยาลัย

CHAPTER II

LITERATURE REVIEW

This chapter reviews previous works that are related to well test in gas condensate reservoirs and wireline formation test (WFT) studies.

2.1 Well Test in Gas Condensate Reservoirs

Gas condensate is often found as single-phase gas in the reservoir. As the fluid is produced, the pressure decreases from the reservoir to the wells, leading to condensation of liquid out of the gas. Due to lower permeability to liquid, a high liquid-to-gas viscosity ratio and lower condensate saturation than the critical value, most of the condensed liquid in the reservoir is unrecoverable and constitutes the “condensate loss”.

Muskat^[1] observed the condensate blockage problem in gas cycling operation. He discussed that condensate builds up in the vicinity of the wellbore and starts to flow when its saturation reaches a critical value. After that, many studies showed the loss of well deliverability due to gas condensate blockage^[2-5].

Knaizeff and Naville^[6] suggested that three radial zones appear with different liquid saturations when the liquid condensate saturation reaches a critical value. Away from the well, an outer region, where the pressure is still above the dew point pressure, contains gas with the initial liquid saturation; next, there is an intermediate region with a rapid increase in liquid saturation and a corresponding decrease in gas relative permeability. Liquid in that region is immobile. Closer to the well, a region forms where the liquid saturation reaches a critical value, and the fluid travels as a two-phase fluid. A large number of studies confirm that when the bottomhole pressure drops below the dew-point pressure, the reservoir and near wellbore region can be divided into three radial zones with different liquid saturations discussed above^[4, 7-9].

As the reservoir pressure declines, the composition of the system changes due to the lack of mobility of the condensate liquid phase. The lighter components such as methane, ethane and propane decreases, while the heavy components increases^[1].

Novosad^[10] discussed that the changes in fluid composition is a result of changes in fluid transported from the reservoir interior, a broad spectrum of fluid types exist at different points in time and space.

Roussennac^[11] illustrated the compositional change during the depletion in his numerical simulation. He observed that during the drawdown period, the overall mixture close to the well becomes richer in heavy components as the liquid builds up in the well grid cell, and the fluid behavior changes from the initial gas condensate to a volatile oil behavior.

Wheaton and Zhang^[12] simulated simple methane-pentane binary systems and attempted to show how the compositions of heavy components of a gas condensate change with time around production wells during depletion. They concluded that an increase in the total molar concentration of heavy components around the well will occur once the flowing bottomhole pressure falls below the dew point. The rate of the change in heavy component composition is higher for rich gas than for lean gas condensate for the same reservoir system.

Bengherbia and Tiab^[13] also demonstrated in their study that both the production history and the simulation prediction show an increase in lighter components in the flowing phase once the pressure drops below the dew point, but it is still not clear how the compositions vary with time and space and how the composition change affects the gas production and the condensate recovery.

Economides et al.^[14] stated that there may also exist a fourth region in the immediate vicinity of the well where low interfacial tensions (IFT) at high rates yield a decrease of the liquid saturation and an increase of the gas relative permeability.

Danesh et al.^[15] were first to report the improvement of relative permeability of condensing systems due to an increase in velocity as well as that caused by a reduction in interfacial tension as velocity increases, known as the coupling effect.

Gringarten et al.^[16] found the first well test evidence in the literature of the existence of the velocity stripping zone. The authors concluded that when capillary number effects are important, the pressure derivative should exhibit three stabilization periods.

Daungkaew and Gringaten^[17] concluded that this zone could not be identified in all well test data due to several reasons: (1) maximum condensate saturation near

the wellbore was not significantly enough; (2) wellbore storage effects at early times hid the increased gas mobility zone; (3) the duration of the test was not long enough; (4) the quality of pressure data was not good enough; and (5) phase redistribution effects occurred in the wellbore.

Gringarten et al.^[18] compared theoretical well test behaviors in vertical and horizontal wells as obtained from compositional simulation with actual behaviors selected from more than twenty different gas condensate reservoirs using time-lapse analyses, deconvolution and different analytical and numerical tools to identify the probable causes of the pressure data behavior. It was shown that, in addition to the usual well test analysis results, it is possible to obtain parameters required for reservoir simulation and well productivity forecasting, such as gas relative permeabilities at the end point, critical condensate saturation, and the base capillary number.

Aluko and Gringarten^[19] investigated well test behavior of rich gas condensate reservoirs below the dew point. The authors suggested that near-wellbore fluid saturation below the dew point pressure in a build up is different from that at the end of the preceding drawdown because of significant differences in fluid properties and saturation distributions. The corresponding pressure derivatives are different.

2.2 Wireline Formation Test (WFT)

Wireline Formation Test (WFT) is used to obtain formation pressure along the borehole to examine fluid gradient, formation fluid sampling and estimate reservoir permeability which is a key parameter during exploration and development field. Several analytical solutions, interpretation techniques of WFT and the application of WFT for some situations have been presented in the literatures.

Doll^[20] first considered the estimation of permeability and permeability anisotropy from pressure transient analysis in formation test. After that, Moran and Flinklea^[21] presented a theoretical analysis of pressure data from wireline formation test. They recognized the difference in flow geometry between formation testers and conventional drill-stem tests. This leads to a completely different equation for the analysis of the pressure response. Therefore, the interpretation needs to be modified.

Assuming single phase flow and permeable beds of finite thickness homogeneous medium, they showed that the early time fluid flow regimes enforced with a probe type formation tester are spherical in nature while the late time regimes are best described by cylindrical flow. Even though their work did not consider the effects of skin and tool storage, they did consider the effect of permeability anisotropy on the measurements. They also developed the general equation for spherical flow in addition to van Everdingen and Hurst's equation for linear flow and Horner's equation^[22] for radial flow. There was also a discussion on the depth of investigation which was shown to be large comparing to the size of spherical sink and also a case involving permeability anisotropy.

Culham^[23] extended the work of Moran and Flinklea^[21] by showing that the assumption of spherical flow is not only valid for a single perforation but also valid for the conventional wellbore geometry or any limited entry perforation. This equation is valid for both conventional well test and wireline formation test. In addition, equations for calculating formation permeability and skin factors were presented. The author also derived the radius of investigation equation for spherical flow problem.

Stewart and Wittmann^[24] estimated permeability from the Repeat Formation Tester (RFT) pretest pressure response. They extended the work of Moran and Finklea^[21] which studied on the Formation Interval Tester (FIT). The authors derived analytical solutions for spherical flow in both an infinite medium system and the case of a reservoir layer bounded above and below by impermeable barriers and also studied the effect of formation anisotropy and the depth of investigation. In addition, they also discussed the upper limit of measurable permeability from buildup by presenting the relationship between the maximum detectable permeability and gauge resolution for different fluid properties.

Dussan and Sharma^[25] illustrated an analysis solution to estimate the horizontal and vertical permeability near the probe by using pressure response obtained from single probe formation tester during drawdown and buildup test. The authors applied Darcy's equation to be an analysis solution with the assumption that the formation is homogeneous and anisotropic. As a result, it has been shown that the

accuracy of the prediction of the horizontal permeability is better than that of vertical permeability.

Goode and Thambynayagam^[26] discussed the advantages of a formation tester with three probes over single probe tester. Three probes formation tester consists of one sink probe and two observation probes. The sink probe generates a pressure pulse by withdrawing fluid from the formation while the resulting pressure response is measured at the sink probe and at each of two observation probes. The authors presented an analytical equation to model the tool response in both vertically bounded and unbounded reservoirs to interpret pressure transients measured by a multiprobe formation tester. It was demonstrated that a multiprobe formation tester can provide data to determine the horizontal and vertical permeabilities and the formation storativity.

Kuchuk et al.^[27] described basic features of the packer module and the observation probe tool combination of the multi-probe wireline formation tester. They presented an analytical solution for the formation behavior with the packer and probe geometry using a modified dimensionless function and provided estimation of the formation parameters.

Proett et al.^[28] introduced a technique to estimate compressibility of the fluid in the flow line, pressure, and permeability in tight reservoir. Since wireline formation tester draws fluid in a short period of time and small volume, the data may be distorted by flow line storage effect when the test is conducted in a tight zone. They introduced a special plot to interpret real time data obtained during initial drawdown and buildup.

Frimann-Dahl et al.^[29] applied advanced well test analysis technique to wireline formation test data. However, the case they presented used a large probe area, and the pressure transient response observed was therefore similar to typical response encountered during conventional well testing. Advanced pressure transient analysis has been applied to wireline formation test data acquired with dual probe, multiprobe, and dual or "straddle packer" configurations.

Whittle et al.^[30] discussed key issues with examples using a single probe wireline formation test dataset. The authors revealed that a well test can be replaced by a wireline formation test if the objectives of the well test can be met by the

wireline formation test. In lower permeability reservoirs (mobilities less than about 100 mD/cp), the quality of data recorded by wireline formation test tools is suitable for pressure transient interpretation.

Daungkaew et al.^[31] illustrated the information that can be obtained from pressure transient analysis of wireline formation test data using an advanced well test analysis technique. The authors discovered that the detailed observation of pressure transient response can provide additional understanding of reservoir even though the radius of investigation of the WFT is very small, i.e., to monitor the pump-out data in gas reservoir, to indicate an increasing fluid mobility away from the probe, and to confirm oil water contact. In addition, the wireline formation tests can then be used to identify valid tests or quality control.



ศูนย์วิทยทรัพยากร
จุฬาลงกรณ์มหาวิทยาลัย

CHAPTER III

THEORY AND CONCEPT

This chapter presents the fundamental of well test interpretation, wireline formation test and gas condensate reservoirs.

3.1 Basic Well Test Interpretation

Well test is used to monitor the response of the well and reservoir to changing production or injection conditions. During a well test, a transient pressure response is created by a temporary change in production rate. The well response is usually monitored during a relatively short period of time compared to the life of the reservoir, depending upon the test objectives. For well evaluation, tests are frequently achieved in less than two days. In the case of reservoir limit testing, several months of pressure data may be needed. Well tests are conducted at all stages in the life of a reservoir: exploration, development, production and injection. At each of these stages, tests are performed with set objectives, using specific hardware and design options. Well test responses characterize the ability of the fluid to flow through the reservoir and to the well. Tests provide a description of the reservoir in dynamic conditions, as opposed to geological and log data. As the investigated reservoir volume is relatively large, the estimated parameters are average values^[32].

Well test analysis is an inverse problem as shown in Figure 3.1. The reservoir properties can be inferred by the response since the response is the characteristic of the reservoir properties. Well test analysis is sometime called pressure transient analysis (PTA) since the measured reservoir response is pressure. The pressure transient is due to changes in production or injection of fluids, hence we treat the flow rate transient as input and the pressure transient as output. The pressure response is analyzed to provide the model(s) whose behavior is identical to the behavior of the actual reservoir.

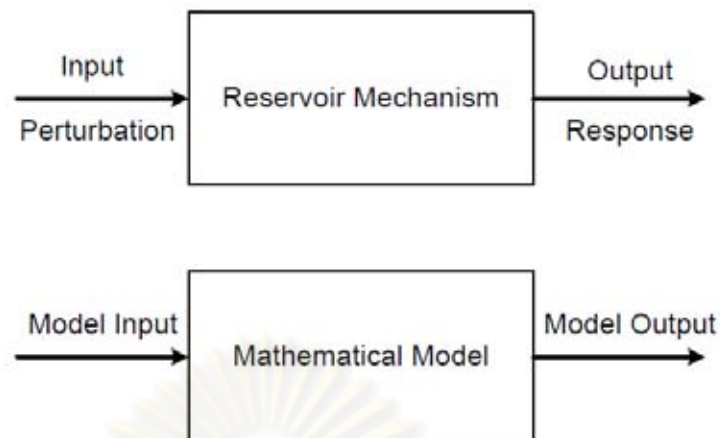


Figure 3.1: Inverse problem^[33].

There are several types of tests such as drawdown test, build up test, injection test, falloff test, interference test, and drill stem test (DST). The type of test depends on the test objectives or practical limitations.

Drawdown and build-up test sequence is used in most cases and also in this work as shown in Figure 3.2. The flow rate is usually measured at surface while the pressure is recorded down-hole. Before opening, the initial pressure p_i is constant and uniform in the reservoir. The drawdown pressure response Δp_{Dd} is recorded during flow time. When the well is shut-in, the build-up pressure change Δp_{BU} is estimated from the last flowing pressure $p(\Delta t=0)$. Then pressure response is analyzed versus the elapsed time Δt since the start of the period (time of opening or shut-in).

Analysis of drawdown test may be difficult to achieve in practice because it is difficult to control the flow rate to be constant. However, it is a good method to test reservoir limit since the time required to observe a boundary response is long and operating fluctuations in flow rate become less significant over such long times.

Build-up test may be easier to analyze since the buildup flow rate is constant as zero. However, it may be difficult to control flow rate before the shut-in and may lose production during shut-in.

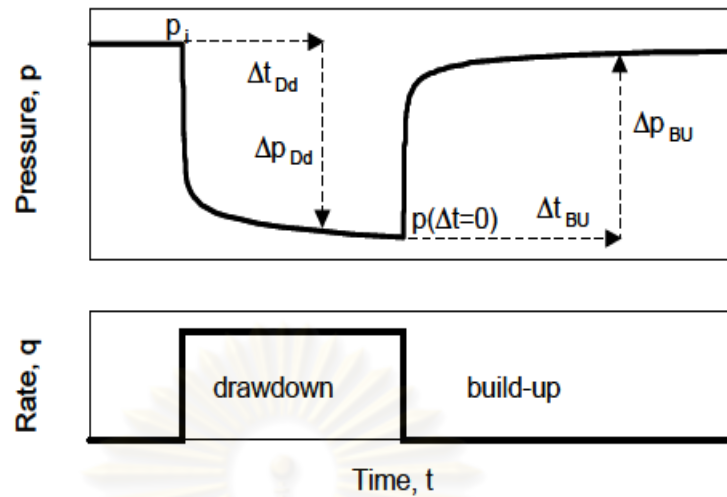


Figure 3.2: Drawdown and build-up test sequence^[32].

3.1.1 Transient Flow Equation

Fluid flow in porous media is governed by the diffusivity equation. The diffusivity equation can be derived by combining the law of conservation of mass, Darcy's law and an equation of state as expressed in Eq. 3.1. It is one of the most important equations in petroleum engineering. The equation is particularly used in analysis well testing data where the time t is commonly recorded in hours.

$$\nabla^2 p = \frac{\phi \mu c_t}{k} \frac{\partial p}{\partial t} \quad (3.1)$$

For radial flow,

$$\frac{\partial^2 p}{\partial r^2} + \frac{1}{r} \frac{\partial p}{\partial r} = \frac{\phi \mu c_t}{0.000264 k} \frac{\partial p}{\partial t} \quad (3.2)$$

where

k	=	permeability, mD
r	=	radial position, ft
p	=	pressure, psia
c_t	=	total compressibility, psi^{-1}

t	=	time, hrs
ϕ	=	porosity, fraction
μ	=	viscosity, cp

3.1.2 The Derivative Plot

In traditional well test analysis, different plots are used for different purposes, and most analysis will require the consideration of several plots. Modern analysis started since Bourdet et al.^[34] developed the pressure derivative analysis method to characterize the flow regimes in 1983. The derivative plot is a plot of $\log(\Delta p)$ versus $\log(\Delta t)$ and $\log(\Delta t \frac{\partial p}{\partial t})$ versus $\log(\Delta t)$. The advantage of the derivative plot is that it is able to display in a single graph many separate characteristics that would otherwise require different plots.

Figure 3.3 shows an example of derivative plot. Each plot consists of two curves presented as log-log graphs. The top curve represents the pressure changes associated with an abrupt production rate perturbation, and the bottom curve indicates the rate of pressure change with respect to time, derivative curve. Its sensitivity to transient features resulting from well and reservoir geometries makes the derivative curve the single most effective interpretation tool. However, it is always viewed together with the pressure change curve to quantify skin effects that are not recognized in the derivative response alone.

ศูนย์วิทยทรัพยากร
จุฬาลงกรณ์มหาวิทยาลัย

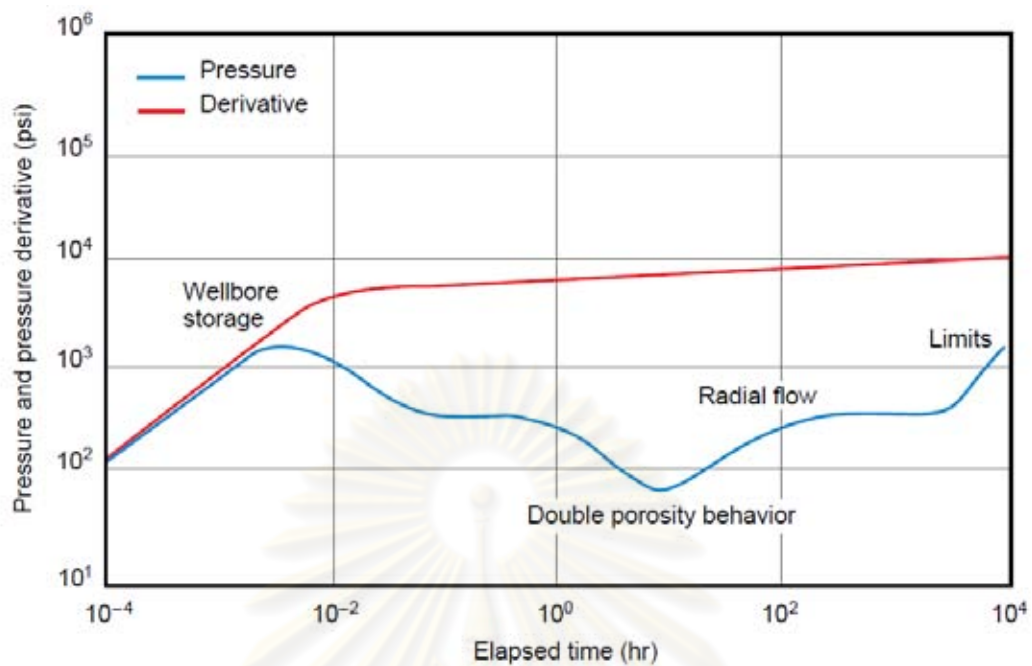


Figure 3.3: Example of derivative plot.

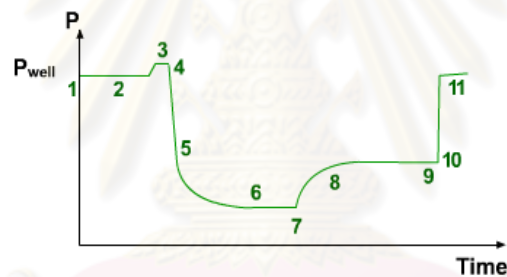
3.2 Wireline Formation Test

Wireline formation tests (WFT) are performed mostly in open hole using a cable-operated formation tester and sampling tool to obtain information from the reservoir. This measurement can provide formation pressures along the borehole and also fluid sampling. Pressure transient data are collected and can be analyzed using Pressure Transient Analysis (PTA) technique to estimate the reservoir parameters. These tools are normally run as part of the open hole logging suite. They are conveyed on large heptacables and consist of precision engineered electro-hydraulic tools capable of performing a variety of tasks. The WFT data typically yields estimation of fluid mobility and initial reservoir pressure. Pressure transient analysis of WFT data uses the same principal as advanced well test analysis and, in many cases, yields more additional information, including estimates of spherical permeability and vertical to horizontal permeability ratio.

3.2.1 Wireline Formation Test Procedure

When WFT tool reaches a target interval, the probe is set in the wellbore. The pretest is then performed by conducting a short drawdown followed by a build-up. The fluid is drawn until the pressure drops below the formation pressure, and then pump-out module was stopped to let the pressure build-up and stabilize at the formation pressure. The main objective of the pretest is to obtain the initial formation pressure.

Figure 3.4 shows a pressure versus time plot of a typical pretest. In a standard pretest, between 5 to 20 cm³, typically 10 cm³, of fluid are withdrawn from the formation through the probe into the pretest chamber. This creates a pressure disturbance and a localized flow around the probe.



- 1 Tool is stopped at desired pressure test depth.
- 2 All pressure gauges read hydrostatic mud pressure.
- 3 Tool is set, flowline pressure may rise due to packer compression.
- 4 Pretest is started.
- 5 Tool flowline expands during initial drawdown.
- 6 Steady state reached below formation pressure.
- 7 Pretest piston stops drawdown, buildup begins.
- 8 Buildup time varies with formation fluid mobility.
- 9 Pressure stabilizes at formation pressure.
- 10 Tool is retracted.
- 11 Pressure gauges return to hydrostatic mud pressure.

Figure 3.4: Typical WFT pressure record^[35].

In pretest period, the flow regime is commonly spherical or hemispherical because the pressure disturbance has a depth of investigation that is too small to reach impermeable boundaries in most cases. The drawdown pressure depends on the

mobility, k/μ , of the flowing fluid, which is usually mud filtrate from the invaded zone.

At the end of the drawdown period, the pretest chamber is full and the build-up period starts. The pressure disturbance continues to advance in a pattern similar to the drawdown period because of fluid flowing from the undisturbed part of the formation toward the low-pressure area near the probe. The pressure measured at the probe rises until it reaches the formation pressure. The time required for this buildup is essentially a function of the formation fluid mobility and the pretest drawdown volume.

During the buildup period, the pressure disturbance propagates spherically and continues in this manner until one impermeable barrier is reached. At this stage, the spherical flow pattern is altered and becomes hemispherical. Eventually, if a second vertical barrier is detected, the hemispherical propagation becomes radial.

To avoid the mud invasion effect in practice, the repeated tests may be performed to obtain the accurate formation pressure as shown in Figure 3.5. The first drawdown period is to clean up formation damage and adjust the choke. Then, drawdown and buildup are repeated again. The reservoir pressure is estimated from the last build up which has the same value of reservoir pressure as in the previous build up as shown in the figure.

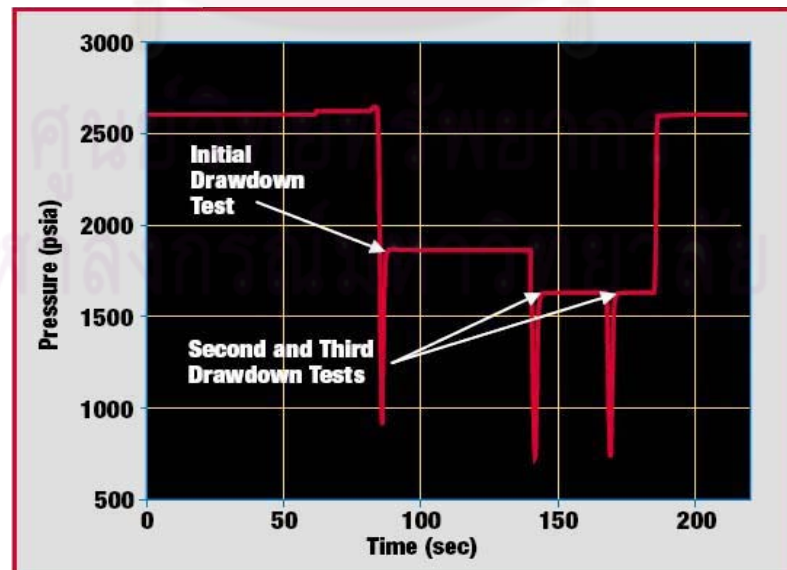


Figure 3.5: Repeated drawdown and buildup pretests.

To obtain a representative reservoir fluid, the pump-out module is then started again to clean up fluid with a longer drawdown. Once reservoir fluid is observed in the flowline, the pumps are stopped and pressure is recorded during the main build up. The pressure response obtained from the last build-up period can be used to estimate reservoir parameters, i.e. vertical and horizontal permeability, skin factor, wellbore storage and radius of investigation. The pressure derivative is a popular tool to identify different flow regimes and provide the estimate of reservoir parameters.

Figure 3.6 shows the theoretical constant-rate pressure-derivative plot. The dashed curve corresponds to the spherical time function and the solid curve to the radial time function. A time interval for which the derivative of the pressure with respect to the spherical time function has a flat trend should correspond to the time when the flow is spherical. During this interval, the derivative of the pressure with respect to the radial time function should have a slope of $-1/2$. Similarly, a time interval for which the derivative of the pressure with respect to the radial time function has a zero slope should correspond to the time when the flow is radial. During this interval, the derivative of the pressure with respect to the spherical time function should have a slope of $+1/2$.

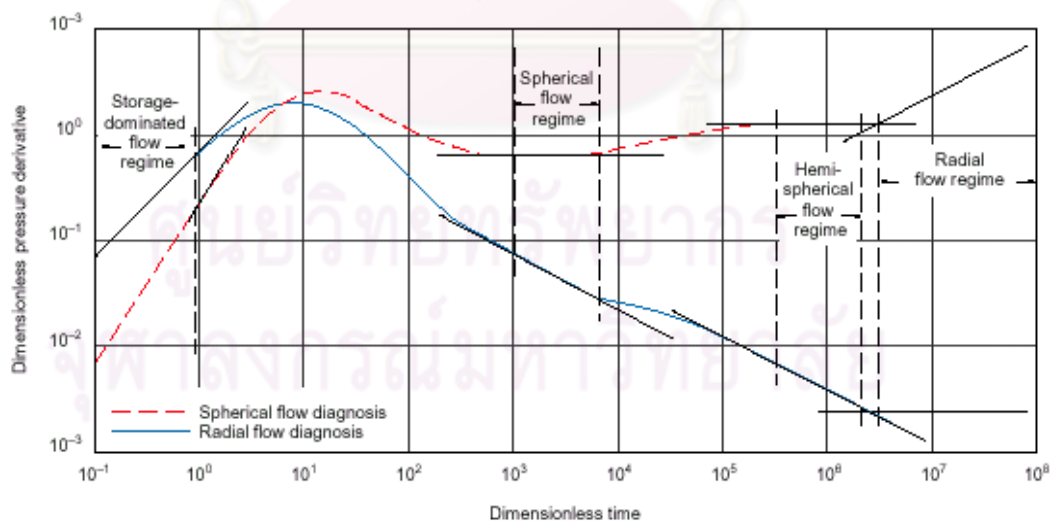


Figure 3.6: Theoretical diagnostic plot^[36].

3.2.2 Wireline Formation Test Interpretation

The same principal as advanced well test analysis technique is used in wireline formation test data to obtain reservoir information. There are three main possible flow regimes which are linear flow in the open interval, spherical flow when there is a vertical contribution to flow, and radial flow when the upper and lower boundaries have been seen.

Horner^[22] derived the radial flow equation for buildup period in 1951. Then, Moran and Finklea^[21] presented the spherical flow equation in 1962 and also showed that only the last two flow regimes, radial flow and spherical flow, can be seen in wireline formation test.

For radial flow equation^[22],

$$p(t) = p_i - \frac{\mu}{4\pi k} \frac{V}{t} [\ln(t + \Delta t) - \ln(\Delta t)] \quad (3.3)$$

where	$p(t)$	=	pressure at time t (dynes/cm ²)
	p_i	=	initial reservoir pressure (dynes/cm ²)
	μ	=	fluid viscosity (poises)
	k	=	formation permeability (mD)
	c	=	compressibility (cm ² /dyne)
	α	=	$\mu c \Phi / k$ (sec/cm ²)
	t	=	total time the tool is opened (sec)
	Δt	=	time after the tool is closed (sec) (buildup time)
	V	=	total volume of fluid produced (cm ³)

The spherical flow regime is controlled by the spherical permeability, k_{xyz} and equations^[31] for spherical flow is as follows:

$$\Delta p = \frac{qB\mu}{2a_1 k_{xyz} r_s} \left[1 - \sqrt{\frac{\Phi \mu c_t r_s^2}{\pi a_2 k_{xyz}}} \frac{1}{\sqrt{\Delta t}} + s_p \right] \quad (3.4)$$

The spherical permeability is

$$k_{xyz} = \sqrt[3]{k_x k_y k_z} = \sqrt[3]{k_{xy}^2 k_z} \quad (3.5)$$

And, the horizontal permeability is

$$k_{xy} = \sqrt[2]{k_x k_y} \quad (3.6)$$

where	μ	=	fluid viscosity (cp)
	Φ	=	porosity (fraction)
	k_{xyz}	=	spherical permeability (mD)
	k_{xz}	=	horizontal permeability (mD)
	k_z	=	vertical permeability (mD)
	c_t	=	total compressibility (psi ⁻¹)
	B	=	formation volume factor (RB/STB)
	Δt	=	time (hrs)
	p_i	=	initial reservoir pressure (psi)
	Δp	=	pressure drop (psi)
	q	=	flow rate (STB/Day)
	r_s	=	probe radius (ft)
	S_p	=	probe skin factor
	a_1	=	0.00708
	a_2	=	0.0002637

3.2.3 Wireline Formation Test Flow Regimes

During testing of wireline formation test, the flow regime is commonly spherical flow or hemispherical flow and radial flow near the probe which can be characterized by pressure derivative plot.

3.2.3.1 Spherical flow

At early times, pressure response is dominated by the tool storage effect. This effect will show a hump in the pressure derivative plot similar to wellbore storage effect.

At middle times, when the fluid in the formation is moving into the probe, which has a small diameter, the flow regime is spherical as shown in Figure 3.7 because the pressure disturbance has a depth of investigation that is too small to reach impermeable boundaries. This flow regime can be observed by a negative half slope straight line in the pressure derivative plot as shown in Figure 3.8. The spherical flow regime is controlled by spherical permeability, k_{xyz} and from this flow regime k_{xyz} can be estimated.

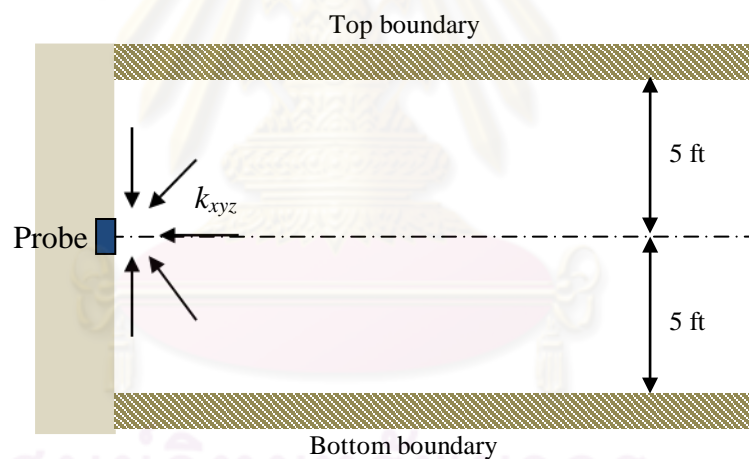


Figure 3.7: Spherical flow regime.

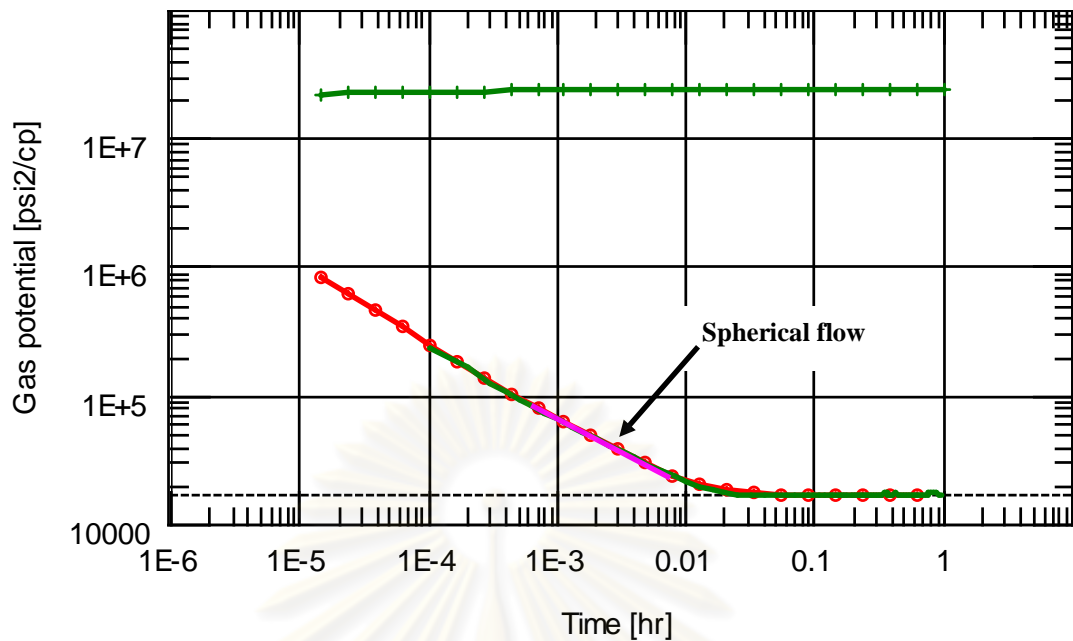


Figure 3.8: Pressure derivative of spherical flow.

3.2.3.2 Radial flow

When pressure disturbance encounters upper and lower boundaries as shown in Figure 3.9, the flow regime is now radial or cylindrical flow. Vertical to horizontal permeability ratio can be calculated if the upper and lower boundaries are known from other source of data such as well logging. In a pressure derivative plot as in Figure 3.10, spherical flow occurs at early times, and then radial flow develops as pressure response reaches the top and bottom boundaries and can be identified by stabilization line on the pressure derivative. The horizontal permeability (k_{xy}), vertical permeability (k_z), and vertical to horizontal permeability ratio (k_z/k_{xy}) can be obtained from this flow regime.

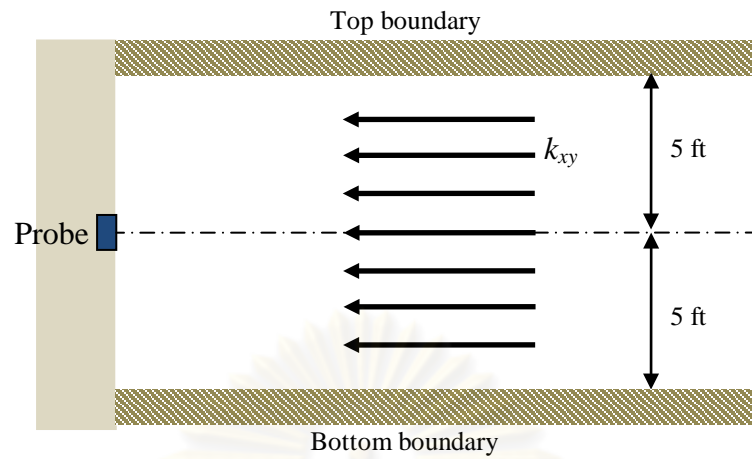


Figure 3.9: Radial flow regime.

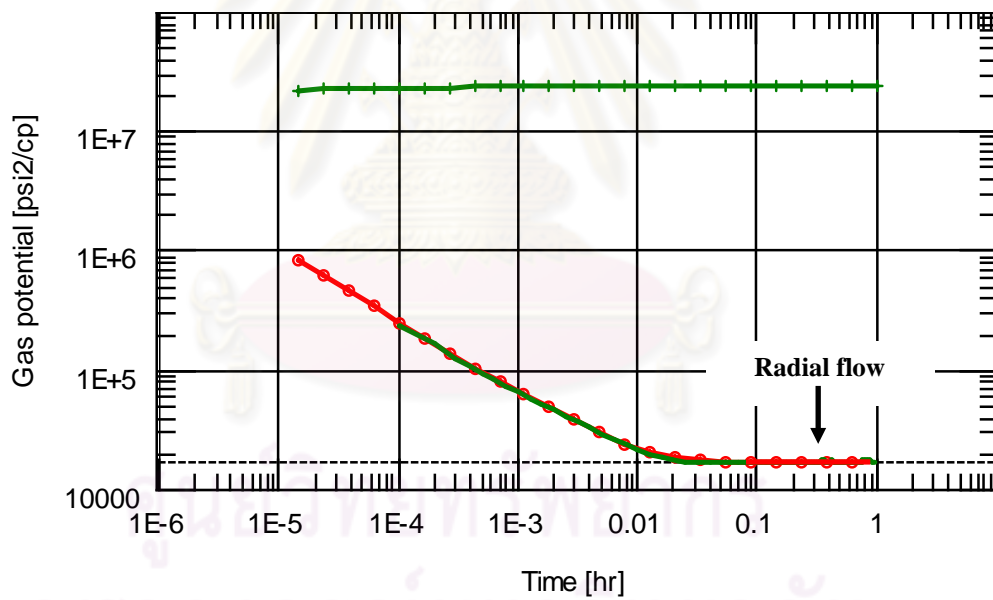


Figure 3.10: Pressure derivative of radial flow or cylindrical flow.

3.2.3.3 Hemispherical flow

When the probe is placed close to the top or bottom boundary, spherical flow will not fully developed. Part of the pressure response hits the closer boundary and starts to develop into radial flow while the other still acts like spherical flow as shown in Figure 3.11. In a pressure derivative log-log plot as shown in Figure 3.12, at early times, the pressure response is influenced by spherical flow. After that, pressure disturbance reaches the closer boundary; then, hemispherical flow takes place, identified by another negative half slope in the derivative plot. Then, when the pressure response reaches both the top and bottom boundaries, radial flow is fully developed.

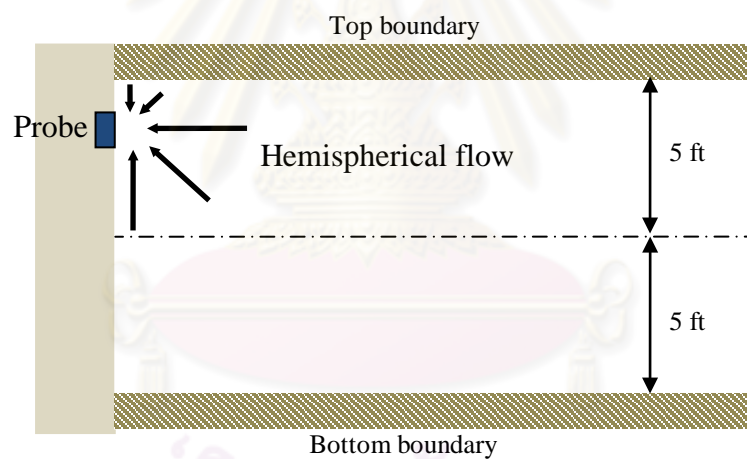


Figure 3.11: Hemispherical flow regime.

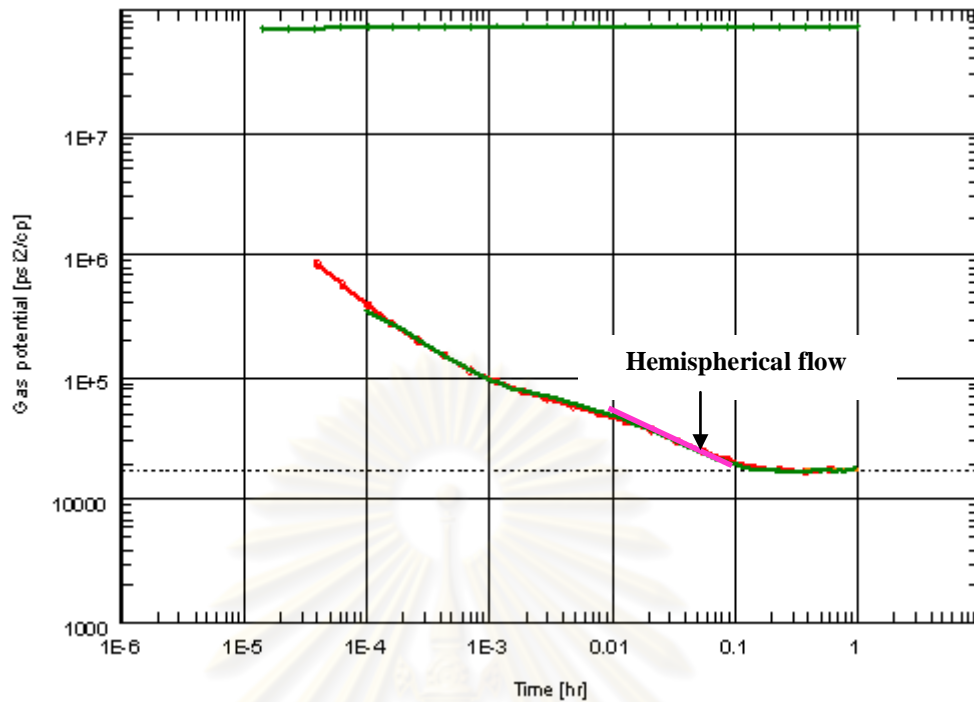


Figure 3.12: Pressure derivative of hemispherical flow.

3.2.4 Wireline Formation Test Tools

Wireline formation testers have developed through a series of innovations as shown in Figure 3.13. The first tools was commercially used in 1955 in the Gulf of Mexico, primarily to recover one fluid sample and measure one formation pressure on each trip to the well. Later, the Formation Interval Tester (FIT) was also introduced.

In 1975, the Repeat Formation Testers (RFT) replaced its predecessors FT or FIT, starting in the North Sea. It added the capability to repeatedly measure formation pressure during a single trip. This marked the beginning of a new era in wireline formation testing technology and application. Then, a variety of wireline testers were available on the market, satisfying the growing need of oil companies in their exploration and development projects. Traditional testers developed in the 1970s and 1980s were very successful in a variety of pressure surveys and applications in single well and reservoir evaluations.

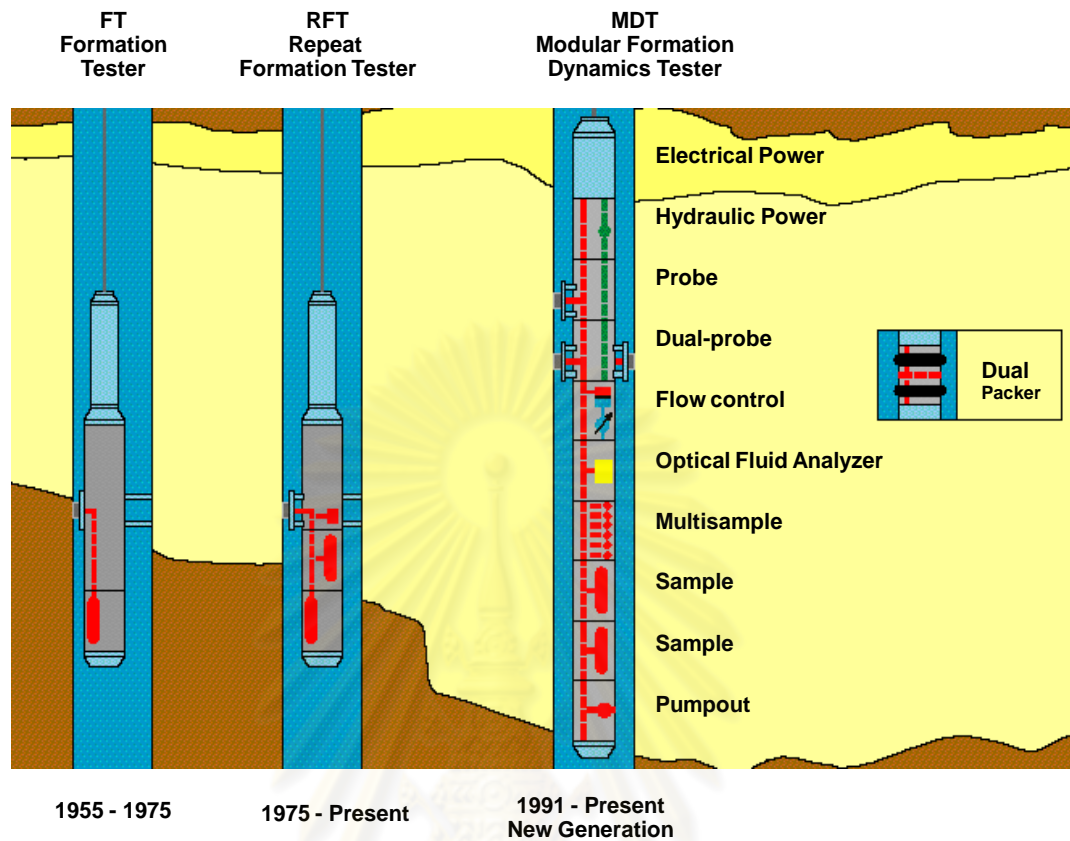


Figure 3.13: History of formation tester^[37].

In the early 1990s, wireline tester technology took another huge step forward. Schlumberger designed a new modular tool, Modular Dynamics Tester (MDT), to provide answers to complex and varied reservoir questions, particularly fluid typing and sampling, marking a new revolution in wireline formation testing with much enhanced features and capabilities. It can be used to determine formation permeability from pressure transients. Then, Baker-Atlas debuted its Reservoir Characterization Instrument (RCI), and in 1999 Halliburton brought Reservoir Description Tool (RDT) to the marketplace.

Now wireline formation testers can be separated into two groups, traditional testers and modern testers. Traditional testers currently still being used in the oil industry, Repeat Formation Tester (RFT), by Schlumberger, Formation Multi-Tester (FMT) by Baker Atlas, Selective Formation Tester (SFT) and Sequential Formation Tester (SFTT) by Halliburton, Repeat Formation Sampler (RFS) by Reeves Wireline and, Formation Tester (FT) by Tucker Wireline, represent the family of traditional

wireline testers. Traditional testers have a fixed-volume pretest chamber from 20-cc to 38-cc and cannot perform extended flows for pressure testing or sampling quality control. For modern wireline testers, several tools have been introduced. Schlumberger's MDT, Halliburton's RDT, and Baker Hughes' RCI lead the wireline testing services worldwide. All these three testers have multifunctional features for a broad span of reservoir evaluation applications, from pressures, fluid identification and sampling, to mini-drillstem testing and permeability evaluations. All these three testers are modular tools; each tool string has to be assembled by stacking all required modules before running into the well.

This study is emphasizing on MDT tool. Modern wireline formation tester can be arranged in a variety of configurations depending on testing needs. The MDT string can be configured for the desired testing objectives. The following section includes a brief description of the MDT tool modules.

3.2.4.1 Basic Tool Modules

The modern wireline testers system comprises a number of modules. The tool is designed to take several pressure measurements and fluid samples during one trip in the well. There are four modules making up the basic tool as shown in Figure 3.14. This configuration which extends the capabilities of existing single-probe testers provides a basic tool to which additional modules and therefore capabilities can be added. Normally the top section of each module houses the electronics, and the bottom section contains the hydraulics and valves. The tool is usually combined with a gamma ray device for depth control and an Auxiliary Measurement Sonde (AMS) tool for tension monitoring.

1) Electrical module - This module converts AC power from the surface to provide tool electrical DC power to drive all the downhole electronics and a supply for the electro-hydraulic system. The electric power module is used in every MDT configuration and always at the top of the tool string.

2) Hydraulic power module - This provides hydraulic power to the probe module by way of a hydraulic bus. It contains an electric motor and a hydraulic pump. Any module needing hydraulic power must be connected immediately next to the

hydraulic power module. This also means that modules that do not have a hydraulic bus cannot be connected between modules using the hydraulic bus. For example, a sample chamber cannot be placed between a hydraulic power module and a single-probe module.

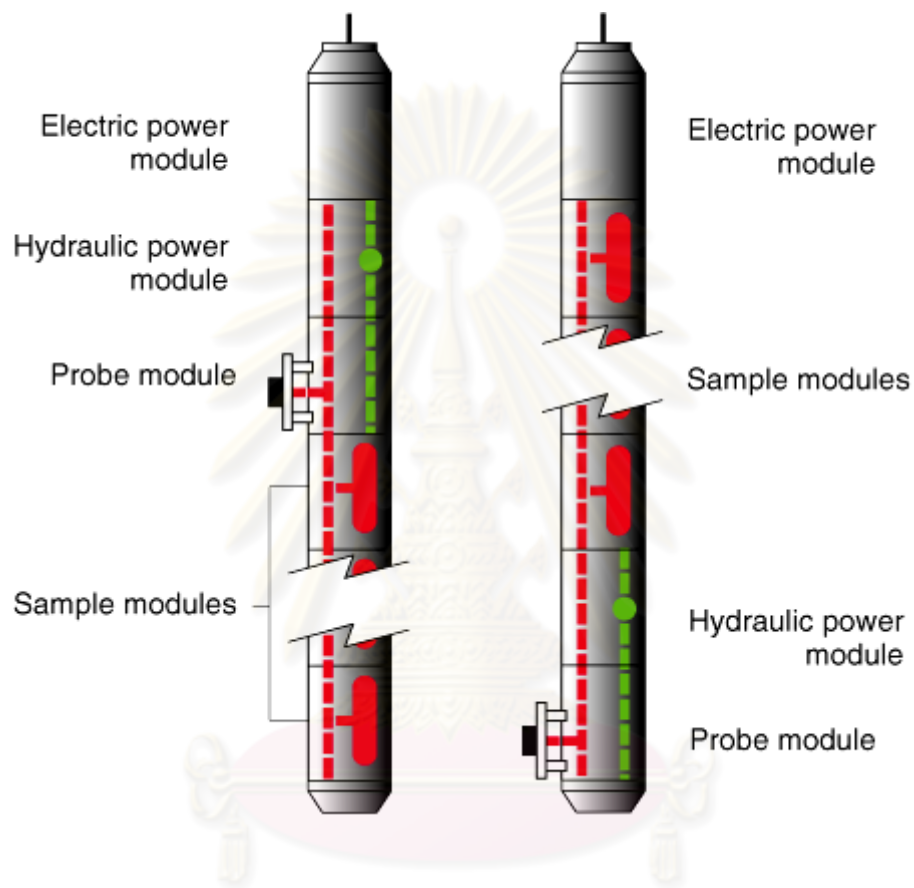


Figure 3.14: MDT basic tool modules^[35].

3) Single probe module - This module establishes pressure and fluid communication between the tool and the formation. Connected directly to the hydraulic power module, the single-probe module contains a probe assembly with packer and telescoping backup pistons and connects the tool flowline to the reservoir. It also houses the strain and quartz gauges and fluid resistivity and temperature sensors and provides pretest functions. The single-probe module can be placed anywhere in the string, but it must be directly connected to the hydraulic power module.

The probe extends against the borehole wall to provide a sealed fluid path from the reservoir to the flowline. The pretest is used to ensure a good hydraulic seal, obtain accurate formation pressure recordings and determine permeability. The module has one pretest chamber with a maximum volume of 20 cm³. The MAXIS 500* service unit controls the sampling pressure, pretest flow rate and volume from the surface. This allows the engineer to select optimal values for the various formation characteristics that can occur during a pressure measurements sequence.

4) Sample chamber modules - Any combination of sample chambers can be assembled. A single flowline serves all the chambers. The sample chambers can be located above the probe module, allowing sampling to take place just 0.53 m (21 in.) from the bottom of the well. The standard sample chambers are available with volumes of 1, 2 $\frac{3}{4}$ and 6 gal. Each chamber has an electromechanically actuated throttle (seal) valve, which is controlled from the surface and directs sampled fluid to the selected chamber in any order. The valve can operate in one of two modes. In seal mode, the valve can be either fully open or fully closed. In throttle mode, the valve operates as a variable orifice that automatically opens and closes to maintain the flowing pressure constant. The throttle valve is a dynamic valve, constantly adjusted to maintain a specified flowline sampling pressure within an error band. In addition, the sample chamber has a drain valve for connecting the sample drainage equipment and a transport valve for sealing the sample in the module.

3.2.4.2 Optional Modules

The MDT tool is built with options to obtain a representative fluid sampling and avoid the contamination by mud filtrate. There are six available optional MDT modules that can be added to the basic tool to substantially increase its capabilities as shown in Figure 3.15.

Multisample module – Each of these modules can collect six 450 mL samples, suitable for PVT (pressure-volume-temperature) laboratory analysis, from one or more downhole locations during a single trip. Each sample is stored in an individual container that can be removed intact at surface and safely and legally

transported for analysis without fluid transfer. The number of chamber depends on the requirement and/or each company's tools' specification.

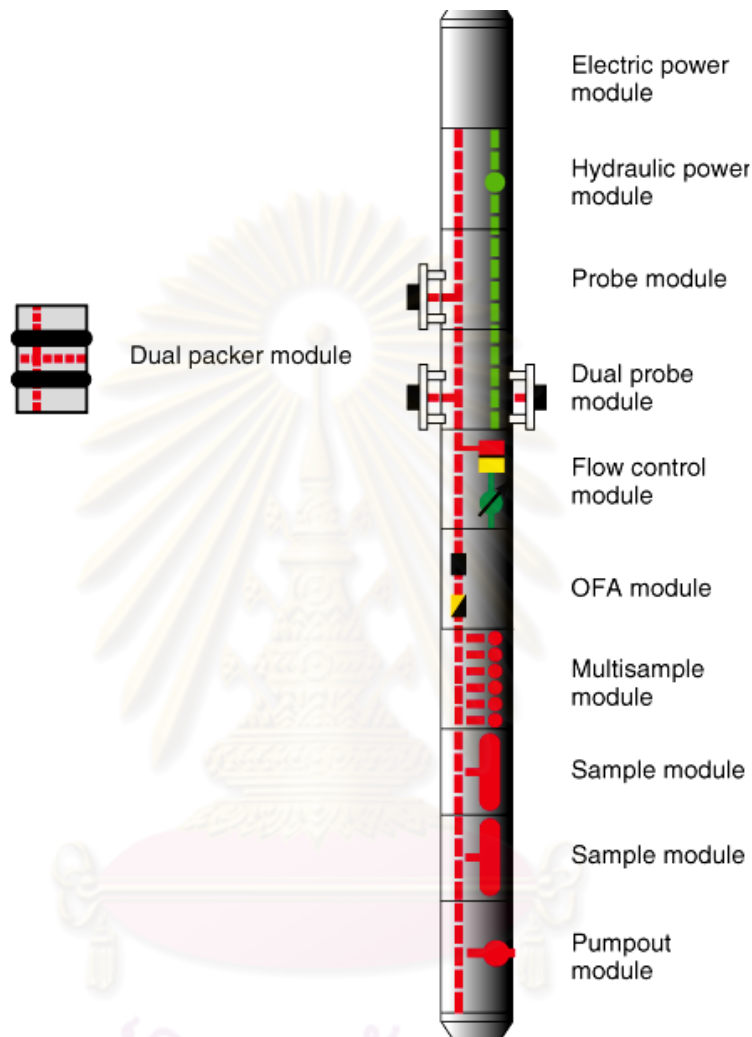


Figure 3.15: MDT tool with optional modules^[35].

Pumpout module – This module pumps formation fluid that has entered the tool out into the borehole. The module is used to dump contaminated fluid prior to sampling. It has to pump against the differential between formation flowing pressure and hydrostatic pressure in the wellbore.

Flow control module – This module provides 1-liter pressure drawdown tests with accurately controlled pressure or flow rate (1 mL/sec to 200 mL/sec). In this way, a larger drawdown than that offered by the pretest can be controlled from

surface, giving extended transients and therefore improved formation pressure measurement and permeability determination.

Multiprobe module – This module can be added to the basic probe module. This creates a tool with three probes, a sink for drawing fluid and two pressure observation probes which are the horizontal probe opposite the sink and the vertical probe above the sink. The system is usually configured with the flow control module, drawing fluid through the sink probe to set up a pressure disturbance in the formation. Analysis of transients measured at the two observation probes yields vertical and horizontal permeability estimates and enhances pressure gradient information.

Dual-packer module – This module provides two inflatable packer elements to isolate a borehole interval for testing and/or sampling. Spacing between the packer elements varies with hole size, but the minimum distance is about 3 ft. The entire borehole wall is open to the formation, so the fluid flow area is several thousand times larger than with conventional probes. The dual packer module can be used as an alternative to conventional probes.

Optical fluid analyzer (OFA) – This is a detection system to indicate fluid type. A series of optical measurement is performed in the OFA tool. These optical measurements help characterize the flowline fluid, including data differentiate hydrocarbon from oil-base drilling mud filtrate. There are several generations of the Downhole Fluid Analyzers (DFA) tool available in the current market. However, this paper will discuss on two types of the DFA tools, Live Fluid Analyzers (LFA) and Composition Fluid Analyzer (CFA).

Live Fluid Analyzer (LFA) - A new MDT module that utilizes new downhole optical techniques to analyze fluids as they flow through the MDT tool. This analyzer provides fluid type and GOR from spectrometry. The LFA spectrometer uses light in the visible and near infrared range to characterize the fluid flowing through the flowline as shown in Figure 3.16. The refractometer provides discrimination between the liquid phase and the gas phase. It builds on and improves existing optical fluid analysis with its unique ability to detect and measure dissolved methane in live fluids, whether it is dissolved in the liquid or in the gas. Oils of different types can be differentiated based on both their methane content and color^[38, 39].

Compositional Fluid Analyzer (CFA) - From spectrometry, the CFA provides fluid apparent density, GOR and compositional analysis. Near-infrared optical absorption spectrometry and fluorescence emission measurements are used to determine gas-fraction concentrations and to identify fluid types, respectively, as fluids flow through the CFA module as shown in Figure 3.17^[38, 40].

In this work, the single probe module of wireline formation tester is used to conduct controlled local production and buildup tests. The tests can be provided formation fluid samples and estimates of horizontal permeability, permeability anisotropy, and wellbore damage.

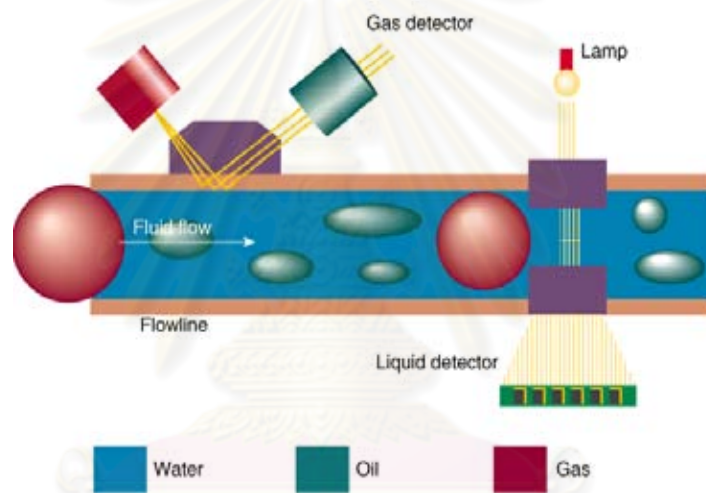


Figure 3.16: Sketch of OFA module with LFA^[39].

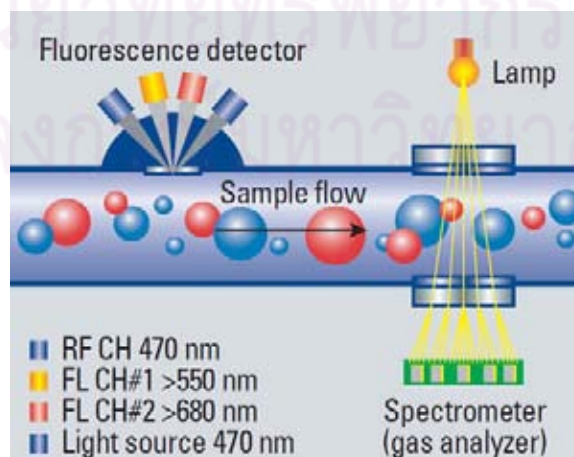


Figure 3.17: Sketch of OFA with CFA^[40].

3.3 Gas Condensate Reservoirs

Generally, there are five types of reservoir fluids. These are usually called black oil, volatile oil, retrograde gas, wet gas, and dry gas. The behavior of a reservoir fluid during production is determined by the shape of its phase diagram, the position of its critical point and the location of reservoir pressure and temperature. Table 3.1 shows generalizations for fluid type^[41].

Table 3.1: McCain's Generalizations for Fluid Types^[41].

	Black oil	Volatile Oil	Retrograde gas	Wet Gas	Dry Gas
Initial producing GOR, scf/STB	<1,750	1,750 – 3,200	>3,200	>15,000*	100,000
Initial stock-tank liquid gravity, °API	<45	>40	>40	up to 70	No liquid
Color of stocktank liquid	Dark	Colored	Lightly colored	Water white	No liquid
Phase change in reservoir	Bubble point	Bubble point	Dew point	No phase change	No phase change
Heptane-plus, mole %	> 20	20-12.5	<12.5	<4	<0.7
Oil FVF at bubble point	<2.0	>2.0	-	-	-

Gas condensate reservoirs are usually formed at higher pressure, higher temperature and deeper underground than other types of oil and gas reservoirs^[1]. Most known condensate reservoirs are found in the range of 3000 to 8000 psia and 200 to 400 °F. These gas condensate reservoirs have wide ranges of fluid composition. Approximate composition indices for gas condensate systems are the condensate/gas ratio of produced fluids (CGR) and the gravity of stock-tank oil. The CGR of gas condensate systems can vary from more than 500 bbl/MMscf (rich fluid) to less than

10 bbl/MMscf (lean fluid). The tank condensate produced from the well varies from less than 30 to more than 80°API, and more than 85% are within the range of 45 to 65°API^[42]. The added economic value of produced condensate, in addition to gas production, makes the recovery of condensate a key consideration in developing gas condensate reservoirs.

3.3.1 Gas Condensate Phase Behavior

Figure 3.18 exhibits a constant composition phase diagram of gas condensate. The phase diagram of a gas condensate system is smaller than that of oil, and the critical point is further down the left side of the envelope. It has a critical temperature less than the reservoir temperature and a cricondenthem greater than the reservoir temperature. Initially, the gas condensate is totally gas in the reservoir, point 1. As the reservoir pressure decreases, the retrograde gas exhibits a dew point, point 2. As the pressure is reduced, liquid condenses from the gas to form a free liquid in the reservoir. This liquid will normally not flow and cannot be produced until the accumulated condensate saturation exceeds the critical condensate saturation due to the relative permeability and capillary pressure effects in the porous medium. Once the reservoir pressure drops below the dew point pressure, a condensate bank tends to form around the well. This high liquid saturation results in reduced gas relative permeability and lowered well deliverability. The effect of reduced gas permeability close to the wellbore is often called "condensate blockage." This causes a loss in productivity. As the reservoir pressure further drops to lower pressure, point 3, the liquid begins to revaporize. However, the revaporization may not occur in the reservoir because the overall composition of the reservoir fluid may change during production leading to a different phase envelope.

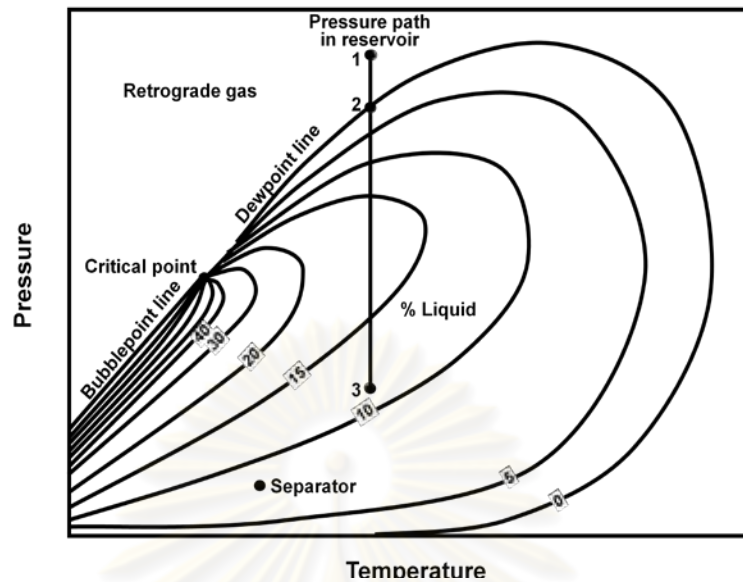


Figure 3.18: Typical gas condensate phase diagram^[41].

Figure 3.19 shows phase diagram of lean and rich gas condensate. There is no clear definition in the literature for where the transition between rich and lean condensates occurs on the phase plot. Compared to lean gas condensates, rich gas condensates have higher percentage of intermediates and C₇₊ components, higher specific gravity and lower gas-oil-ratio. The following guidelines are often used to distinguish rich condensate fluids: an initial producing gas-oil-ratio of 3300 to 5000 scf/stb^[41], heptane plus concentrations close to 12.5%^[43], maximum liquid drop-outs of up to 35% and an initial liquid yield of over 100 stb/MMscf.

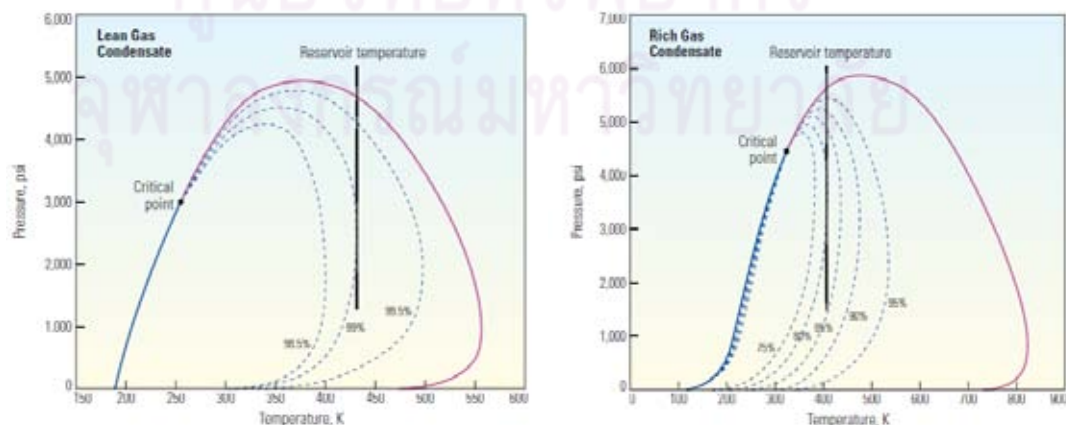


Figure 3.19: Constant composition phase diagram of a gas-condensate system^[44].

3.3.2 Compositions Changes when Condensate Drop-out

In some gas condensate reservoirs, the reservoir pressure and temperature are close to the critical point^[45]. The near critical fluid exhibits the retrograde condensation of rich gas with high shrinkage factor. For this type of reservoir, there is a high producing gas oil ratio (GOR), and light surface oil. It is very difficult to identify gas and liquid states even there is no distinct gas/oil contact can be observed in the reservoir. Figure 3.20 shows a phase diagram of a near critical condensate system, which the isotherm or pressure path is very close to the critical point. The critical point remains on the left-hand side of the pressure path. Figure 3.21 displays the phase diagram of a near critical oil phase diagram, which the critical point is now on the right-hand side of the pressure path. Therefore, small changes in reservoir condition will result in a change of fluid properties considerably^[46].

During production, the condensate or heavy liquid components (C_{7+}) start to accumulate in the reservoir while the amount of lighter components such as methane, ethane and propane decrease as they are more producible; thus causing the change in the system composition. Clearly, the details of composition evolution with time and distance are controlled by the production schedule. Hence, different fluid types may exist at different points in time and space.

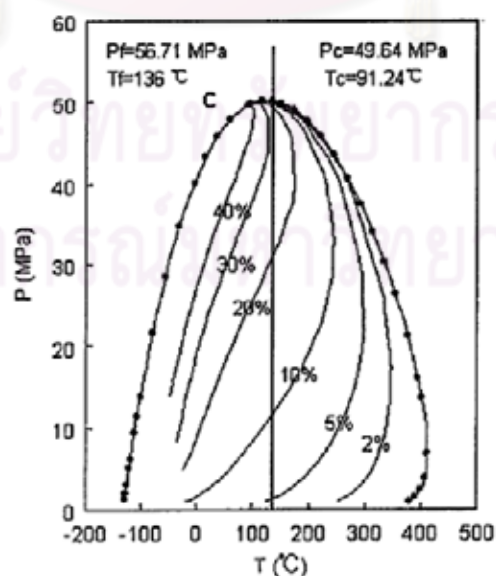


Figure 3.20: Phase diagram of a near critical point condensate system^[45].

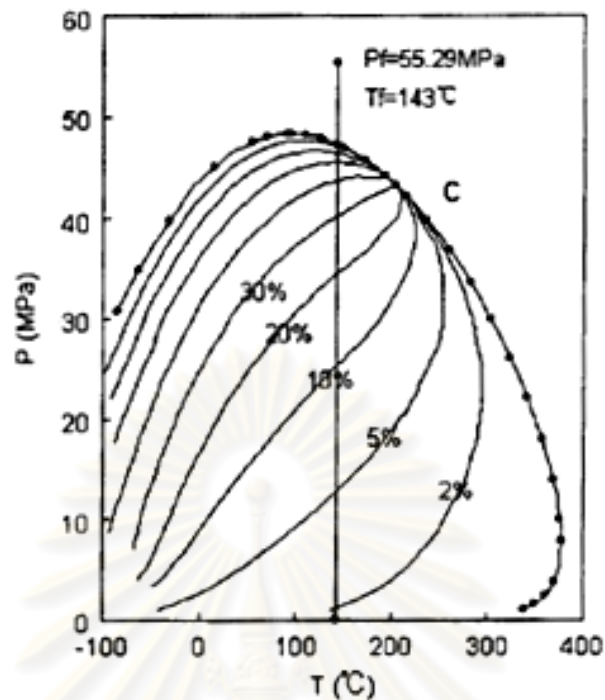


Figure 3.21: Phase diagram of a near critical point volatile oil system^[45].

In a rich gas condensate fluid during the shut-in period after the high rate production period, the condensate saturation increases near the wellbore during the shut-in period. The increase of condensate saturation as pressure increase is a behavior of volatile oil system, not the gas condensate system^[47]. In addition, there is a field in north Louisiana. It had an initial producing gas/oil ratio of 2,000 scf/STB. The stock-tank liquid was “medium orange” and had a gravity of 51.2°API, which was initially classified as volatile oil. However, during the producing history of this field the stock-tank liquid gravity steadily increased to 63°API, and the producing gas/oil ratio increased to a maximum of 29,000 scf/STB, which this produced fluid is now classified as condensate^[47].

3.3.3 Condensate Banking

Gas condensate reservoir can be divided into three radial zones^[6, 48] when a well is produced below the dew point pressure and the reservoir pressure is still above the dew point as shown in Figure 3.22.

Away from the well, region 3, where the reservoir pressure is still above the dew point pressure, contains gas only. Next, region 2, there is an intermediate region with a rapid increase in liquid saturation and a corresponding decrease in gas relative permeability. However, liquid in this region is immobile because its saturation is less than the critical condensate saturation. Closer to the well, region 1, a region forms where the liquid saturation reaches a critical value, and the fluid travels as a two-phase fluid. Regions 1 and 3 can be identified from well test data, where they create a two-region composite behavior and appear as two different mobility zones on the pressure derivative^[49].

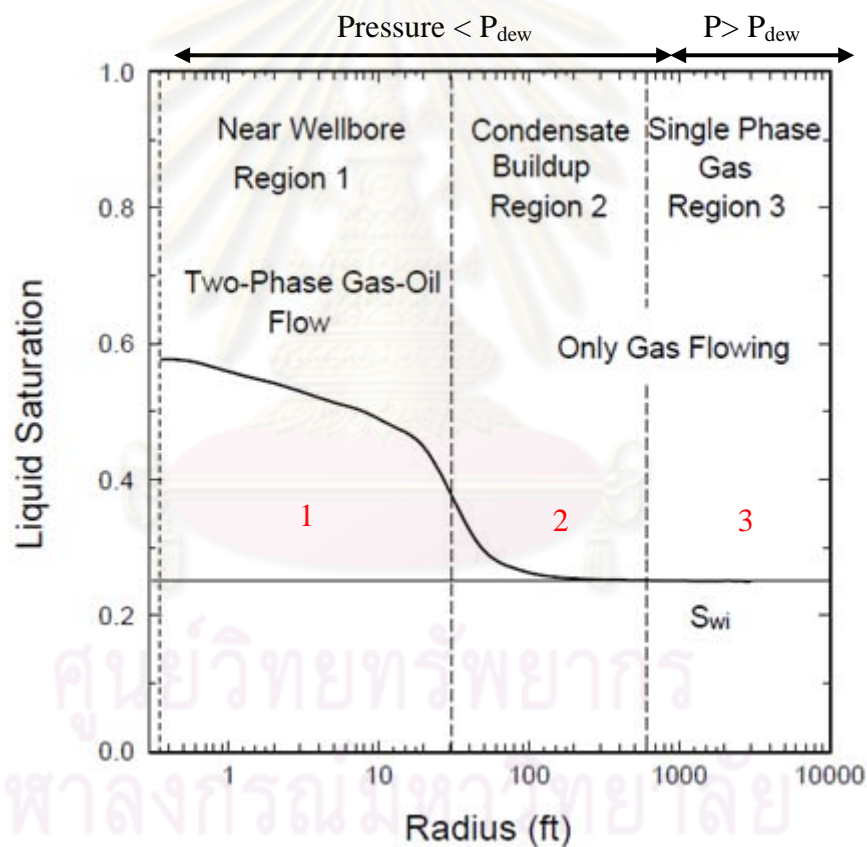


Figure 3.22: Regions around gas condensate wellbores^[4].

It may also exist a fourth region immediate vicinity to the wellbore where low interfacial tension at high gas velocity leads to a decrease of condensate saturation and an increase of gas relative permeability as shown in Figure 3.23, when the condensate saturation is high enough and there is no other effect hiding them, such

as high wellbore storage, wellbore phase redistribution, noisy data, or boundary and other reservoir effects. This phenomenon is referred to as “positive coupling” or “capillary number effect”.

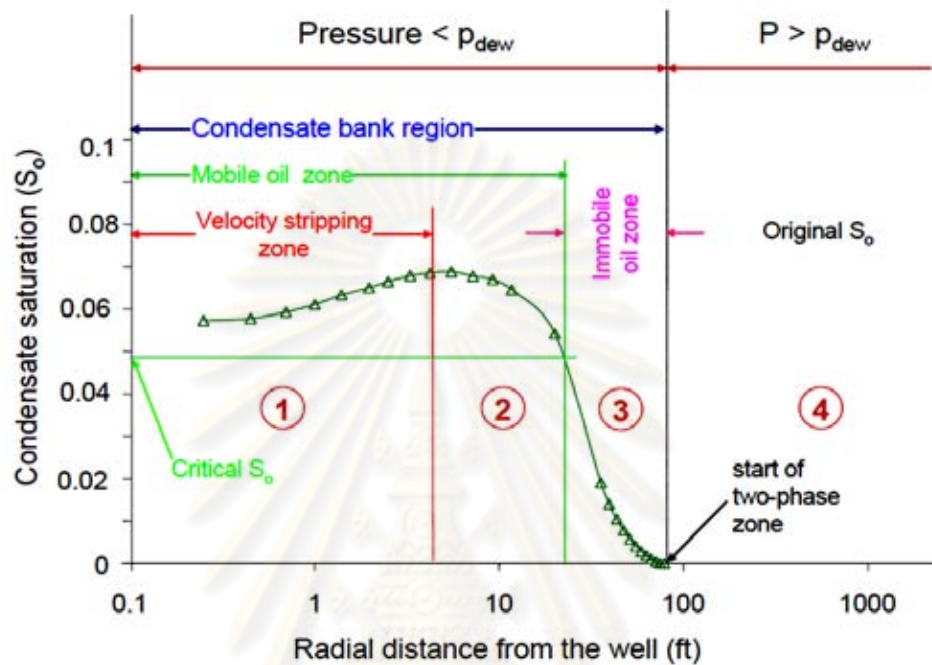


Figure 3.23: Condensate saturation profile with condensate drop-out and velocity stripping^[16].

In terms of pressure derivative, the second and third zones would not show different mobilities. This is due to two reasons: (1) both zones have high condensate saturation, and (2) the size of the second zone diminishes when the third zone is formed. When the velocity-stripping zone does not exist, there are only two different mobility zones, Regions 2 and 4, which create a *two-region composite behavior* and appear as two different mobility zones on the pressure derivative as shown in Figure 3.24. The outer mobility zone indicates a gas reservoir with initial condensate saturation whereas the inner zone represents a mobility zone with high condensate saturation.

In the near wellbore region where high velocity and low interfacial tension exist, the increased gas mobility zone occurs. This creates a *three-region composite behavior* and appears as three different mobility zones (Regions 1, 2 and 4) on the

pressure derivative when the condensate saturation is high enough and there is no other effect hiding them. This will yield three stabilizations on the derivative as shown in Figure 3.24. The early time stabilization represents gas with lower condensate saturation.

Regions 1, 2 and 3 are referred to as the condensate bank, and the decrease in gas effective permeability resulting from the existence of this condensate bank can have a significant impact on the well performance. The “condensate banking” effect is compensated by “velocity stripping” which increases the gas mobility in the immediate vicinity of the wellbore. “Velocity” or “viscous” stripping (also called “positive coupling”) occurs at high capillarity number, obtained when there is high flow rate or low interfacial tension.

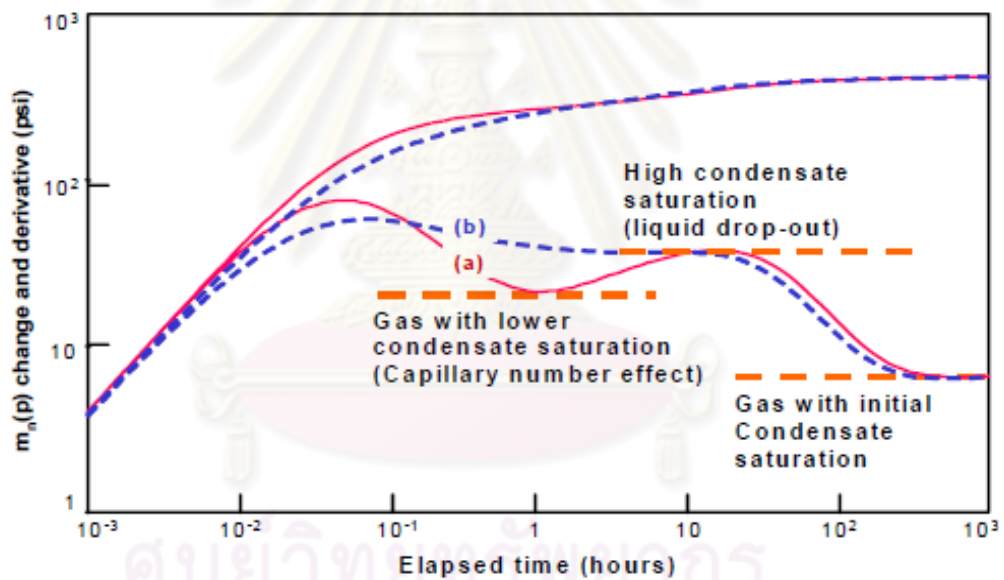


Figure 3.24: Pressure and derivative composite behaviors: (a) three-region composite; (b) two-region composite^[16, 18].

CHAPTER IV

SIMULATION RESERVOIR MODEL

In order to perform wireline formation testing, a radial grid model was used with the compositional simulator, E300 from Schlumberger, to acquire pressure responses under particular conditions. The simulation results were then interpreted using Pressure Transient Analysis (PTA) software, Saphir. As a result, reservoir properties can be obtained.

The top depth of the reservoir was set at 8500 feet. To simulate a homogenous reservoir, permeabilities in the theta and radial directions were set to be 5 mD. Therefore, the horizontal permeability (k_{xy}) is equal to 5 mD. The vertical permeability in the z-direction was set to be 1 mD. The porosity was set to be 10%. For all of our cases, the geometrical properties of the reservoir are described in Table 4.1, and the gas-oil relative permeability curve is shown in Figure 4.1.

A homogeneous reservoir with a 10 ft thick single layer is modelled where the size of the grid blocks increases logarithmically since the pressure response changes logarithmically as a function of distance. Only a single grid cell is connected to the reservoir to represent a single probe formation tester. The grid geometry containing 30 grid blocks in the radial direction, 21 grid blocks in the theta direction, and 21 grid blocks in the z-direction.

The initial size of the grid block closest to the well in all directions depends on the actual size of the probe size of the tool used to conduct the test. This work considers three probe types, which are extra-large probe size, large probe size and standard probe size. The standard probe size is mainly used and has the cross sectional area of 0.1521 square inches (probe radius of 0.220034 inches). The large and extra-large probe size has the cross sectional area of 0.8495 square inches (probe radius of 0.52 inches) and 2.011 square inches (probe radius of 0.80008 inches), respectively. Hence, the initial size of the grid block in all directions can be calculated.

The wellbore radius is set to be 0.25 ft. In the radial direction, the first grid block is 0.0796 ft. and following grid block sizes are increased logarithmically as a function of distance. In the theta direction, the first grid cell is 7.4485 degrees. Similar

to the radial direction, the angle is increased logarithmically in the clockwise and counter clockwise directions. In the z-direction, the first grid cell size is 0.0325 ft and the following grid cell sizes are also increased with logarithmic increment as showed in Table 4.2. The probe position is set to grid number 11 which is the smallest grid size located at the middle of the formation. Figures 4.2, 4.3 and 4.4 depict the side view, top view and a 3D view of the single layer radial model, respectively.

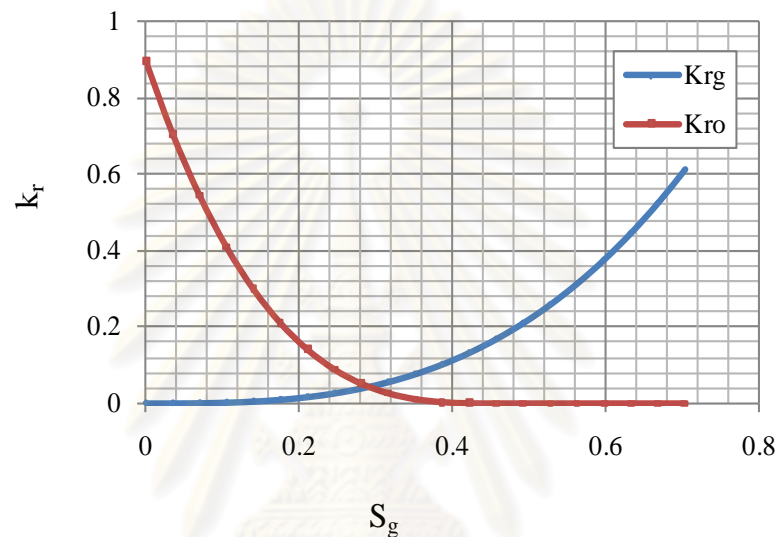


Figure 4.1: Gas-oil relative permeability curve used in the simulations.

Table 4.1: Basic reservoir rock and fluid properties for the simulation run.

Characteristic	Value
Porosity	0.1 fraction
Horizontal permeability	5 mD
Vertical permeability	1 mD
Connate water saturation	0.297 fraction
Wellbore radius	0.25 ft
External radius (r_e)	1000 ft
Top depth	8500 ft
Reservoir thickness	10 ft
Number of nodes – radial direction	30
Number of nodes – theta direction	21
Number of nodes – vertical direction	21

Table 4.2: Summary of grid geometry for the single layer radial model

Radial direction		Theta direction		Vertical direction	
Grid	grid size (ft)	grid	grid size (degree)	grid	grid size (ft)
1	0.0796	1	7.4485	1	1.6515
2	0.1050	2	8.5832	2	1.1150
3	0.1384	3	9.8907	3	0.7528
4	0.1825	4	11.3975	4	0.5082
5	0.2406	5	13.1338	5	0.3431
6	0.3172	6	15.1347	6	0.2317
7	0.4183	7	17.4403	7	0.1564
8	0.5515	8	20.0972	8	0.1056
9	0.7271	9	23.1589	9	0.0713
10	0.9587	10	26.6869	10	0.0481
11	1.2640	11	30.7525	11	0.0325
12	1.6665	12	30.7525	12	0.0481
13	2.1973	13	26.6869	13	0.0713
14	2.8971	14	23.1589	14	0.1056
15	3.8197	15	20.0972	15	0.1564
16	5.0362	16	17.4403	16	0.2317
17	6.6401	17	15.1347	17	0.3431
18	8.7548	18	13.1338	18	0.5082
19	11.5430	19	11.3975	19	0.7528
20	15.2191	20	9.8907	20	1.1150
21	20.0661	21	8.5832	21	1.6515
22	26.4567	Sum	360.0000	Sum	10.0000
23	34.8825				
24	45.9917				
25	60.6390				
26	79.9510				
27	105.4135				
28	138.9852				
29	183.2487				
30	241.6091				
Sum	1000.0000				

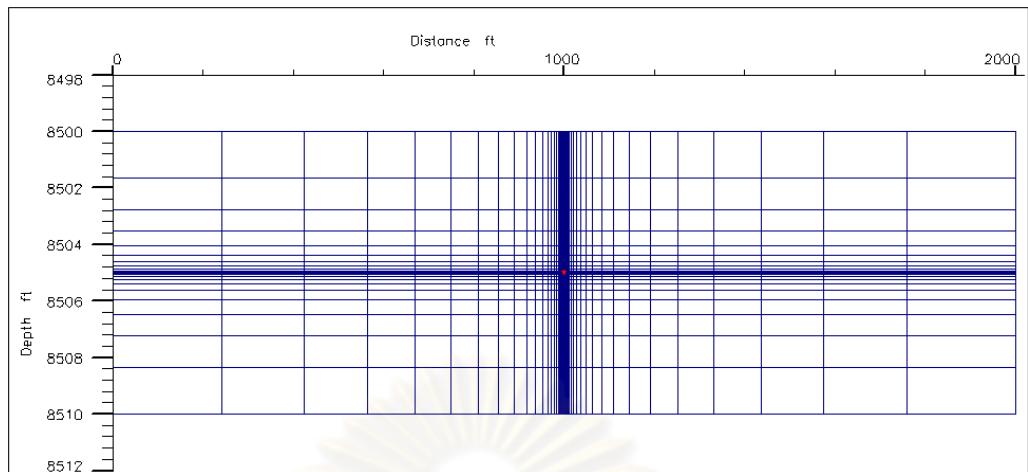


Figure 4.2: Side view of a single layer radial model.

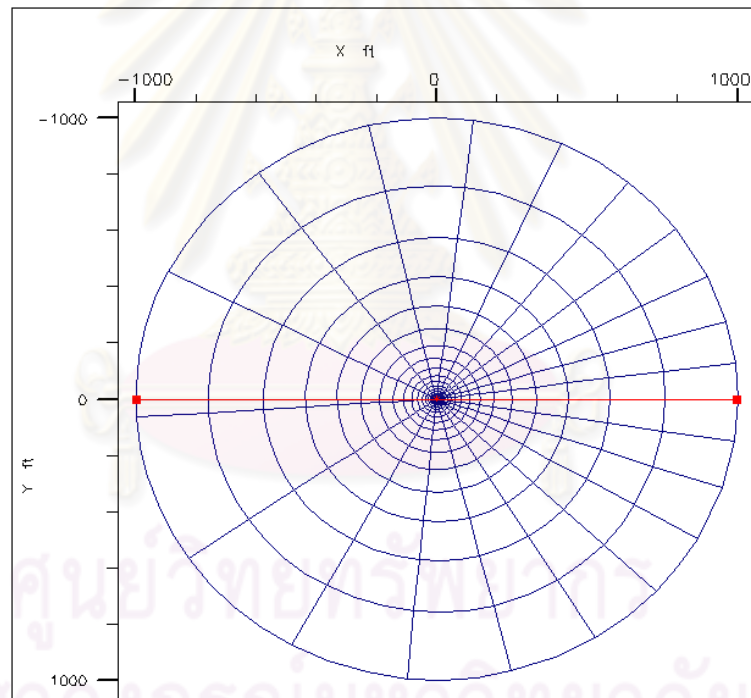


Figure 4.3: Top view of a single layer radial model.

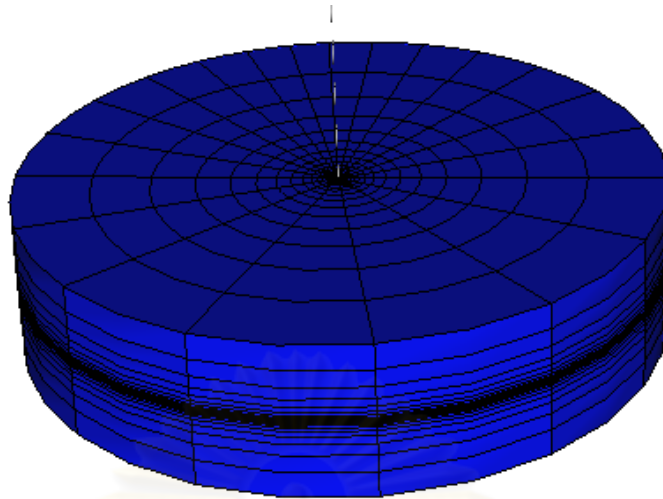


Figure 4.4: 3D view of a single layer radial model.

Three fluids with different degrees of richness in condensate which are fluids A, B and C were used in this study. Fluid A and C are obtained from Al-Lamki's work^[47] whereas Fluid B is obtain from Kenyon's work^[50]. All of fluid properties and EOS used in this study are the same as presented in those papers. The compositions and basic properties of Fluids A, B and C are shown in Tables 4.3 and 4.4 respectively. Figure 4.5 shows liquid drop-out for Fluid A, B and C. The phase behaviors calculated by PVTi program are shown in Figures 4.6, 4.7 and 4.8 respectively. Fluid A has a maximum liquid drop-out of 1.02% and was modeled using Soave-Redlich-Kwong (SRK) equation of state with 12 components including water. Fluid B has a maximum liquid drop-out of 3.41% and was modeled using Peng-Robinson (PR) equation of state with 8 components including water. Fluid C has a maximum liquid drop out of 19.24% and was modeled using Soave-Redlich-Kwong (SRK) with 10 components including water. According to the maximum liquid drop-out, Fluid A is very lean gas condensate, Fluid B is lean gas condensate and Fluid C is rich gas condensate.

The models were simulated with a sequence of drawdown and build-up period. Wellbore storage and initial skin factor were not included in the models since the main concern for this study is to evaluate the effect of the condensate bank on pressure behavior in wireline formation test. To simplify the simulation, capillary number effect and the velocity dependent relative permeability options were also not

used. In addition, the examples of time steps and data file used in the simulation are presented in Appendix A and B respectively.

Table 4.3: Fluid composition of Fluid A, Fluid B and Fluid C.

Fluid A				
Component	Mole fraction	MW	Critical Pressure (psia)	Critical Temperature (R)
N2	0.015800	28.01	493.1	227.2
CO2	0.024100	44.01	1071	547.6
C1	0.796000	16.04	666.7	343
C2	0.068700	30.07	707.8	549.8
C3	0.035700	44.1	615	665.6
n-C4	0.018900	58.12	548.8	765.2
n-C5	0.008800	72.15	488.1	845.4
PC1	0.026155	109.03	408	1005.2
PC2	0.004584	175.59	302	1222.6
PC3	0.001235	263.51	172	1411.5
PC4	0.000026	422.8	95	1664.9

Fluid B				
Component	Mole fraction	MW	Critical Pressure (psia)	Critical Temperature (R)
N2+C1	0.80447	16.1464	664.579	341.341
CO2+C2+C3	0.11758	35.7582	745.052	586.362
C4+C5+C6	0.03195	67.645	499.146	820.504
C7-C9	0.02361	103.069	406.819	992.92
C10-C12	0.00982	146.834	314.444	1117.11
C13-C17	0.00793	200.222	262.234	1245.979
C18-C78	0.00463	322.89	210.749	1505.4

Fluid C				
Component	Mole fraction	MW	Critical Pressure (psia)	Critical Temperature (R)
CO2	0.01210	44.01	1071.33	548.46
N2	0.01940	28.01	492.31	227.16
C1	0.65990	16.04	667.78	343.08
C2	0.08690	30.07	708.34	549.77
C3	0.05910	44.10	618.70	665.64
C ₄₋₆	0.09670	66.87	514.93	806.54
C ₇ P ₁	0.04745	107.78	410.75	838.11
C ₇ P ₂	0.01515	198.56	247.56	1058.04
C ₇ P ₃	0.00330	335.20	160.42	1291.89

Table 4.4: Basic fluid properties of Fluid A, Fluid B and Fluid C.

Fluid properties	Fluid A	Fluid B	Fluid C
Maximum liquid drop out, %	1.02	3.41	19.24
Reservoir temperature, F	251	270	230
Initial reservoir pressure, psia	3474	5850	3730
Dew point pressure, psia	3468	5847	3724
Critical condensate saturation, fraction	0.244	0.246	0.240

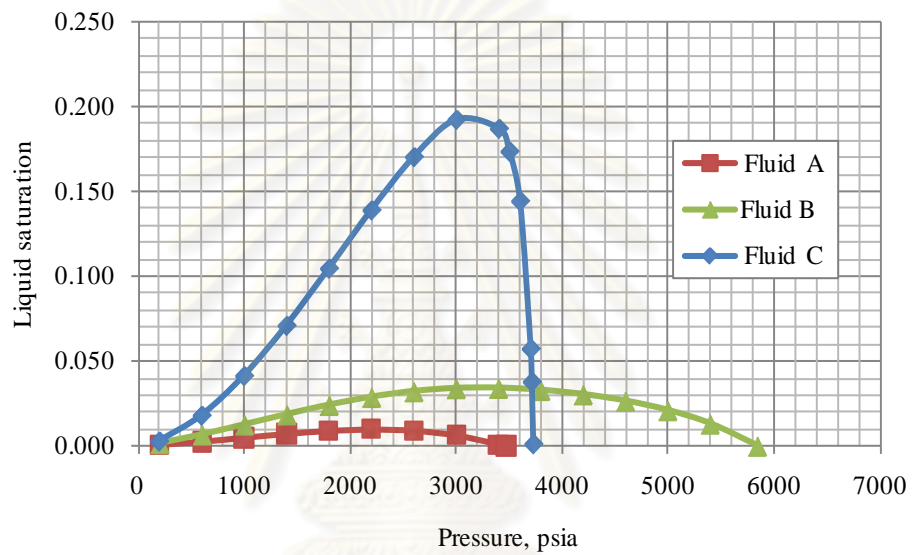


Figure 4.5: Liquid drop-out for Fluid A, B and C.

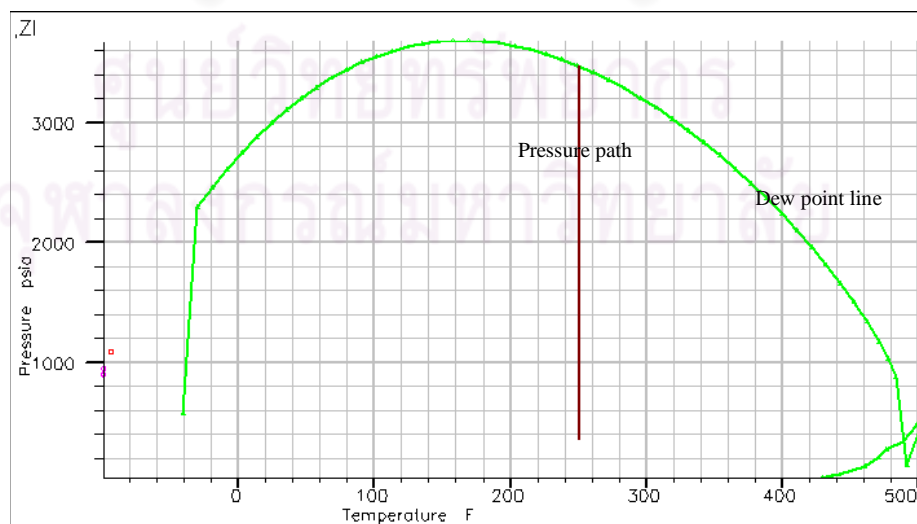


Figure 4.6: Phase behavior of Fluid A.

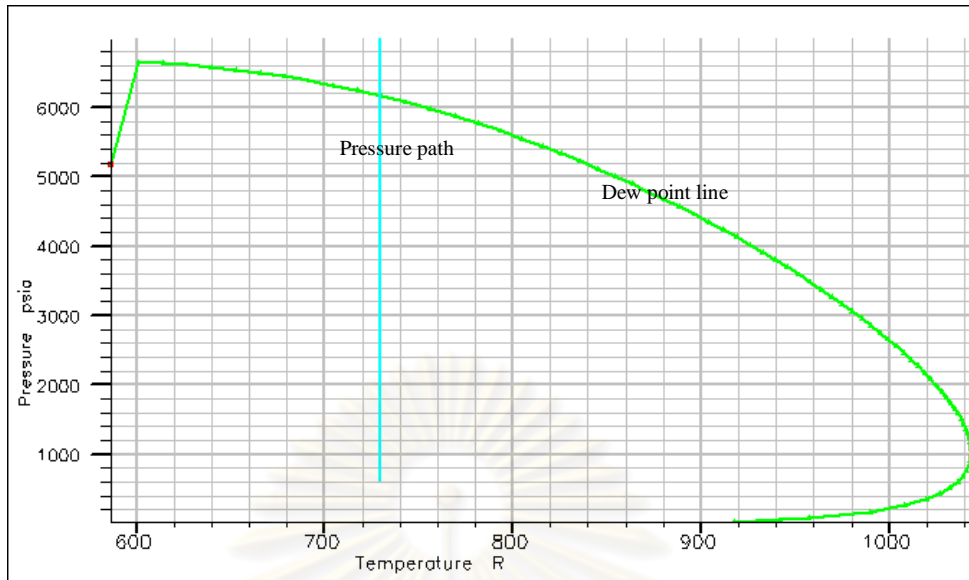


Figure 4.7: Phase behavior of Fluid B.

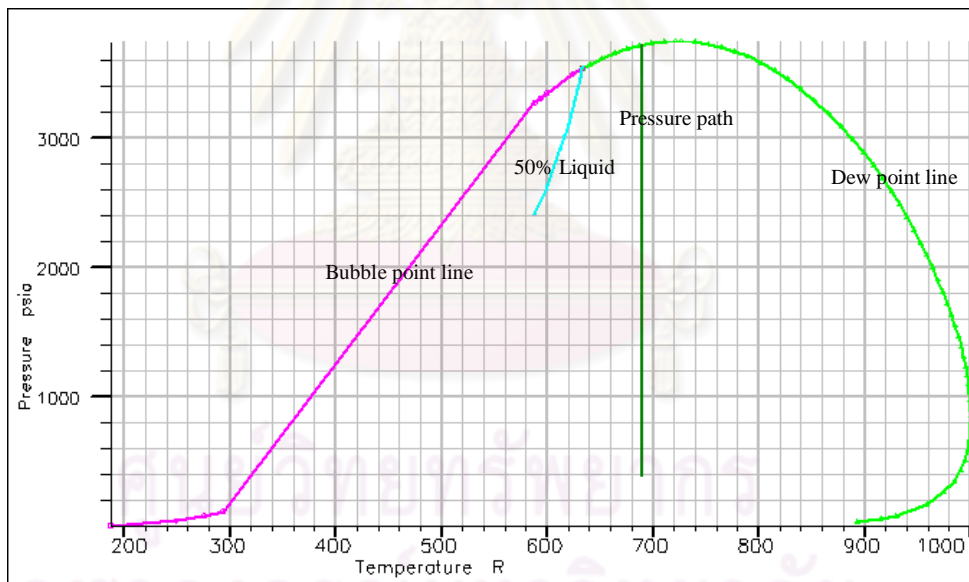


Figure 4.8: Phase behavior of Fluid C.

CHAPTER V

SIMULATION RESULT AND ANALYSIS

This chapter describes results from the simulation work using generic rich and lean fluids for single layer homogeneous gas condensate reservoir. A reservoir simulator, E300, was used to simulate pressure transient responses from the wireline formation tester. Then, the pressure transient analysis software, Saphir, was used to estimate reservoir parameters. A number of cases were generated in order to investigate the effect of condensate dropout on the pressure behavior obtained from formation tester data and evaluate the applicability of wireline formation test in gas condensate reservoir whether it can detect the increasing size of condensate bank. The effect of condensate bank on estimates of reservoir parameters was examined by comparing the estimated reservoir parameters obtained from Pressure Transient Analysis (PTA) technique with the actual value used in the simulation.

5.1 Behavior above Dew Point Pressure (Model Validation)

The first scenario was run using lean fluid (Fluid A) to validate the model. The initial reservoir pressure was set at 6000 psia, much higher than the dew point pressure of 3468 psia, in order to monitor single phase gas behavior. Hence, the flowing probe pressure is still higher than the dew point pressure. Initially, the radial and theta permeability was input as 5 mD with the vertical permeability of 1 mD; hence, permeability anisotropy (k_z/k_{xy}) is equal to 0.2. The formation test was simulated with a sequence of drawdown and build-up periods. The simulated probe was designed to set at the middle of the formation. Fluid was drawn with a flow rate of 1 Mscf/d for 1 hr, and followed by a shut-in period or buildup test of 1 hr. The test period in the model is longer than that in the actual formation test to define all possible flow regimes such as radial flow. In addition, wellbore storage was set to zero; therefore, we should not see the effect of wellbore storage in the derivative. A schematic of reservoir description for this case is shown in Figure 5.1. The pressure and flow rate profile from the simulation are shown in Figure 5.2.

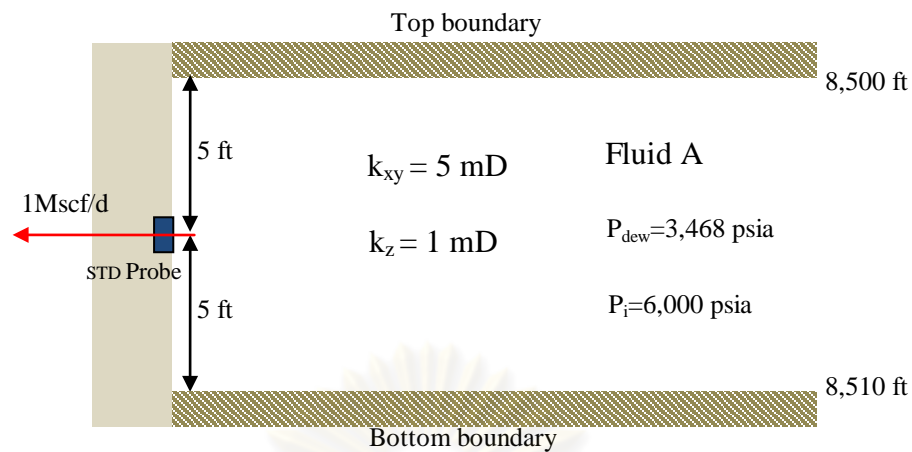


Figure 5.1: A schematic of reservoir to study behavior below dew point pressure.

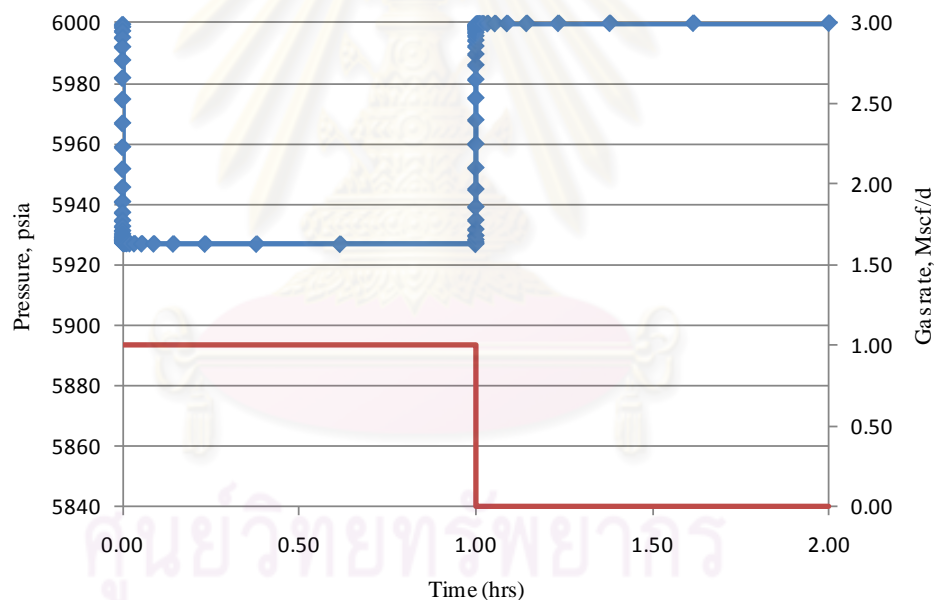


Figure 5.2: Pressure and flow rate profile of lean Fluid A when the flowing probe pressure is much higher than the dew point pressure.

After running an analytical model using formation test option, the values of k_{xy} , k_z/k_{xy} , skin and radius of investigation were estimated using pressure transient analysis software. Figure 5.3 shows the log-log derivative plot of the build-up period. An analytical model is shown as a green line and the pressure derivative is shown as a red one. As can be seen in the figure, an analytical model shown as a green line the

spherical flow model can be matched with the curve at time before 0.01 hr. At late times, after 0.03 hr, the radial flow model can also be matched with the curve.

As expected, there is no condensate drop-out in the near wellbore region since the flowing probe pressure is much higher than the dew point pressure. The derivative exhibit two responses which are (1) a negative half slope straight line corresponding to spherical flow near the wellbore where there is a vertical contribution to flow, open interval smaller than the drained interval and (2) a zero slope straight line corresponding to radial flow regime.

Figure 5.4 shows grid block condensate saturation and pressure at the end of the drawdown period as a function of radial distance. From this figure, it is clear that the liquid saturation is zero for all grid cells since the flowing probe pressure is higher than the dew point pressure.

In addition, the compositions of all components are the same during the drawdown period as illustrated by concentration of CH_4 in Figure 5.5 as an example and are the same for the entire of radial distance as in Figure 5.6. Hence, phase behavior is the same during the test duration.

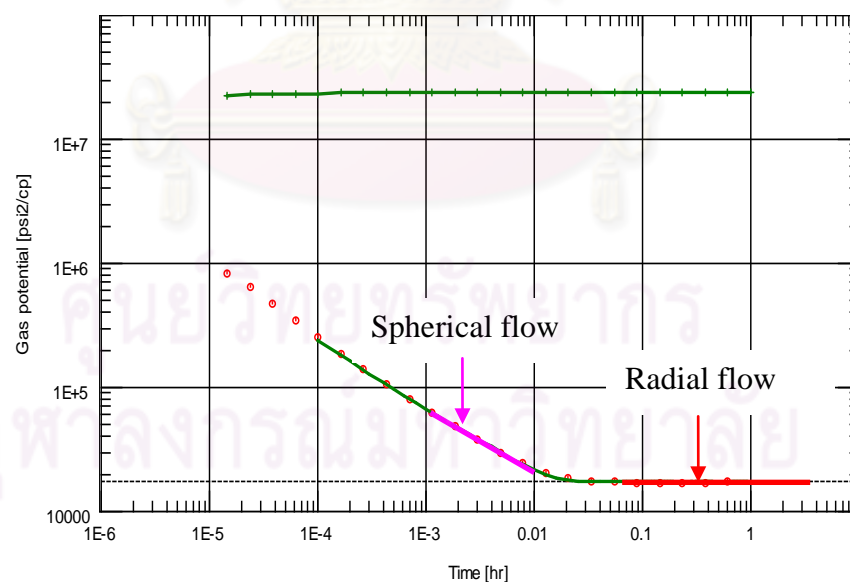


Figure 5.3: Derivative plot of lean Fluid A when the probe pressure is much higher than the dew point pressure.

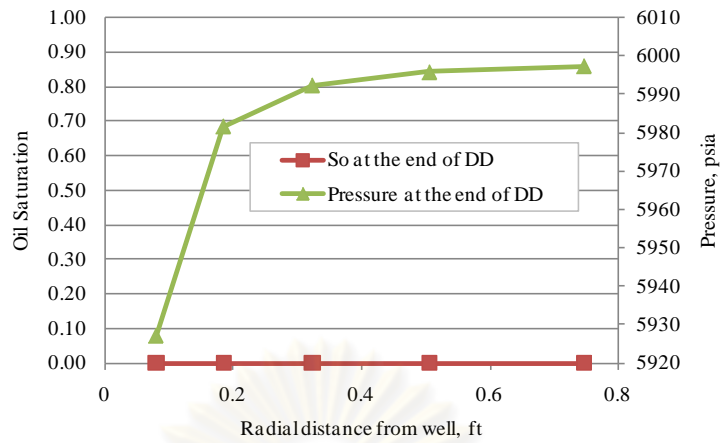


Figure 5.4: Condensate saturation and pressure profile at the end of drawdown of lean Fluid A when the probe pressure is much higher than the dew point pressure.

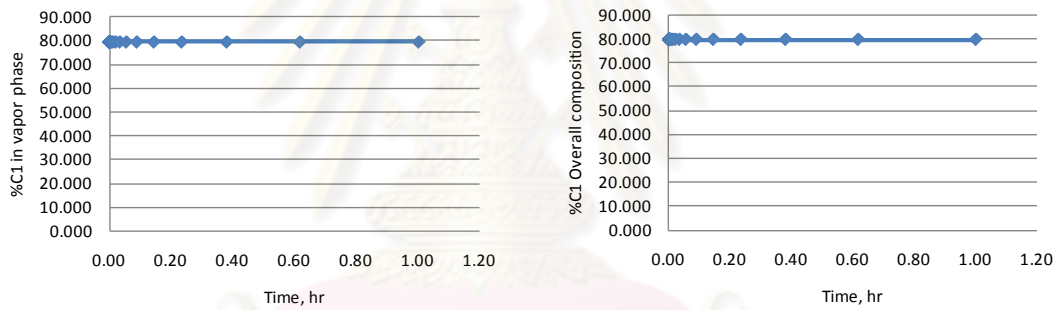


Figure 5.5: Composition of C_1 at probe cell versus time during drawdown period of lean Fluid A when the probe pressure is much higher than the dew point pressure.

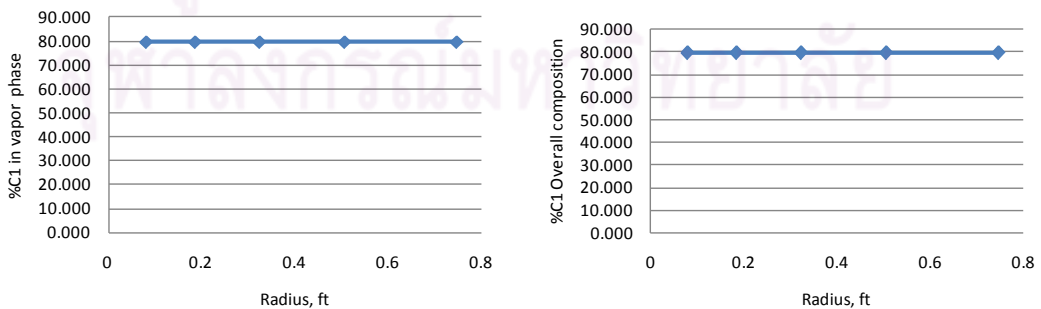


Figure 5.6: Composition profile of C_1 at the end of drawdown of lean Fluid A when the probe pressure is much higher than the dew point pressure.

Table 5.1 shows the interpretation results. Gas effective permeability (k_{xy}) was estimated to be 2.93 mD. This is consistent with the input absolute horizontal permeability of 5 mD and the end point gas relative permeability of 0.61 with the error of 4% (the gas effective permeability corresponding to absolute permeability of 5 mD is 3.05 mD). The spherical flow analysis shows the permeability anisotropy (k_z/k_{xy}) of 0.224 which has an error of 12%. This result confirms that the estimated permeability from WFT pressure response is reliable.

Table 5.1: Interpreted results when the probe pressure is much higher than the dew point pressure.

Drawdown rate (Mscf/d)	Interpreted			Error			Skin	R_{inv} (ft)
	k_{xy} (mD)	k_z/k_{xy}	Calc. k_z (mD)	k_{xy} (%)	k_z/k_{xy} (%)	k_z (%)		
1.00	2.93	0.22	1.08	-3.93	12.00	7.59	0.00	87.80

5.2 Behavior below Dew Point Pressure

The objective of this section is to investigate the pressure behavior below dew point pressure. The simulation was run with lower initial reservoir pressure. The initial reservoir pressure was set to be 3474 psia. As a result, the flowing probe pressure drops below the dew point pressure. The schematic of the reservoir used in this case is shown in Figure 5.7. The lean Fluid A was drawn for 1 hr with flow rate of 1 Mscf/d and 1 hr of buildup test. The pressure and flow rate profile are shown in Figure 5.8. As seen from the figure, the flowing probe pressure is below the dew point pressure.

Figure 5.9 shows the log-log derivative plot of build-up test with an analytical model using formation test option. An analytical model is shown as a green line and the pressure derivative is shown as a red line. As can be seen from this figure, the spherical flow model can be matched to the data at time between 0.001 hr to 0.01 hr. At late times, after 0.05 hr which corresponds to 19.58 ft radius of investigation, the radial flow model can be matched to the data. The derivative plot shows two negative half slope parallel straight lines indicating two different spherical mobilities, a

spherical composite behavior, and followed by a zero slope straight line representing radial flow. Actually, the first negative half slope straight line is not clearly seen in this case since there is only one pressure point in this line. Since, wellbore storage was set to zero, the deviation from typical spherical flow behavior, as shown in previous section, should be due to liquid drop-out.

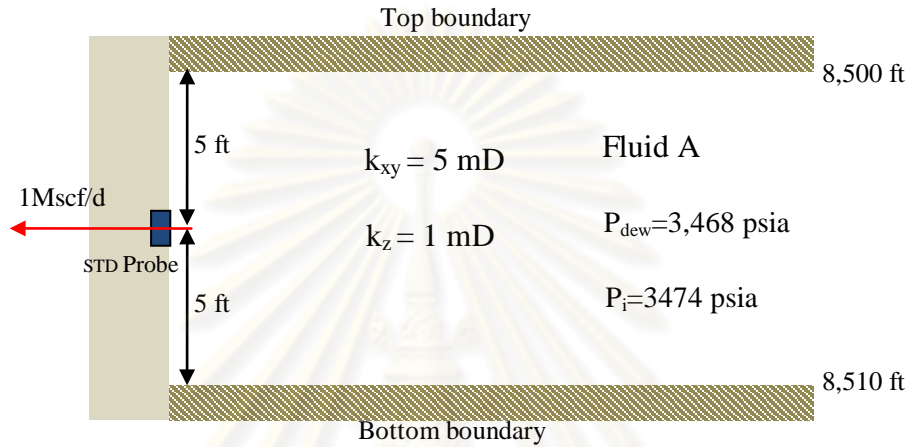


Figure 5.7: A schematic of reservoir to study behavior below the dew point pressure.

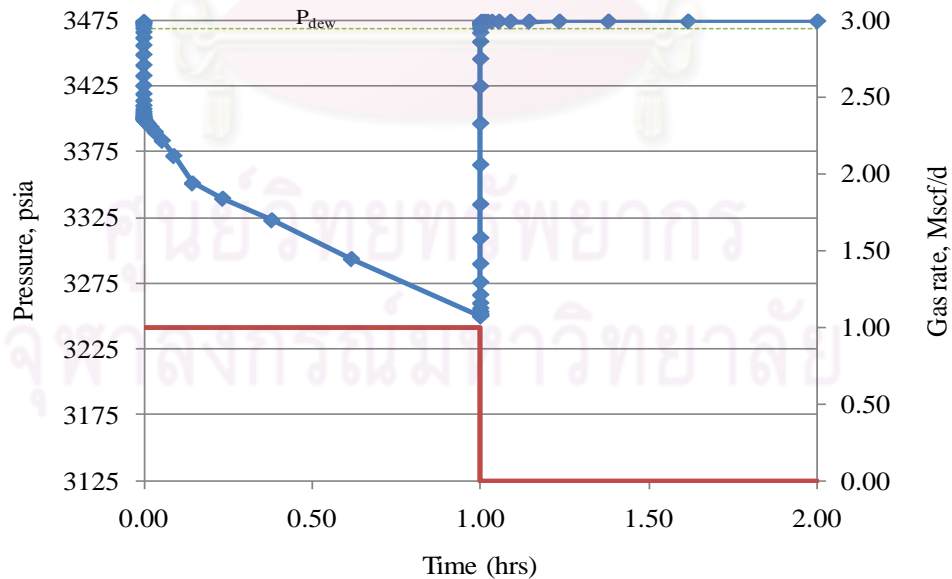


Figure 5.8: Pressure and flow rate profile of lean Fluid A when the flowing probe pressure is below the dew point pressure.

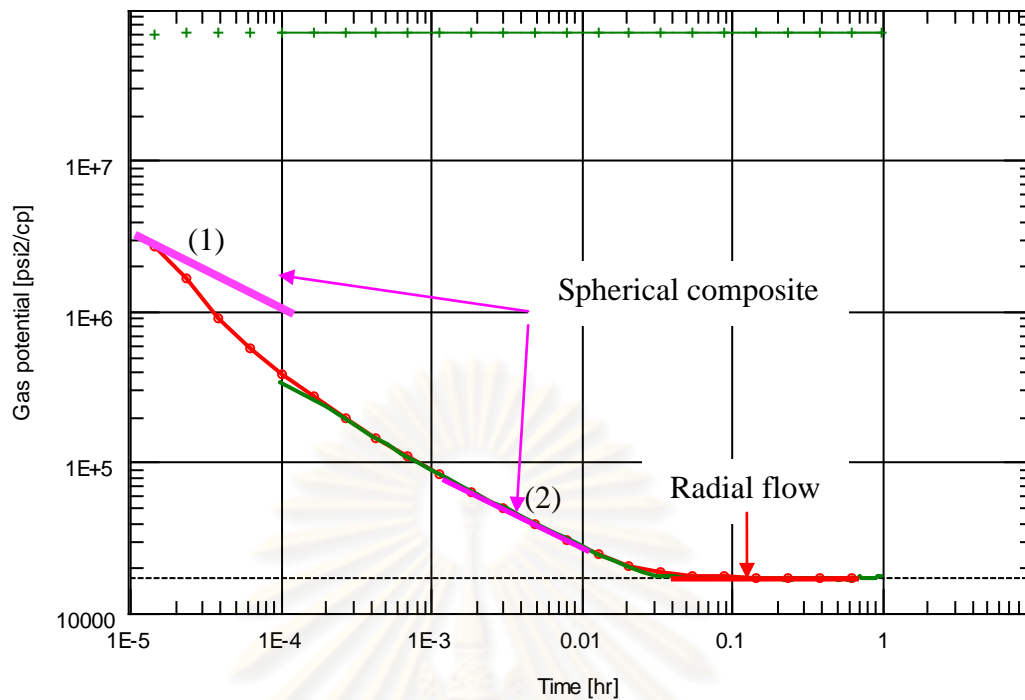


Figure 5.9: Derivative plot of lean Fluid A when the probe pressure is below the dew point pressure.

At the end of drawdown period, the reservoir can be divided into three radial zones as shown in Figure 5.10. R1 represents the probe grid block; R2 represents the block next to the probe cell in the radial direction; R3 and R4 are the blocks further away from the wellbore into the reservoir in the radial direction. As Fluid A is being produced, the pressure decreases from the reservoir to the well, leading to condensation of liquid from the gas. The probe pressure drops below the dew point pressure but the reservoir pressure is still above the dew point pressure. Away from the well where the distance is greater than r_{dew} of 0.42 ft, zone3, and the pressure is still above the dew point pressure, there is gas only. Closer to the well, there is an intermediate region between 0.18 ft to 0.42 ft, zone2, with a rapid increase in liquid saturation and a corresponding decrease in gas relative permeability as shown in Figure 5.11. However, liquid in this region is immobile because its saturation is less than the critical condensate saturation. Closer to the well with the distance lesser than 0.18 ft, zone1, the liquid saturation reaches a critical value, and the fluid travels as a two-phase fluid which can be confirmed by the fact that the oil relative permeability is more than zero as shown in Figure 5.11.

The radius of investigation to the radial flow regime is 19.58 ft which is larger than the condensate bank region of 0.42 ft. Hence, all three zones exist within the spherical flow regime. This yields a spherical composite behavior with the upper negative half slope straight line corresponding to the spherical mobility of condensate bank and the lower negative half slope line corresponding to the spherical mobility of the original gas.

Figure 5.12 shows the phase envelope of each block near the probe cell at the end of drawdown. At the end of drawdown, phase envelopes for different radial distance are not the same as that of initial fluid, ZI. At the probe cell and the block nearby the probe cell, R1 and R2, fluid behaves like a volatile oil system. Away from the probe block, R3 and R4, fluid behaves like a gas condensate but the fluid at R3 becomes richer than that at R4 which has the same phase envelope as the initial fluid. Therefore, the fluid behaves as a volatile oil for radius less than approximately 0.18 ft, R2. In summary, the fluid in the outer cell behaves like a gas condensate but the fluid in the inner cell behaves like a volatile oil.

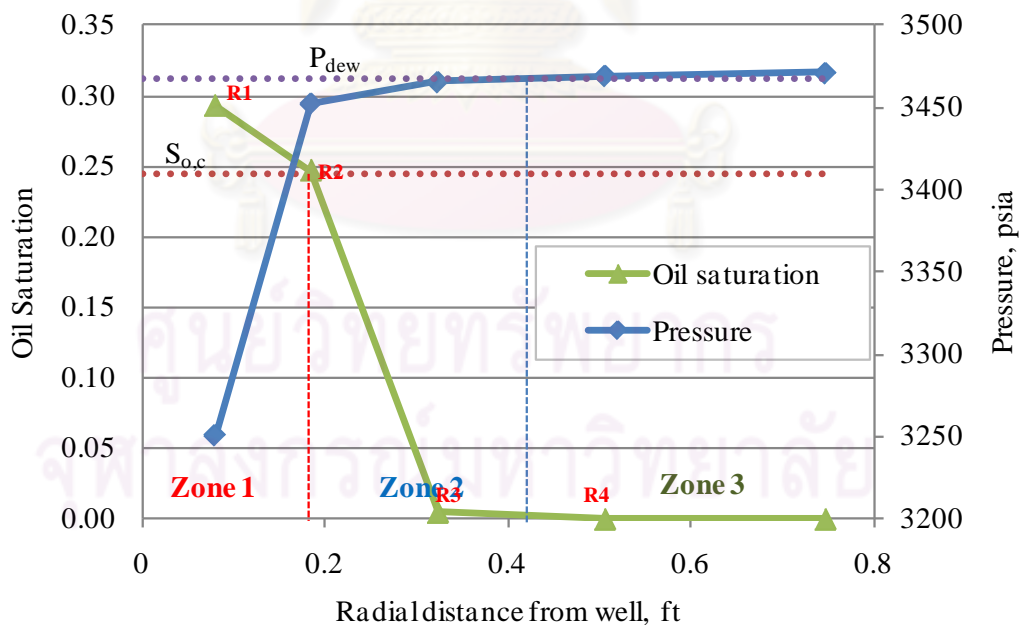


Figure 5.10: Condensate saturation and pressure profile at the end of drawdown of lean Fluid A when the probe pressure is below the dew point pressure.

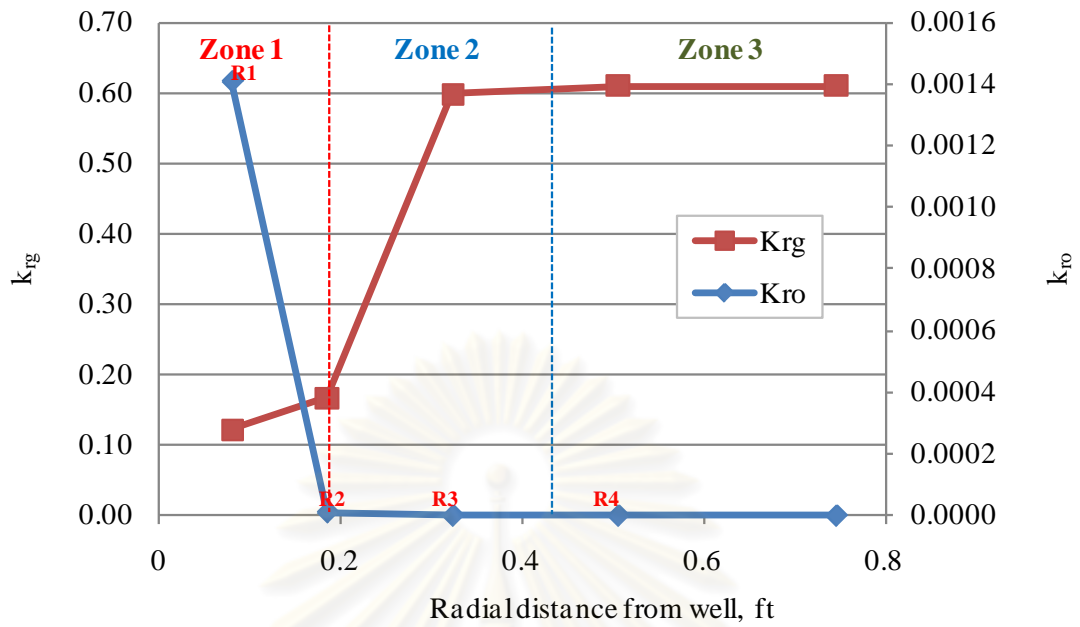


Figure 5.11: Relative permeability profile at the end of drawdown of lean Fluid A when the probe pressure is below the dew point pressure.

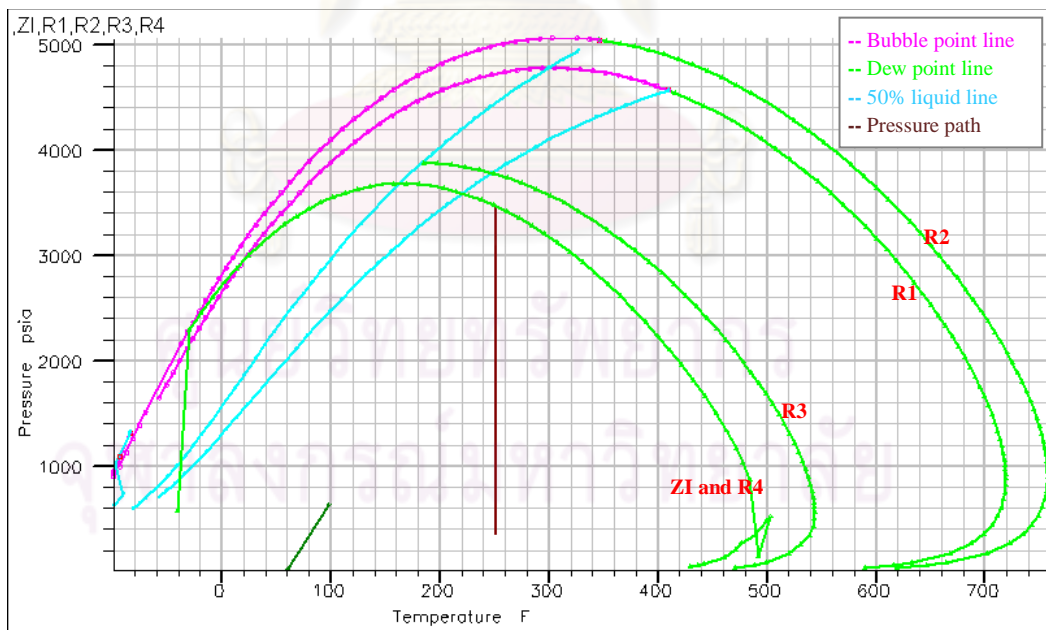


Figure 5.12: Phase behavior of the block near the probe cell at the end of drawdown of lean Fluid A when the probe pressure is below the dew point pressure.

There is a difference in fluid composition in the radial distance at the end of drawdown as depicted in Figure 5.13. When the bottomhole pressure drops below the dew point pressure, the condensate bank starts to form in block R1, R2 and R3 in this case. The heavy component like C_5 drops out of the gas phase and accumulates near the wellbore. This is why C_5 in the gas phase decreases toward the wellbore and C_5 in the liquid phase increases toward the wellbore. The light component like C_1 in the gas phase increases toward the wellbore and C_1 in the liquid phase decreases toward the wellbore. The overall C_1 composition decreases toward the wellbore, indicating that the mixture fluid near the wellbore becomes heavier. This is why the fluid near the wellbore in R1 and R2 grid blocks behaves like a volatile oil system.

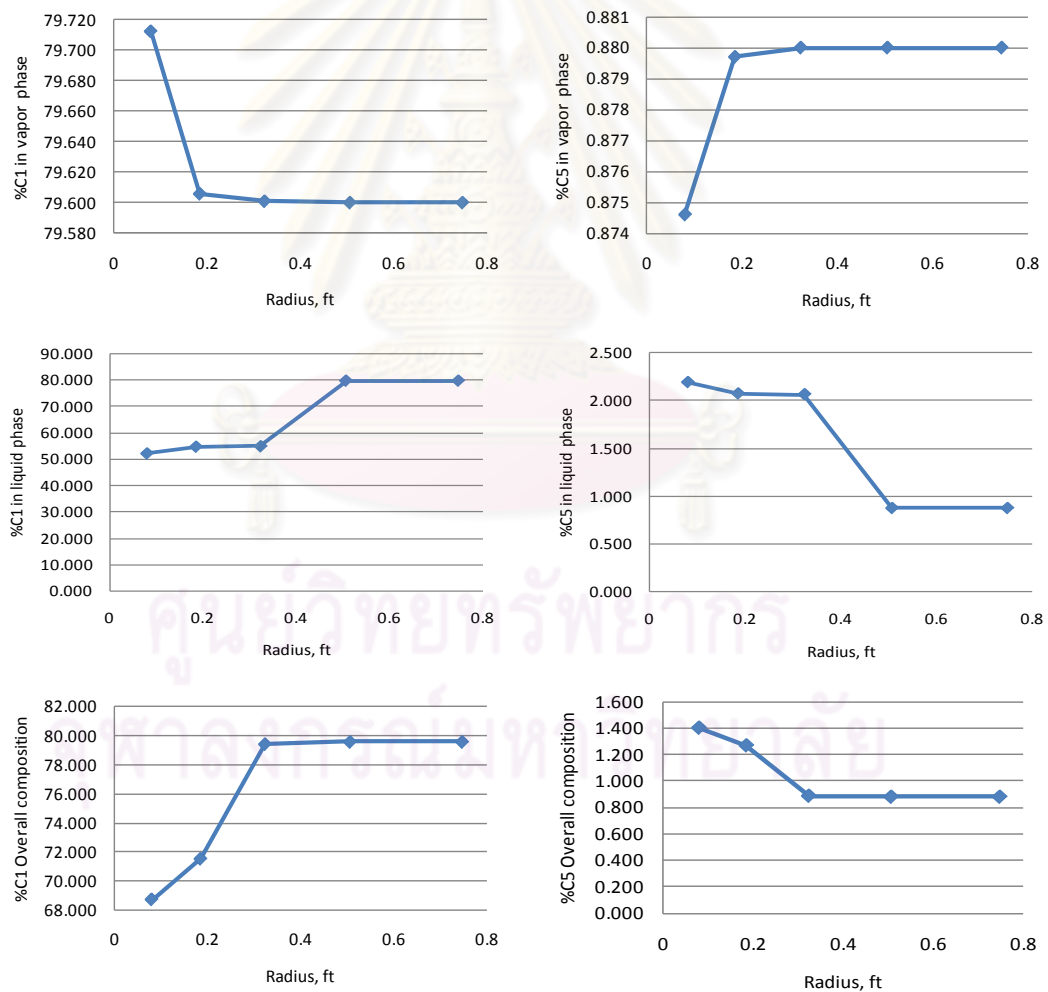


Figure 5.13: Composition profile of C_1 and C_5 at the end of drawdown of lean Fluid A when the probe pressure is below the dew point pressure.

From analysis of pressure data, the interpreted result in Table 5.2 shows that WFT pressure response in lean gas condensate reservoir can be used to estimate reservoir permeability with an acceptable value even though condensate banking occurs. The error from the interpretation is approximately the same as the one in the previous case. The error of estimated horizontal permeability (k_{xy}) is about 3.93%; the error of estimated permeability anisotropy is 13%, and the error of estimated vertical permeability (k_z) is 8.55%.

Table 5.2: Summary of interpreted results when the probe pressure is below the dew point pressure.

Drawdown rate (Mscf/d)	Interpreted			Error			Skin	R_{inv} (ft)	k_z/k_{xy} (early time)
	k_{xy} (mD)	k_z/k_{xy}	Calc. k_z (mD)	k_{xy} (%)	k_z/k_{xy} (%)	k_z (%)			
1.00	2.93	0.23	1.09	-3.93	13.00	8.55	1.02	65.7	0.039

5.2.1 Phase Behavior during Drawdown Period

As the pressure drops below the dew point, the oil condenses from the gas, and zone 2 develops. The oil accumulates until its saturation reaches the critical condensate saturation. Zone 1 develops at the 31st time step, T31, or at time of 0.0128 hr or 46 sec as shown in Figure 5.14.

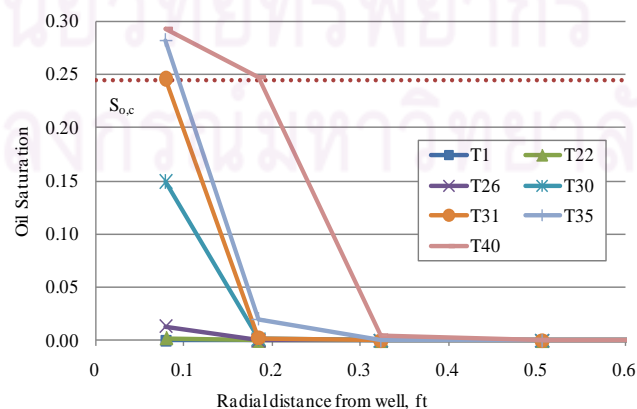


Figure 5.14: Condensate saturation profiles during drawdown period of lean Fluid A when the probe pressure is below the dew point pressure.

As the original gas flows through Region 2 in the reservoir, its composition changes. The flowing gas becomes leaner because of condensation of intermediate and heavy components. Consequently, the oil in zones 1 and 2 becomes heavier as the pressure decreases. Figure 5.15 indicates that the overall mixture anywhere in zone 1 or 2 become heavier and the flowing gas becomes leaner as the pressure decreases below the dew point pressure. For example, at T31, the overall C_1 mole fraction decreases towards the well bore, indicating that the mixture becomes heavier. On the other hand, the vapor phase or the flowing gas becomes leaner as we approach the wellbore.

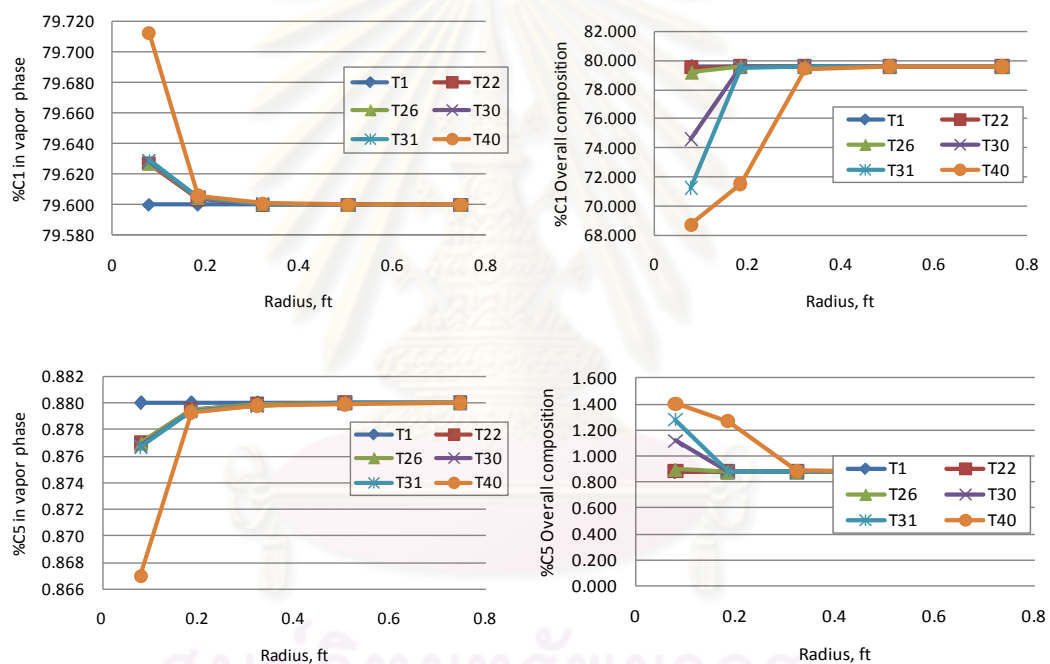


Figure 5.15: Compositions profile during drawdown period of lean Fluid A when the probe pressure is below the dew point pressure.

Figure 5.16 shows overall and vapor composition at the probe grid block versus time. For all components, the composition profiles in the vapor phase and overall composition are presented in Appendix C. In the vapor phase at the probe cell, the compositions of N_2 , CO_2 and C_1 are increasing with time and the intermediate and heavy components, C_2 up to C_{30+} , are decreasing with time. On the other hand, in the overall composition, N_2 , CO_2 and C_1 compositions are decreasing with time and the

intermediate and heavy components, C_2 up to C_{30+} , are increasing with time. Hence, the overall fluid at the probe becomes heavier and heavier while the flowing gas becomes leaner and leaner.

Figures 5.17 and 5.18 show the shifting of phase envelope during depletion. The initial reservoir pressure is 3474 psia, and the reservoir temperature is 251°F. The phase envelope of initial lean Fluid A is shown as ZI in Figure 5.17. Initially, the critical point lies to the left of the pressure path, which this is a gas condensate behavior. As can be seen, the fluid switches from lean gas condensate behavior to rich gas condensate behavior and to volatile oil behavior at 0.0128 hr or 46 sec. Since the overall composition of the mixture at the probe cell is changing during the drawdown period as shown in Figure 5.16, the associated critical properties and phase envelope are also changing.

As fluid is drawn, some intermediate and heavy components in the gas phase condense in the probe grid cell, and the overall mixture in the cell becomes richer in heavy components. The phase envelope of probe fluid is shifting during production. The critical point tends to move clockwise round the phase envelope, and the phase envelope itself tends to move to higher pressure and to higher temperature as shown in Figure 5.17. However, the critical point still lies to the left of the pressure path but the critical point becomes nearer to the pressure path line with increasing production time. Hence, the fluid behaves a richer gas condensate.

After time step T31, the probe fluid has a higher critical temperature than the reservoir temperature. The critical point lies to the right of the pressure path line as shown in Figure 5.18. The phase envelope tends to move to lower pressure and to higher temperature as the pressure is depleted. Hence, the fluid at this time, 46 sec, changes from a gas condensate system to a volatile oil system. As explained earlier, zone 1, where there is two phase flow, also develops at time step of T31 or 46 sec. It indicates that fluid behavior changes from gas condensate to volatile oil as zone 1 develops.

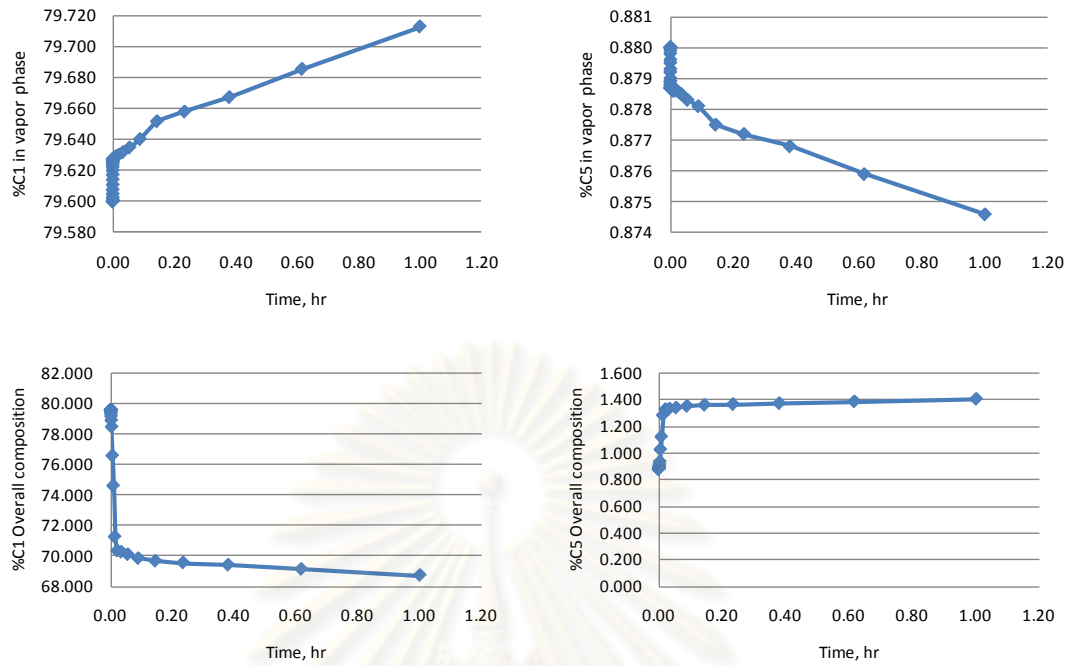


Figure 5.16: Composition at the probe cell versus time during drawdown period of lean Fluid A when the probe pressure is below the dew point pressure.

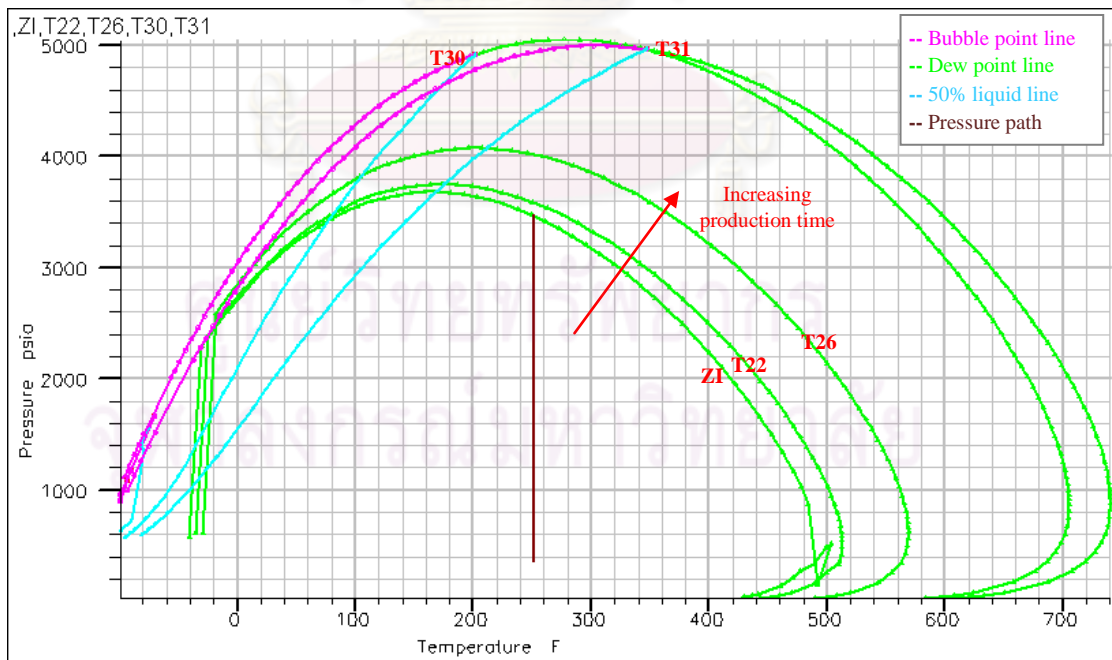


Figure 5.17: Phase behavior at the probe grid block before 46 sec (T31) of production of lean Fluid A when the probe pressure is below the dew point pressure.

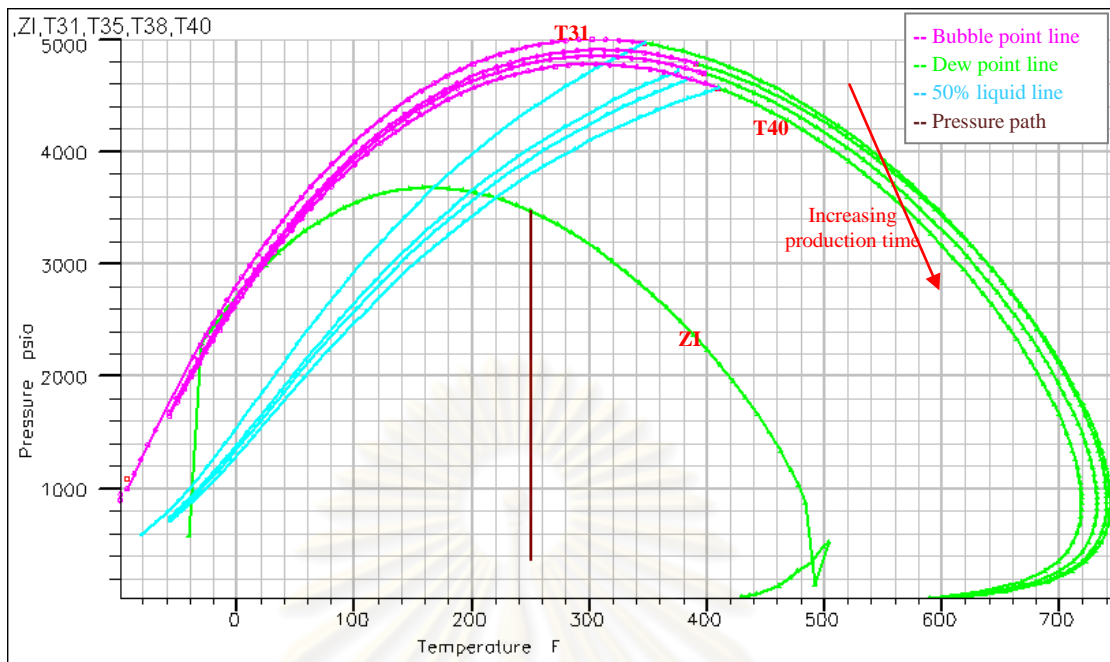


Figure 5.18: Phase behavior at the probe grid block after 46 sec (T31) of production of lean Fluid A when the probe pressure is below the dew point pressure.

5.2.2 Phase Behavior during Build-up Period

During the buildup period, the probe pressure increases to be above the dew point pressure as shown in Figure 5.8, and we would expect the oil to revaporize into gas. Figure 5.19 shows the phase envelope at the probe cell during the build-up test. Initially, the fluid at the probe cell behaves like a volatile oil at the end of previous drawdown.

At the probe grid block during build-up period, the phase envelope of the fluid changes a bit, and the critical point moves counterclockwise. This behavior implies that the fluid still behaves like a volatile oil and becomes a bit leaner during the build-up period as a result of a little change in fluid composition which can be seen in Figure 5.20. Since fluid composition is changing with the radial distance at the beginning of build-up test as can be seen in Figure 5.21, each component tries to go into the equilibrium. Hence, the composition at the probe cell changes. For example, C_1 mole fraction near the well is less than that away from the well at the beginning of build-up result in the increase of C_1 at probe cell.

Figure 5.22 shows condensate saturation of each block during the build-up test. As can be seen, condensate saturation increases as the pressure increases at the probe cell, R1, and at the cell adjacent to the probe cell, R2. This is the characteristic of volatile oil system. On the other hand, the condensate saturation at R3 decreases as the pressure increases because of revaporization. This is the characteristic of gas condensate system.

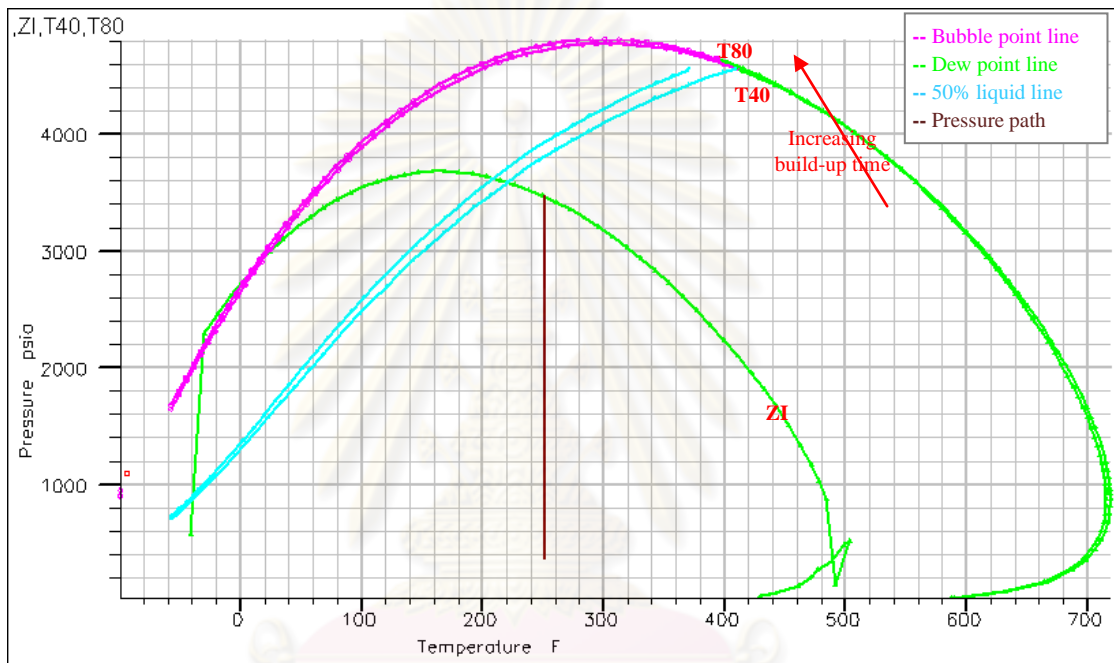


Figure 5.19: Phase behavior at the probe cell during build-up period of lean Fluid A.

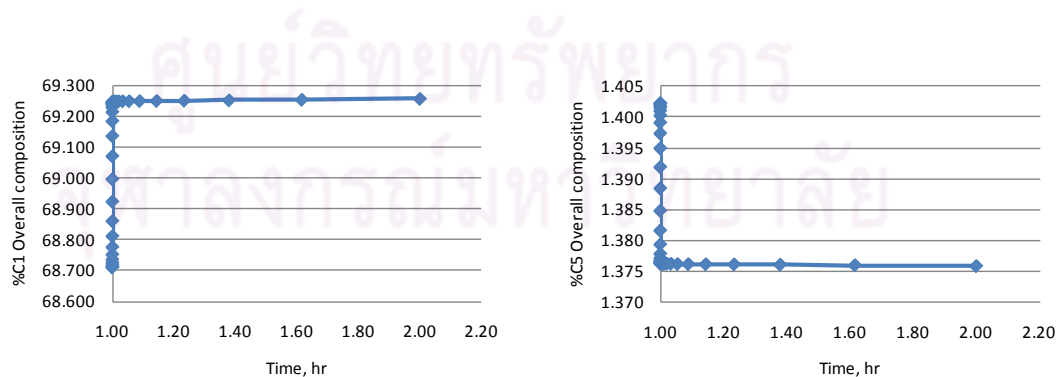


Figure 5.20: Composition at the probe cell during build-up period of lean Fluid A.

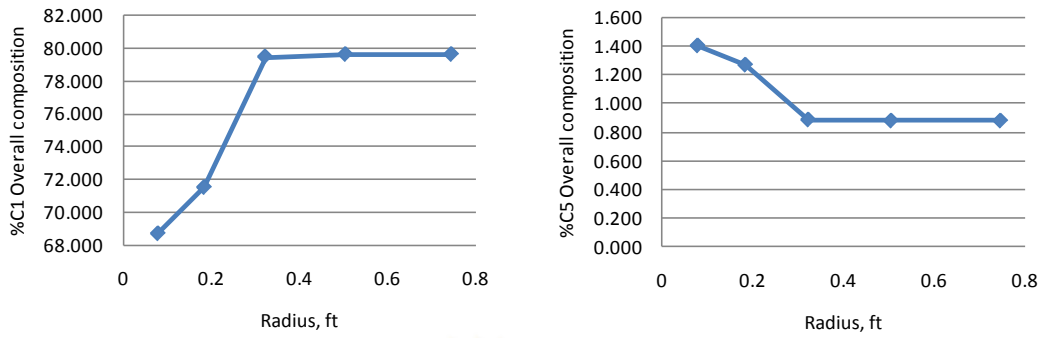


Figure 5.21: Composition profile at the beginning of build-up period of lean Fluid A.

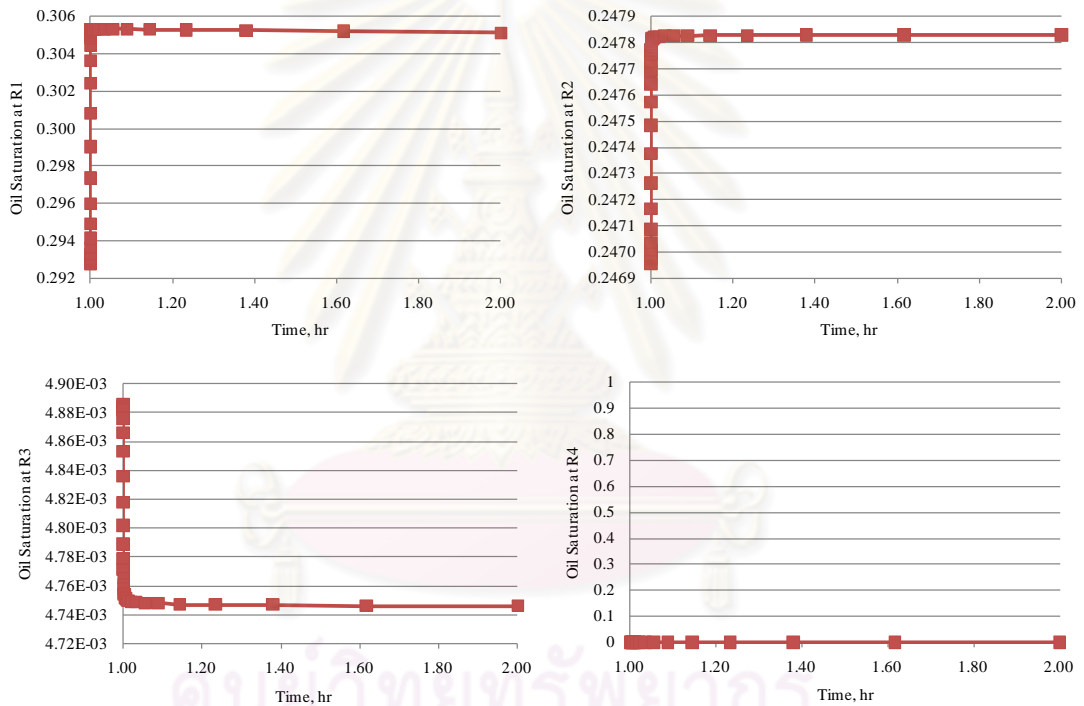


Figure 5.22: Block condensate saturation during build-up period of lean Fluid A.

5.3 Effects of Drawdown Rate

The objective of this section is to investigate the effects of drawdown rate. A schematic of reservoir description for this case is shown in Figure 5.23. The same reservoir model is used. We varied the drawdown rate as shown in Table 5.3. The flow period consists of a 60-minute drawdown and a 60-minute buildup. The radial

and theta permeabilities are still 5 mD while the vertical permeability is still 1 mD resulting permeability anisotropy ratio of 0.2, the same as the base case. The condensate saturation profiles at the end of drawdown of each case are shown in Figure 5.24.

Figure 5.24 shows condensate saturation profile at the end of drawdown for different drawdown rates obtained from reservoir simulation. The diagnostic plots of the tests are shown in Figures 5.25 to 5.27. Figure 5.28 shows phase envelopes at the end of drawdown for different drawdown rates. The analytical model used for interpretation matched well with the data on log-log diagnostic plot for all cases as shown in Appendix D.

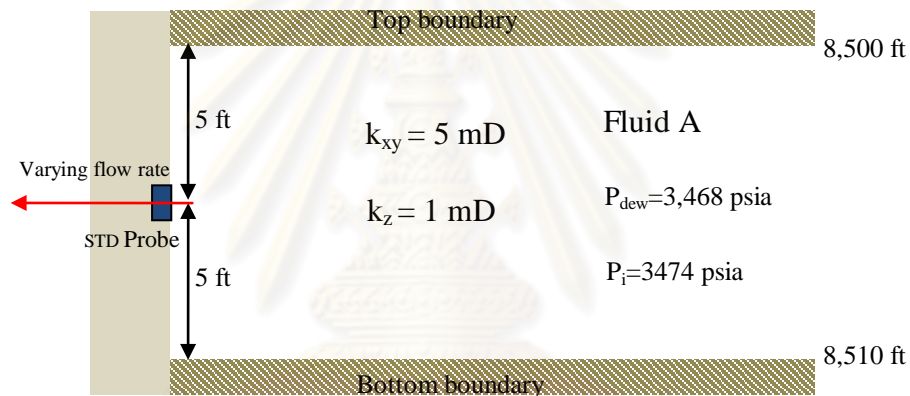


Figure 5.23: A schematic of reservoir for different drawdown rates.

Table 5.3: Case definition and pressure drop of each case.

Case	Drawdown rate (Mscf/d)	ΔP^* (psia)	ΔP^* below P_{dew} (psia)
A-r1	0.028	2.1	-3.9
A-r2	0.084	6.3	0.3
A-r3	0.168	12.9	6.9
A-r4	0.25	21.8	15.8
A-r5	0.50	66.2	60.2
A-r6	0.75	127.6	121.6
A-r7	1.00	223.8	217.8
A-r8	2.00	544.3	538.3

* pressure drop at the end of drawdown

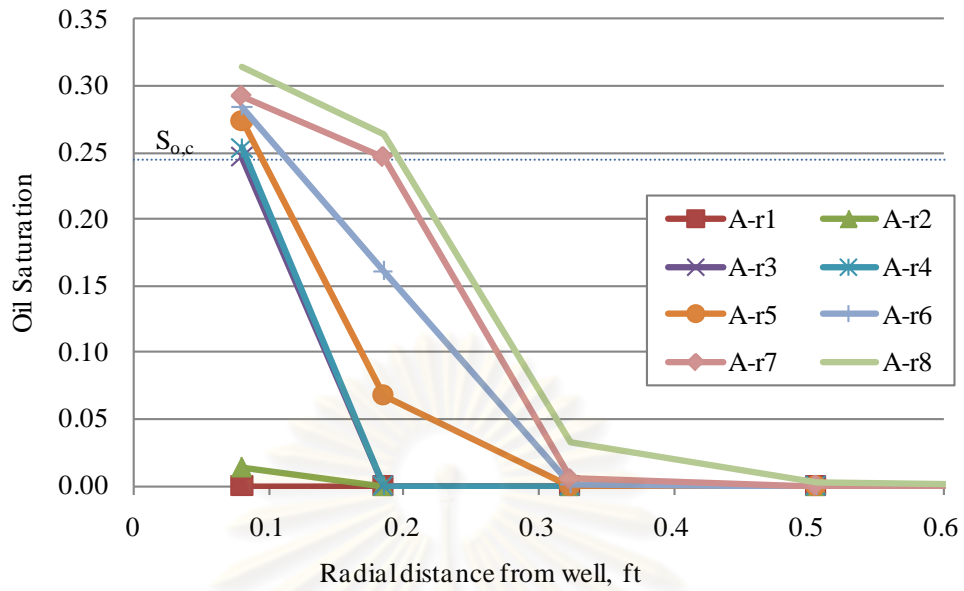


Figure 5.24: Condensate saturation profile at the end of drawdown of lean Fluid A for different drawdown rates.

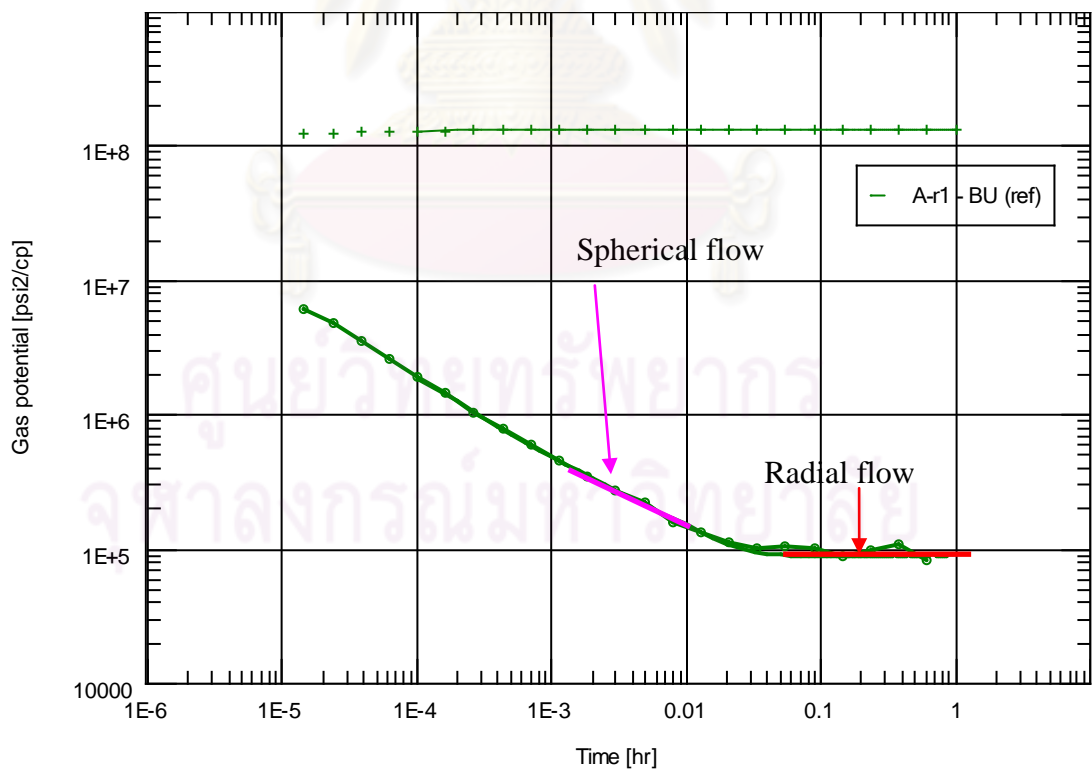


Figure 5.25: Derivative plot of lean Fluid A for case A-r1.

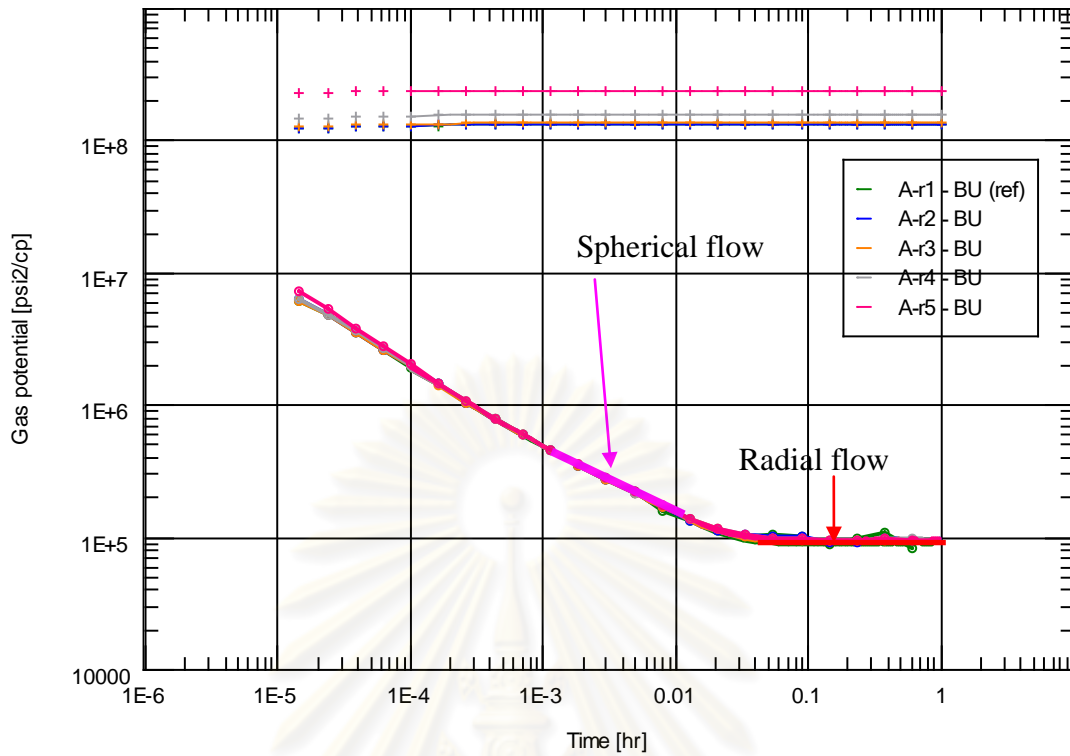


Figure 5.26: Derivative plots of lean Fluid A for case A-r2, A-r3, A-r4 and A-r5.

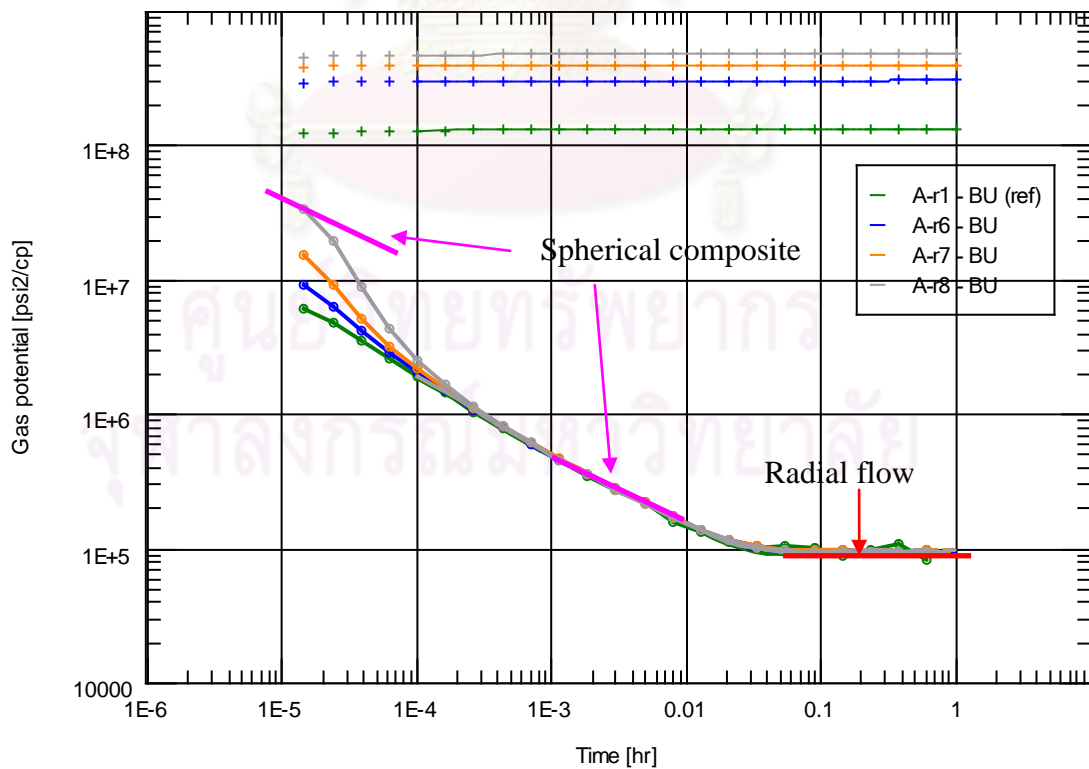


Figure 5.27: Derivative plots of lean Fluid A for case A-r6, A-r7 and A-r8.

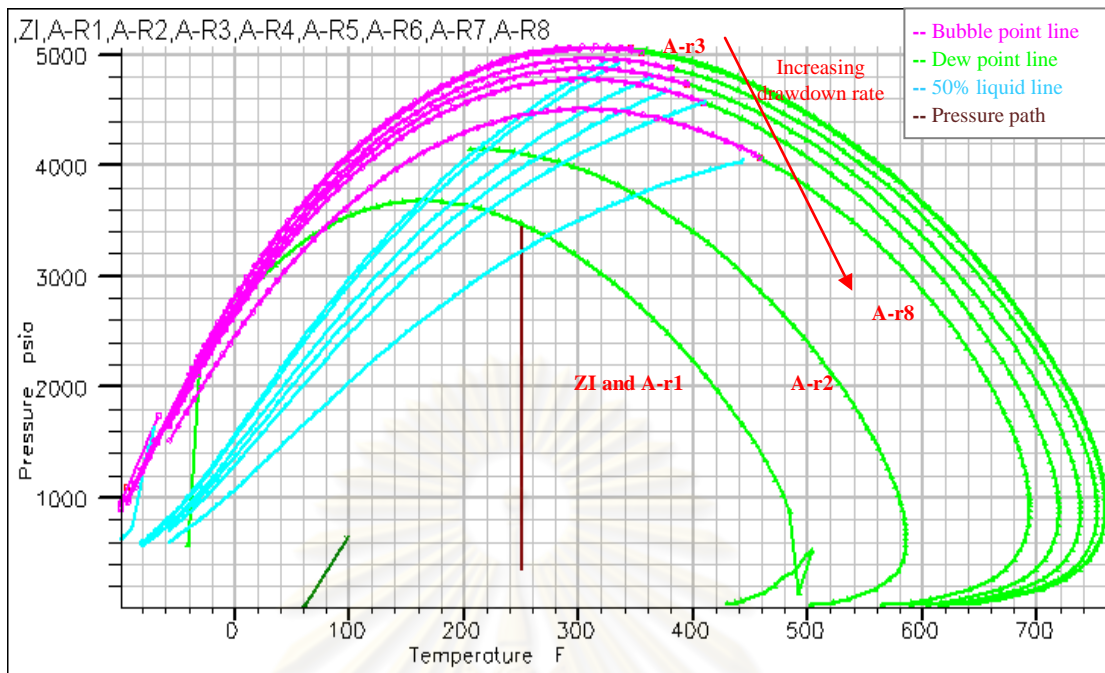


Figure 5.28: Phase behavior at the end of drawdown for different drawdown rates for Fluid A.

Table 5.4: Interpreted results for different drawdown rates.

Case	Interpreted			Error			Skin	R_{inv} (ft)	k_z/k_{xy} (early time)
	k_{xy} (mD)	k_z/k_{xy}	Calc. k_z (mD)	k_{xy} (%)	k_z/k_{xy} (%)	k_z (%)			
A-r1	2.95	0.200	0.97	-3.28	0.00	-3.2	0.00	67.1	-
A-r2	2.82	0.236	1.09	-7.54	18.00	9.1	0.01	65.4	-
A-r3	2.83	0.234	1.09	-7.21	17.00	8.5	0.02	65.5	-
A-r4	2.92	0.235	1.12	-4.26	17.50	12.4	0.13	65.7	-
A-r5	2.93	0.233	1.12	-3.93	16.50	11.9	0.52	65.7	-
A-r6	2.95	0.223	1.08	-3.28	11.50	7.8	0.76	66.0	0.069
A-r7	2.93	0.226	1.09	-3.93	13.00	8.5	1.02	65.7	0.039
A-r8	2.92	0.232	1.11	-4.26	16.00	11.1	1.20	65.7	0.011

As can be seen in Table 5.3, the flowing probe pressure in the first case, A-r1, remains above the dew point pressure for the entire test duration. The flowing probe pressure at the end of drawdown period in case A-r2, case A-r3, A-r4 and A-r5 is a little bit below the dew point pressure whereas the flowing probe pressure at the end

of drawdown period in case A-r6, A-r7 and A-r8 is below the dew point pressure. As there is no depletion in the reservoir, the pressure at the end of build-up for all cases is above the dew point pressure.

From Figure 5.24, condensate bank zone 1 develops at the end of drawdown when using gas flow rate higher than 0.168 Mscf/d. With increasing drawdown rate, the condensate bank size is increasing, both zone1 and zone2 are increasing.

For case A-r1 in Figure 5.25, the flowing probe pressure remains above the dew point pressure. There is only single phase gas in the reservoir. The derivative plot for the build-up following the drawdown of this case exhibits a negative half slope straight line and a zero slope straight lines as expected from single phase gas. Therefore, this case will be used as a reference case to compare the derivative plot with other cases.

For case A-r2, A-r3, A-r4 and A-r5 in Figure 5.26, the flowing probe pressure just drops below the dew point pressure. Thus, the oil drops out of the gas. The diagnostic plots still exhibit a behavior similar to that in case A-r1. However, the corresponding interpretation indicates a higher total skin as shown in Table 5.4. This is the effect of the condensate drop-out. In case A-r2, the condensate saturation has not yet reached the critical saturation, and only zones 2 and 3 exist in the reservoir as shown in Figure 5.24. Only the gas phase is produced, and the immobile condensate appears as an additional skin effect, known as condensate blockage. As can be seen in Figure 5.24, case A-r3, A-r4 and A-r5 have all three zones in the reservoir but they don't show clearly the first negative half slope straight line since the radius of zone 1, which represents the upper negative half slope line, is too short to be monitored by the derivative plot.

For case A-r6, A-r7 and A-r8 in Figure 5.27, the probe pressure drops below the dew point pressure. Thus, condensate occurs. The derivative plots show two negative half slope parallel straight lines indicating two different spherical mobilities, a spherical composite behavior and followed by a zero slope straight line representing radial flow. As the pressure decreases, the condensate saturation reaches the critical value. At this point, the condensate becomes mobile, and zone 1 develops. All three zones exist near the wellbore in the spherical flow regime as shown in Figure 5.27. This yields a spherical composite behavior with the upper negative half slope straight

line corresponding to the spherical mobility of condensate bank and the negative half slope lower line corresponding to the spherical mobility of the original gas.

Consequently, the upper negative half slope straight line corresponding to spherical mobility of condensate bank varies with the condensate saturation. The derivative plots show noticeable spherical composite behavior when using drawdown rate of 0.75 Mscf/d or higher, in case A-r6, A-r7 and A-r8 since drawdown pressure in these cases is high enough to develop zone 1, which has condensate saturation higher than the critical condensate saturation.

The heavy component drops out of the gas phase and accumulates near the wellbore resulting in the changing of fluid composition near wellbore region and also changing phase envelope, i.e., critical point moves clockwise, as shown in Figure 5.28. The fluid at the probe cell in case A-r1 and A-r2 still behaves like a gas condensate at the end of drawdown while fluid at the probe cell in case A-r3, A-r4, A-r5, A-r6, A-r7 and A-r8 behaves like a volatile oil system. As the drawdown rate increases, the pressure drop increases and also the condensate drop out, or the heavy component, increases. Hence, the fluid becomes richer in heavy component as the drawdown rate increases.

The interpreted results in Table 5.4 confirm again that WFT pressure response in lean gas condensate reservoir can be used to estimate reservoir permeabilities with an acceptable value even when condensate banking occurs. The error of estimated horizontal permeability (k_{xy}) is less than 7.5%, and the error of estimated vertical permeability (k_z) is smaller than 12.5%.

5.4 Effects of Initial fluid Composition

The objective of this section is to investigate the effects of initial fluid composition. The same tests were used for richer gas condensate. Fluid B is richer than Fluid A, and Fluid C is richer than Fluid B. The flow period consists of a 60-minute drawdown and a 60-minute buildup. The radial and theta permeabilities are still 5 mD while the vertical permeability is still 1 mD resulting permeability anisotropy ratio of 0.2. A schematic of reservoir description for this case is shown in Figure 5.29.

Fluid composition and fluid property are changed from Fluid A to richer gas condensate. In this section, Fluid B and C were used to simulate formation tests with seven different drawdown rates as shown in Table 5.5. Fluid B has a maximum liquid drop-out of 3.41%, reservoir temperature of 270°F, initial reservoir pressure of 5850 psia, dew point pressure of 5847 psia and critical condensate saturation of 0.246. Fluid C has a maximum liquid drop-out of 19.24%, reservoir temperature of 230°F, initial reservoir pressure of 3730 psia, dew point pressure of 3724 psia and critical condensate saturation of 0.240. Fluid compositions are presented in Chapter 4.

The condensate saturation profiles at the end of drawdown from reservoir simulation runs are shown in Figures 5.34 and 5.35. The diagnostic plots of the build-up tests are shown in Figures 5.30 to 5.33, and the interpreted results are tabulated in Tables 5.6 and 5.7. Phase envelopes calculated by PVTi are shown in Figures 5.36 and 5.37. The analytical model used for interpretation matches well with the data on the log-log diagnostic plot for all cases as shown in Appendix D, which an analytical model is shown as a green line and the pressure derivative is shown as a red line.

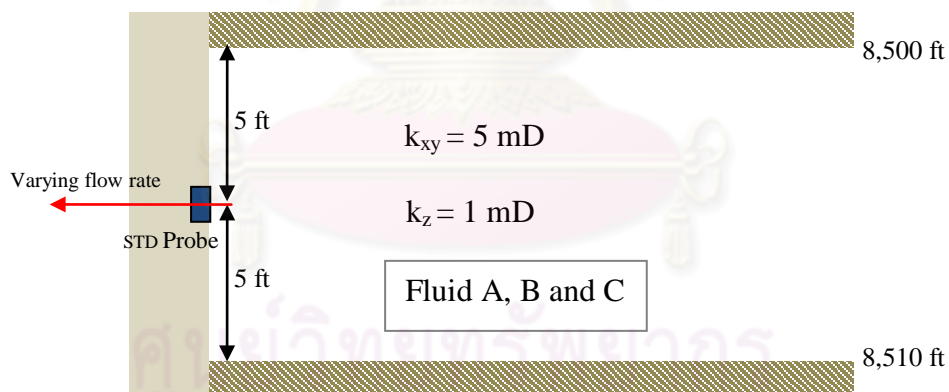


Figure 5.29: A schematic of reservoir for different initial fluid compositions.

Table 5.5: Case definition and pressure drop for Fluid B and Fluid C.

Case	Drawdown rate (Mscf/d)	ΔP^* (psia)	ΔP^* below P_{dew} (psia)	Case	Drawdown rate (Mscf/d)	ΔP^* (psia)	ΔP^* below P_{dew} (psia)
B-r1	0.028075	2.1	-0.9	C-r1	0.028075	2.8	-3.2
B-r2	0.084225	6.4	3.4	C-r2	0.084225	8.3	2.3
B-r3	0.168450	15.3	12.3	C-r3	0.168450	26.7	20.7
B-r4	0.25	29.7	26.7	C-r4	0.25	102.3	96.3
B-r5	0.50	91.9	88.9	C-r5	0.50	280.5	274.5
B-r6	0.75	187.0	184.0	C-r6	0.75	473.6	467.6
B-r7	1.00	288.8	285.8	C-r7	1.00	651.1	645.1

* pressure drop at the end of drawdown

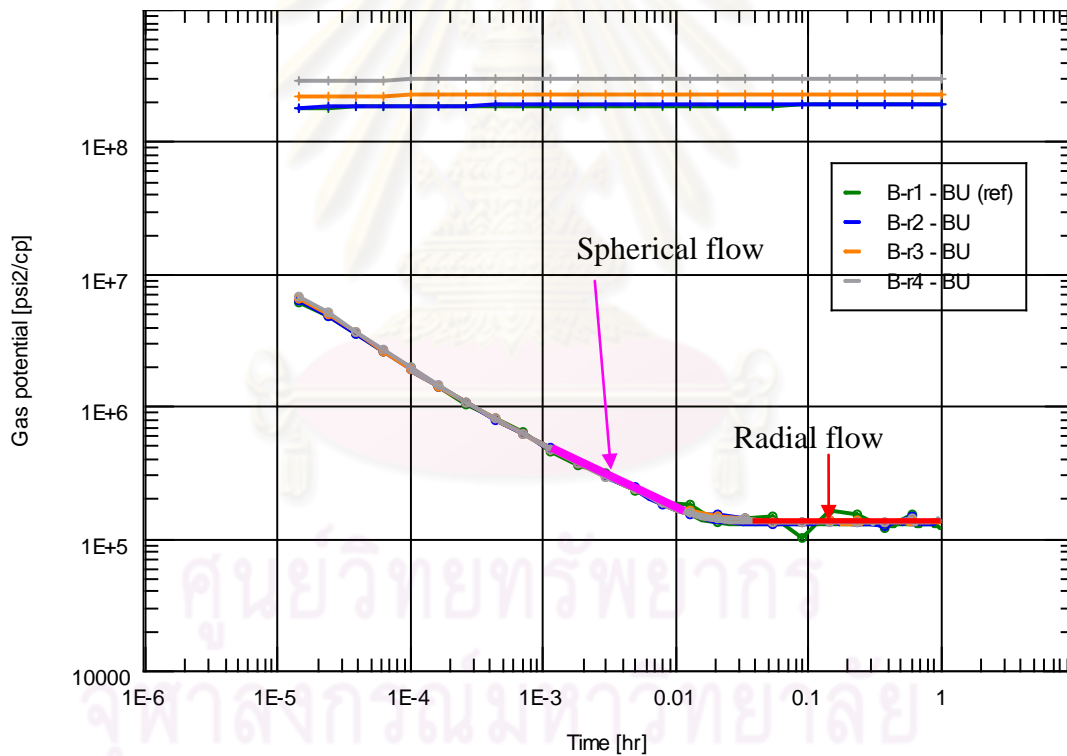


Figure 5.30: Derivative plots for case B-r1, B-r2, B-r3 and B-r4.

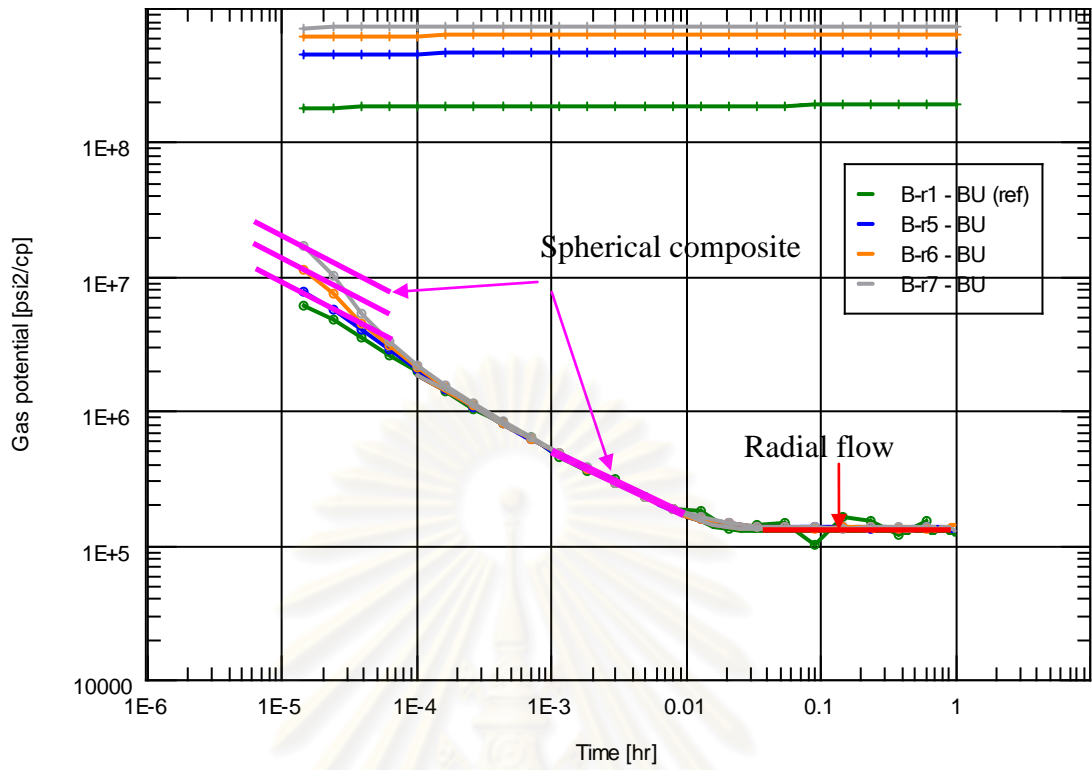


Figure 5.31: Derivative plots for case B-r5, B-r6 and B-r7,

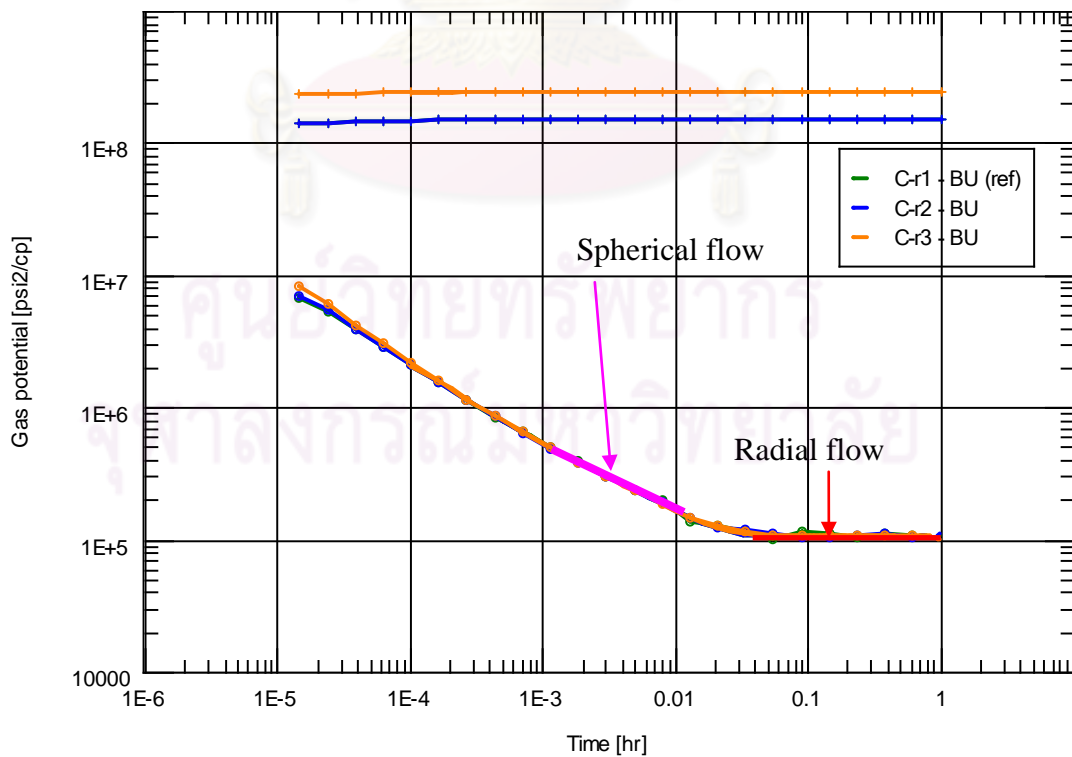


Figure 5.32: Derivative plots for case C-r1, C-r2 and B-r3.

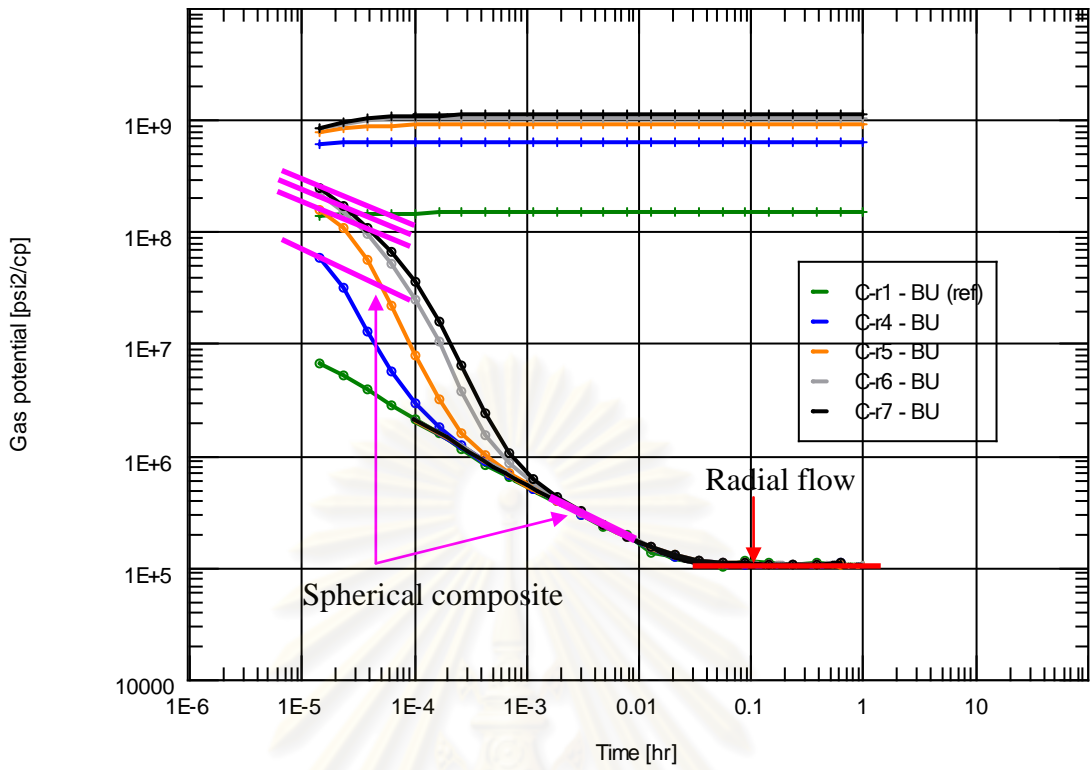


Figure 5.33: Derivative plots for case C-r4, C-r5, C-r6 and C-r7.

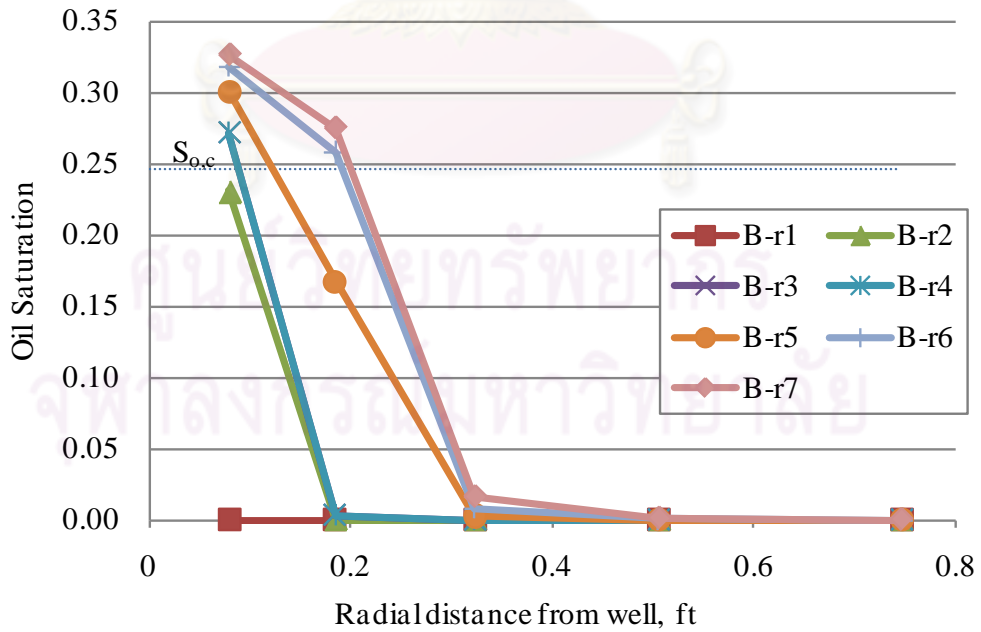


Figure 5.34: Condensate saturation profile at the end of drawdown for different drawdown rates for Fluid B.

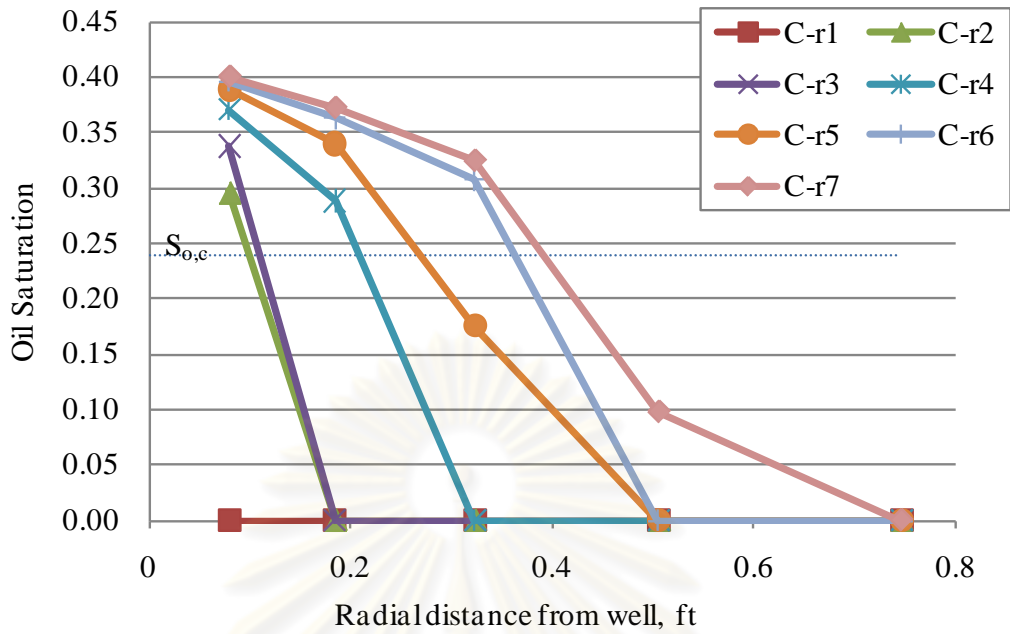


Figure 5.35: Condensate saturation profile at the end of drawdown for different drawdown rates for Fluid C.

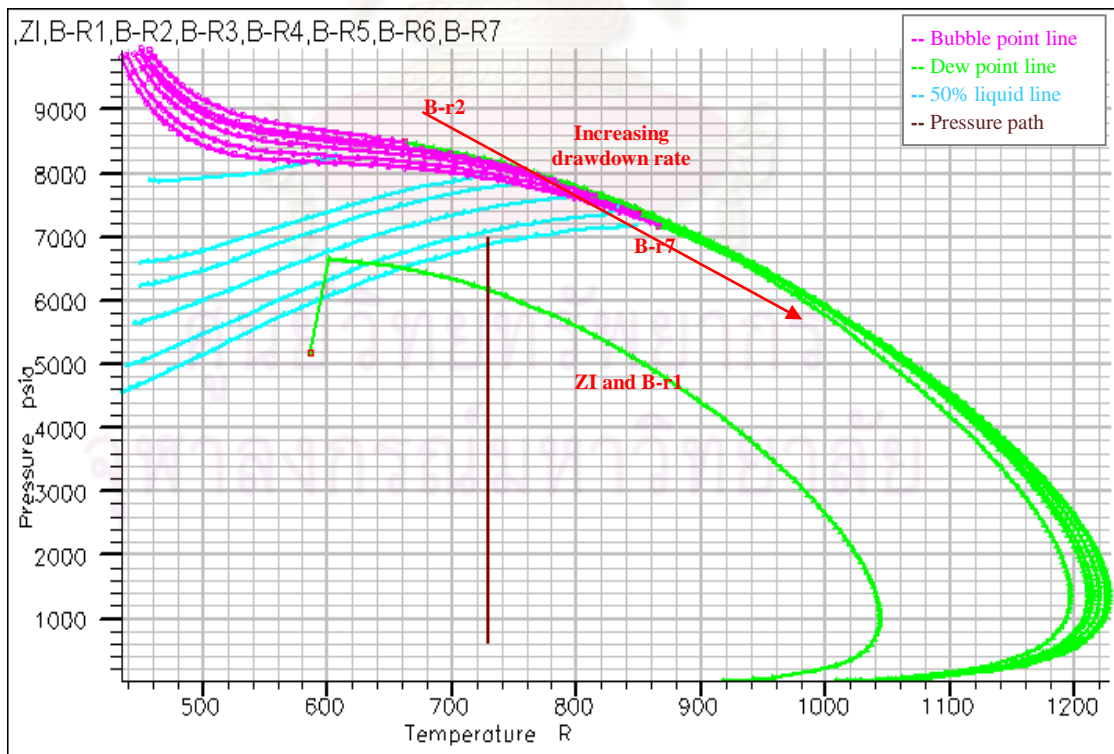


Figure 5.36: Phase behavior at the end of drawdown using Fluid B.

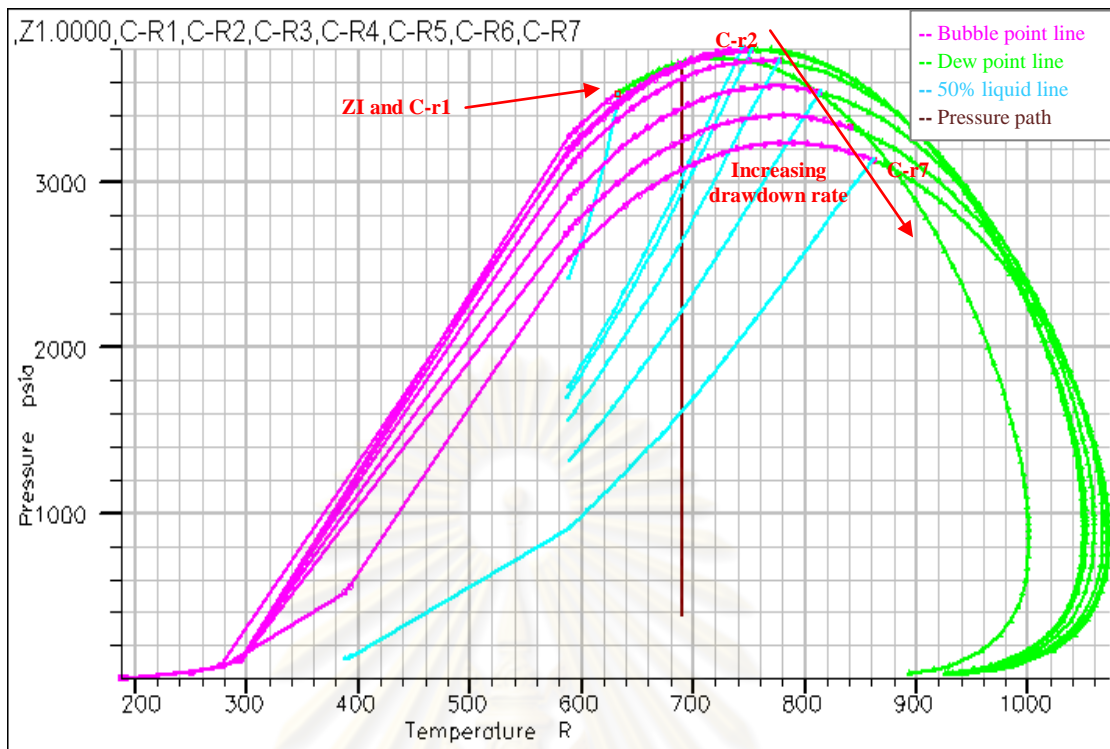


Figure 5.37: Phase behavior at the end of drawdown using Fluid C.

Table 5.6: Interpreted results for different drawdown rates using Fluid B.

Case	Interpreted			Error			Skin	R_{inv} (ft)	k_z/k_{xy} (early time)
	k_{xy} (mD)	k_z/k_{xy}	Calc. k_z (mD)	k_{xy} (%)	k_z/k_{xy} (%)	k_z (%)			
B-r1	3.01	0.206	1.02	-1.31	3.00	1.6	0.00	87.5	-
B-r2	2.94	0.222	1.07	-3.61	11.00	7.0	0.00	86.6	-
B-r3	2.91	0.228	1.09	-4.59	14.00	8.8	0.17	86.0	-
B-r4	2.90	0.228	1.08	-4.92	14.00	8.4	0.43	85.9	-
B-r5	2.82	0.254	1.17	-7.54	27.00	17.4	0.84	84.8	0.09875
B-r6	2.88	0.235	1.11	-5.57	17.50	11.0	1.14	85.6	0.06387
B-r7	2.88	0.233	1.10	-5.57	16.50	10.0	1.28	85.6	0.03956

Table 5.7: Interpreted results for different drawdown rates using Fluid C.

Case	Interpreted			Error			Skin	R_{inv} (ft)	k_z/k_{xy} (early time)
	k_{xy} (mD)	k_z/k_{xy}	Calc. k_z (mD)	k_{xy} (%)	k_z/k_{xy} (%)	k_z (%)			
C-r1	2.92	0.254	1.22	-4.26	27.00	21.6	0.01	64.0	-
C-r2	2.94	0.25	1.20	-3.61	25.00	20.5	0.02	64.2	-
C-r3	2.89	0.268	1.27	-5.25	34.00	27.0	0.45	63.6	0.0997
C-r4	2.95	0.241	1.17	-3.28	20.50	16.5	1.40	64.3	0.0056
C-r5	2.90	0.253	1.20	-4.92	26.50	20.3	1.73	63.7	0.00046
C-r6	2.86	0.249	1.17	-6.23	24.50	16.7	1.86	63.4	0.00019
C-r7	2.91	0.245	1.17	-4.59	22.50	16.9	1.93	63.8	0.00019

As can be seen in Table 5.5, the flowing probe pressure in case B-r1 and case C-r1 remains above the dew point pressure for the entire test duration. The flowing probe pressure in the other cases is below the dew point pressure. As there is no depletion in the reservoir, the pressure at the end of build-up for all cases is above the dew point pressure.

From Figures 5.30 to 5.33, the richer gas condensate Fluid B and C exhibit similar derivative behavior to that of the leaner Fluid A, i.e., a spherical composite behavior and radial flow behavior are observed from the derivative plot when three radial zones developed in the reservoir. As can be seen in Section 5.3, Fluid A exhibits the spherical composite behavior at drawdown rate of 0.75 Mscf/d and higher. From Figures 5.31 and 5.33, Fluid B exhibits the spherical composite behavior at drawdown rate of 0.5 Mscf/d and higher whereas Fluid C exhibits the same behavior at rate of 0.168 Mscf/d and higher. Fluid B is richer than Fluid A, and Fluid C is richer than Fluid B. The richer gas condensates have more amount of condensate drop-out for the same pressure drop. This is why the richer fluids exhibit the spherical composite behavior at a lower rate.

Figures 5.34 and 5.35 show condensate saturation profile at the end of drawdown for different drawdown rates for Fluid B and C, respectively. For Fluid B, condensate bank zone 1 develops at the end of drawdown when using gas flow rate higher than 0.168 Mscf/d (case B-r3). With increasing drawdown rate, the condensate bank size is increasing (both zone 1 and zone 2). For Fluid C, when using gas flow rate higher than only 0.084 Mscf/d (case C-r2), condensate bank zone 1 can develop at the

end of drawdown. Similar to Fluid A and B, condensate bank size is increasing (both zone 1 and zone 2) with increasing drawdown rate. This clearly shows that the condensate increases in size as the drawdown rate increases.

Phase envelopes in Figures 5.36 and 5.37 clearly show that the shifting of phase envelope in richer gas condensate is similar to that occurs in lean gas condensate, i.e., critical point moves clockwise, and fluid behavior changes from lean gas condensate behavior to rich gas condensate behavior and to volatile oil behavior as the drawdown rate increases. The heavy component drops out of the gas phase and accumulates near the wellbore resulting in the changing of fluid composition near wellbore region. As the drawdown rate increases, the pressure drop increases and also the condensate drop out, or the heavy component, increases. The richer gas condensates have more amount of condensate drop-out for the same pressure drop. This is why the richer fluids change the behavior from gas condensate behavior to volatile oil behavior at a lower rate.

The interpreted results in Tables 5.6 and 5.7 show that WFT pressure response in rich gas condensate reservoir can be used to estimate reservoir permeabilities with an acceptable value even when condensate banking occurs. The error of estimated horizontal permeability (k_{xy}) is less than 7.5%, and the error of estimated vertical permeability (k_z) is no larger than 27%. The upper negative half slope straight line corresponding to spherical mobility of condensate bank varies with the condensate saturation. The reduction in condensate spherical mobility is higher than the lean gas condensate case because of higher condensate blockage.

5.5 Effects of Test Duration

The objective of this section is to study the effect of test duration by varying drawdown period and build-up period. Tests with five different durations of buildup and drawdown periods as shown in Table 5.8 were simulated. The horizontal permeability (k_{xy}) was set equal to 5 mD, and the vertical permeability (k_z) was set equal to 1 mD. Thus, the permeability anisotropy is 0.2 mD. The flow rate of the tests was set at 2Mscf/d to draw Fluid A. The probe position was set at the middle of the reservoir as shown in Figure 5.38.

After formation tests were simulated, the pressure responses for these different cases were interpreted using Saphir. The analytical model used for interpretation matched well with the data on log-log diagnostic plot for all cases as shown in Figures D23 to D27 in Appendix D, which an analytical model is shown as a green line and the pressure derivative is shown as a red line.

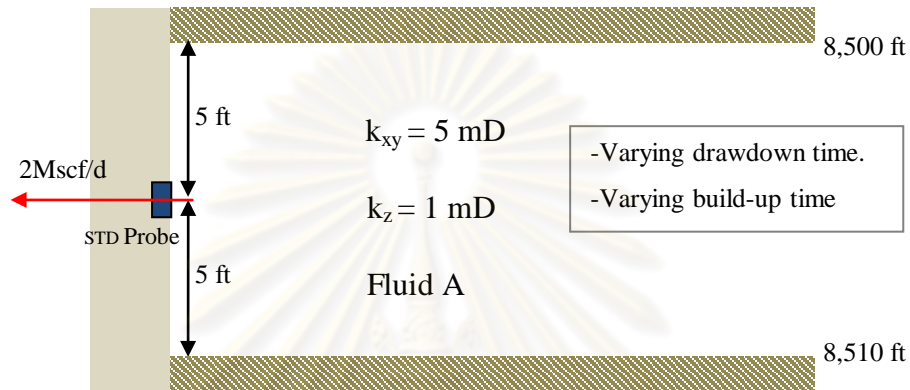


Figure 5.38: Schematic of a single layer reservoir with different test durations.

Table 5.8: Case definition for different test durations.

Case	Drawdown rate (Mscf/d)	Drawdown time (mins)	Build-up time (mins)	ΔP^* (psia)	ΔP^* below P_{dew} (psia)
A-t1	2.00	15.0	30.0	467.7	461.7
A-t2	2.00	15.0	60.0	467.7	461.7
A-t3	2.00	30.0	30.0	522.7	516.7
A-t4	2.00	30.0	60.0	522.7	516.7
A-t5	2.00	60.0	60.0	544.3	538.3

* pressure drop at the end of drawdown

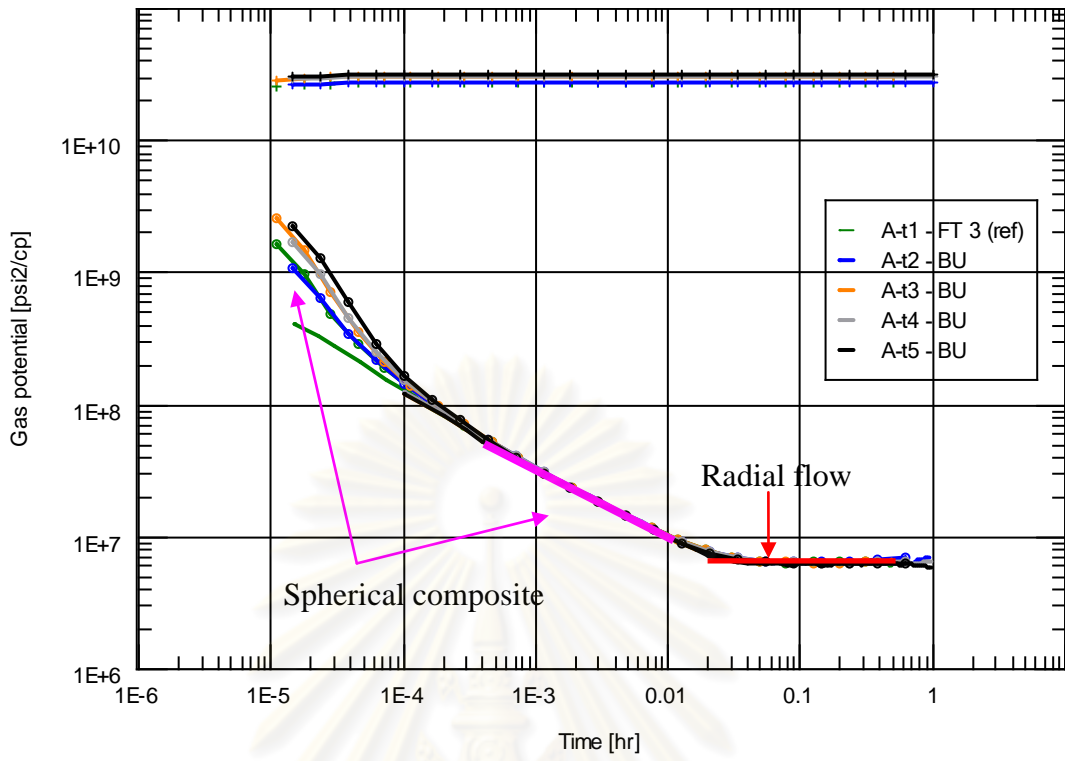
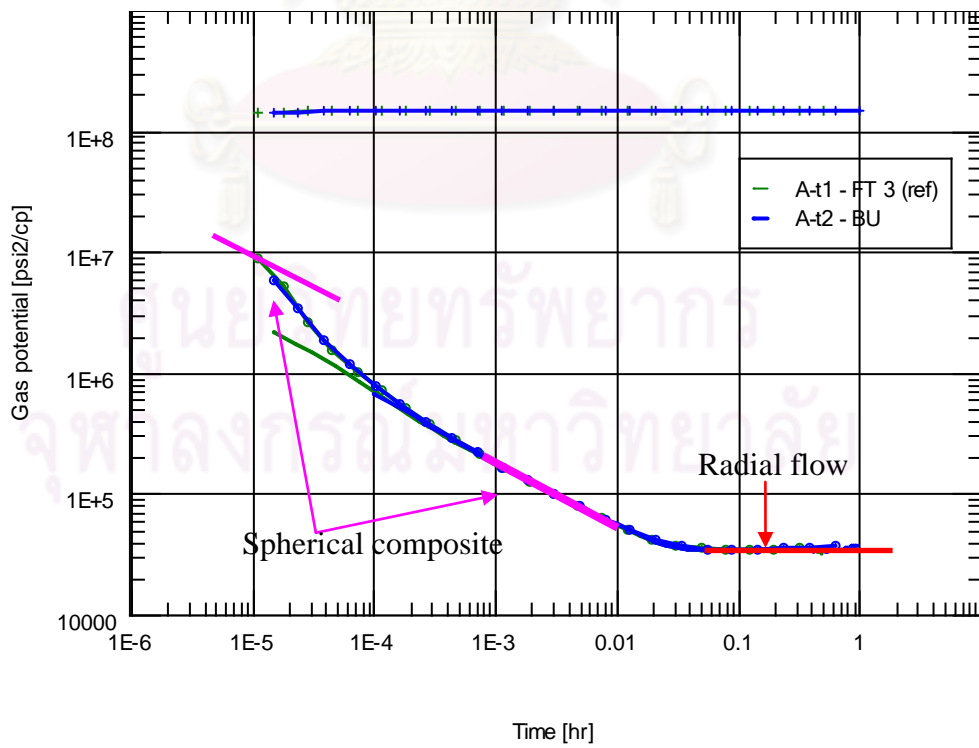
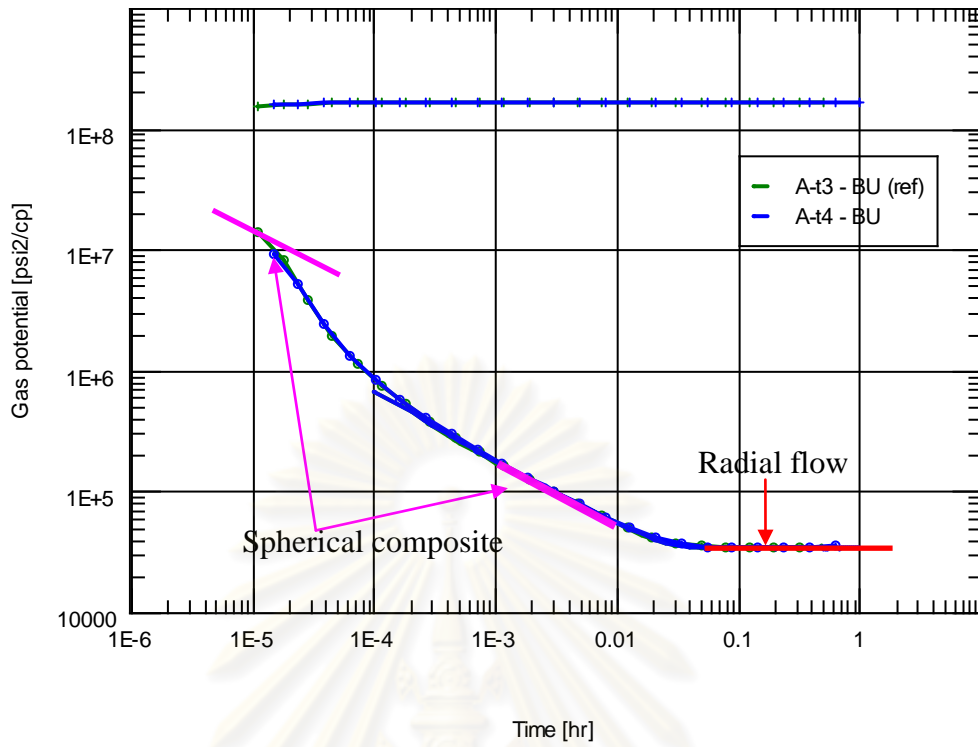


Figure 5.39: Derivative plot for different test durations.



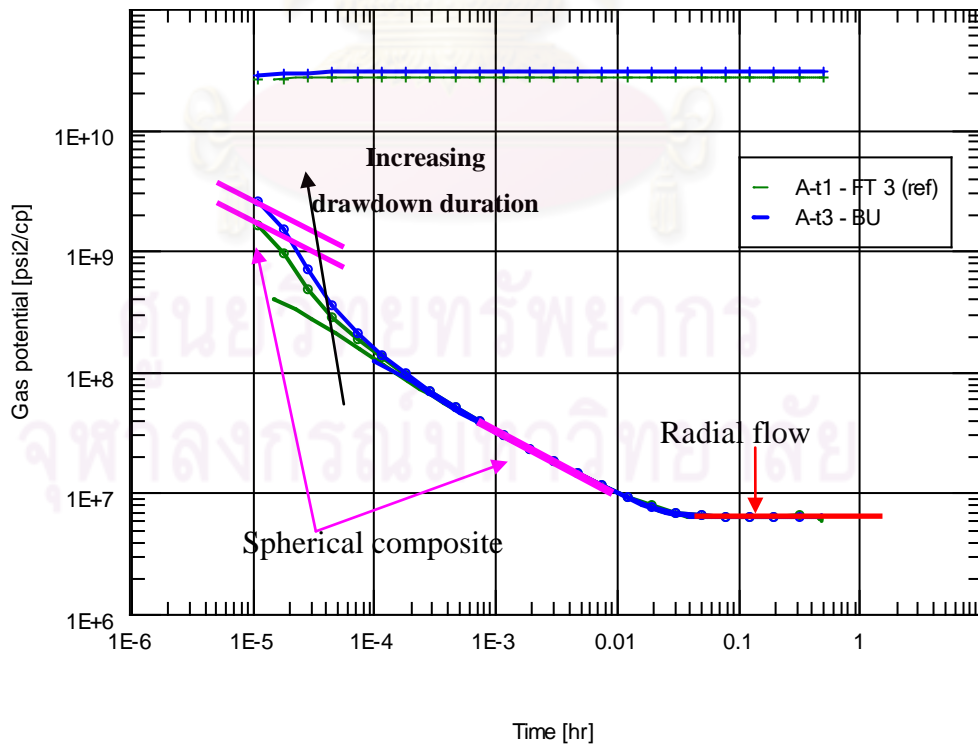
(a): Derivative plot of case A-t1 and case A-t2.

Figure 5.40: Derivative plot for different build-up duration.



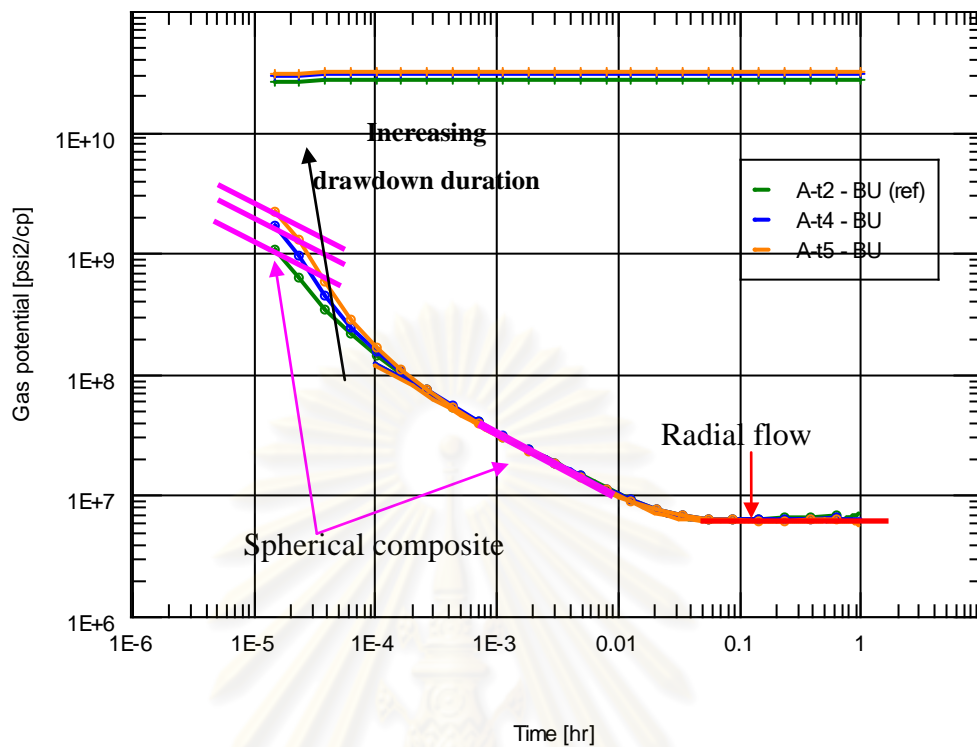
(b): Derivative plot of case A-t3 and case A-t4.

Figure 5.40: Derivative plot for different build-up duration (continued).



(a): Derivative plot of case A-t1 and case A-t3.

Figure 5.41: Derivative plot for different drawdown duration.



(b): Derivative plot of case A-t2, case A-t4 and case A-t5.

Figure 5.41: Derivative plot for different drawdown duration (continued).

Since the simulation was performed for Fluid A with drawdown rate of 2 Mscf/d, the spherical composite behavior should be seen in the derivative plots. As expected, diagnostic plots of all cases show spherical composite behavior. However, the prominent of the upper negative half slope line of each case is different as shown in Figure 5.39.

Figure 5.40 shows derivative plots of case A-t1 in comparison with case A-t2 and derivative plots of case A-t3 in comparison with case A-t4 in which the build-up time is increases while keeping the same drawdown duration. The derivatives exhibit the same behavior for the same drawdown duration. This is a result of the same pressure drop and the same condensate saturation profile at the end of drawdown as shown in Table 5.9. However, radius of investigation is longer as we increase the build-up time, as shown in Table 5.10 since the results are interpreted from the derivative plot of the build-up period.

From Figure 5.41, derivative plots show that the upper negative half slope straight line can be seen clearer as we increase the drawdown time while keeping the

same build-up time. This is a result of the difference in condensate saturation profile at the end of drawdown as shown in Table 5.9, as can be seen by comparing case A-t1 with case A-t3 and comparing case A-t2 with case A-t4 and case A-t5. As expected, radius of investigation is approximately the same due to the same build-up time as shown in Table 5.10.

The interpreted results in Table 5.10 show that the spherical and horizontal permeabilities obtained from the tests are close to those used in simulation with an acceptable value. The error of estimated horizontal permeability (k_{xy}) is less than 6%, and the error of estimated vertical permeability (k_z) is no larger than 13%.

Table 5.9: Block condensate saturation for different test durations.

Case	Drawdown time (mins)	Build-up time (mins)	Block condensate saturation				
			R1	R2	R3	R4	R5
A-t1	15.0	30.0	0.3097	0.24939	0.00657	0.0005	0
A-t2	15.0	60.0	0.3097	0.24939	0.00657	0.0005	0
A-t3	30.0	30.0	0.3133	0.25829	0.01417	0.0010	0
A-t4	30.0	60.0	0.3133	0.25829	0.01417	0.0010	0
A-t5	60.0	60.0	0.3147	0.26396	0.03250	0.0020	0

Table 5.10: Interpreted results for different test durations.

Case	Interpreted			Error			Skin	R_{inv} (ft)	k_z/k_{xy} (early time)
	k_{xy} (mD)	k_z/k_{xy}	Calc. k_z (mD)	k_{xy} (%)	k_z/k_{xy} (%)	k_z (%)			
A-t1	2.88	0.235	1.11	-5.57	17.50	11.0	1.05	47.4	0.02308
A-t2	2.90	0.221	1.05	-4.92	10.50	5.1	1.04	67.2	0.03539
A-t3	2.88	0.239	1.13	-5.57	19.50	12.8	1.15	47.3	0.01051
A-t4	2.91	0.217	1.04	-4.59	8.50	3.5	1.15	67.3	0.01743
A-t5	2.98	0.217	1.06	-2.30	8.50	6.0	1.20	68.1	0.02097

5.6 Effects of Probe Size

The objective of this section is to study the effects of probe size on pressure behavior in gas condensate reservoir by varying the probe size. Three different probe sizes were considered to simulate formation test: 0.15, 0.85, and 2.16 square inches representing cross sectional area of standard, large, and extra-large probe, respectively. Three different cases were defined and simulated as shown in Table 5.11. The schematic of reservoir description is shown in Figure 5.42. The radial and theta permeabilities are 5 mD and the vertical permeability is 1 mD. The flow rate of the tests was set to be 1 Mscf/d to draw Fluid A. The flow period consists of a 60-minute drawdown and a 60-minute buildup. The grid model used has to change from case to case. Hence, the theta and vertical grid sizes, which represent the probe area, were changed as shown in Appendix A.

After running the simulation for the test, the pressure response was then interpreted by Saphir. The diagnostic plots of the tests are shown in Figure 5.43, and the interpreted results are depicted in Table 5.12. The analytical model used for interpretation matched well with the data on log-log diagnostic plot for all cases as shown in Figures D28 to D30 in Appendix D, which an analytical model is shown as a green line and the pressure derivative is shown as a red line.

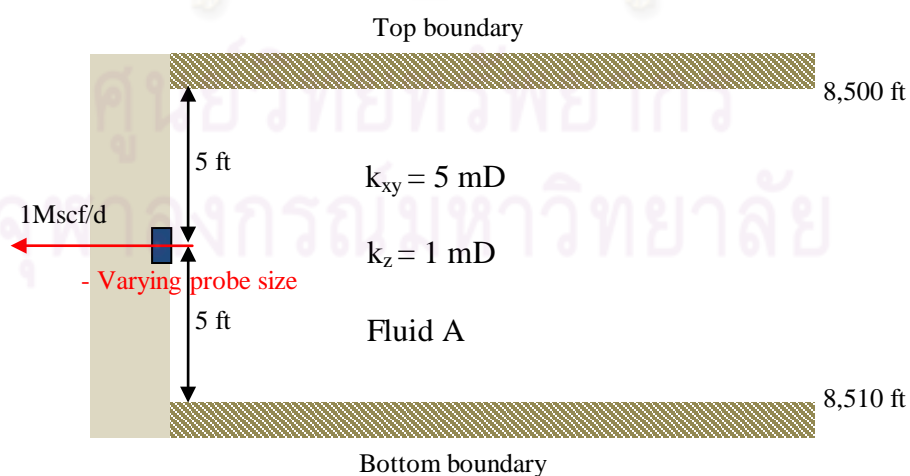


Figure 5.42: Schematic of a single layer reservoir with different probe sizes.

Table 5.11: Case definition for different probe sizes.

Case	Probe size (in ²)	Drawdown rate (Mscf/d)	ΔP^* (psia)	ΔP^* below P_{dew} (psia)
A-STD	0.1521	1.00	223.8	217.8
A-L	0.8495	1.00	71.1	65.1
A-XL	2.0110	1.00	35.2	29.2

* pressure drop at the end of drawdown

Table 5.12: Interpreted results for different probe sizes.

Case	Interpreted			Error			Skin	R_{inv} (ft)	k_z/k_{xy} (early time)
	k_{xy} (mD)	k_z/k_{xy}	Calc. k_z (mD)	k_{xy} (%)	k_z/k_{xy} (%)	k_z (%)			
A-STD	2.93	0.226	1.09	-3.9	13.00	8.6	1.02	65.7	0.0394
A-L	2.93	0.232	1.11	-3.9	16.00	11.4	0.80	65.8	0.0499
A-XL	2.91	0.232	1.11	-4.5	16.00	10.7	0.57	65.5	0.0690

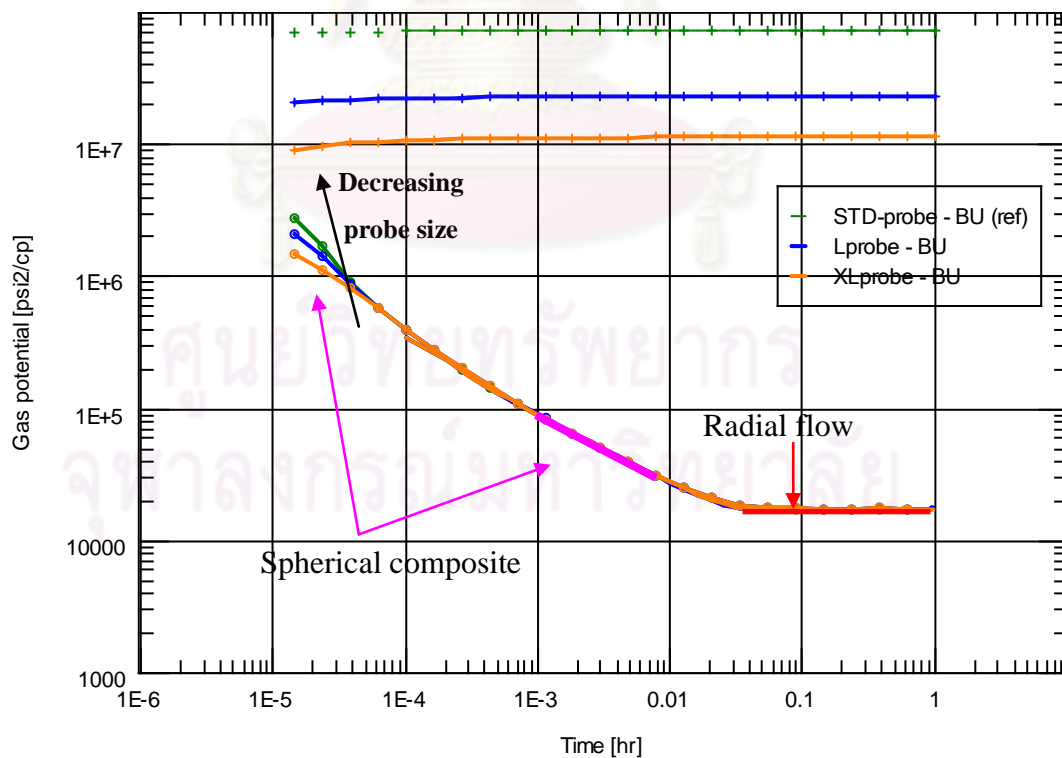


Figure 5.43: Derivative plot for different probe sizes.

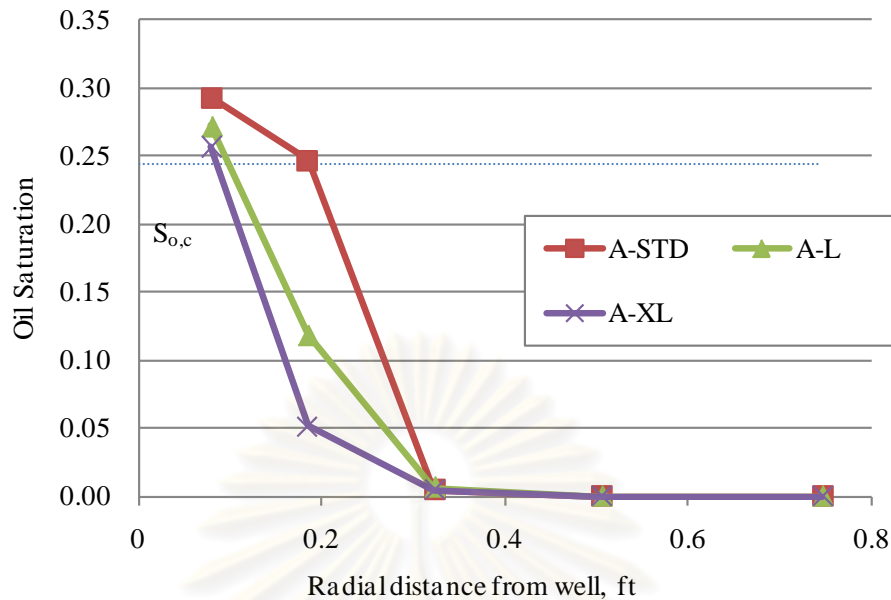


Figure 5.44: Condensate saturation profile at the end of drawdown for different probe sizes.

From Table 5.11, the standard probe size, case A-STD, has the highest pressure drop, and the extra-large probe size, case A-XL, has the lowest pressure drop. Hence, the pressure drop is decreased as probe area is increased. The spherical flow model can be matched with the data at time between 0.001 hr to 0.01 hr. At late times, after 0.05 hr, the radial flow model can be matched to the data.

The log-log derivative plots of all tests are compared in Figure 5.43. The arrow in the plot shows the direction for increase in probe area. It indicates that spherical composite behavior can be seen clearly in the standard probe and the large probe. The upper negative half slope straight line for smaller probe can be seen more clearly since smaller flow area has higher pressure drop due to partial penetration, creating a higher skin as shown in Table 5.12, and higher condensate saturation as shown in Figure 5.44.

The interpreted results in Table 5.12 show that the spherical and horizontal permeabilities obtained from the tests are close to those used in simulation with an acceptable value. The error of estimated horizontal permeability (k_{xy}) is less than 4%, and the error of estimated vertical permeability (k_z) is no larger than 12%.

5.7 Effects of Probe Position

To understand the effect of the probe position on the pressure behavior and condensate saturation, we ran a total of eleven cases at different probe positions. The probe position was set at the middle of the formation, 0.5, 1, 2, 3 and 4 feet away from the middle of the formation.

In these cases, grid sizes in the theta and radial directions are the same as those in the base case. The z-direction grids were resized corresponding to the probe position. The standard probe size was used for all cases. The initial z grid size which represents the probe area is the same. The example of resized grid is shown in Appendix A. The schematic of reservoir description is shown in Figure 5.45. The radial and theta permeabilities are 5 mD, and the vertical permeability is 1 mD. The flow rate of the tests was set to be 1Mscf/d to draw Fluid A. The flow period consists of a 60-minute drawdown and a 60-minute buildup. After running simulation, the pressure response was then interpreted by Saphir. The diagnostic plots of the tests are shown in Figure 5.46, and the interpreted results are summarized in Table 5.13. The analytical model used for interpretation matched well with the data on log-log diagnostic plot for all cases as shown in Figures D31 to D40 in Appendix D, which an analytical model is shown as a green line and the pressure derivative is shown as a red line.

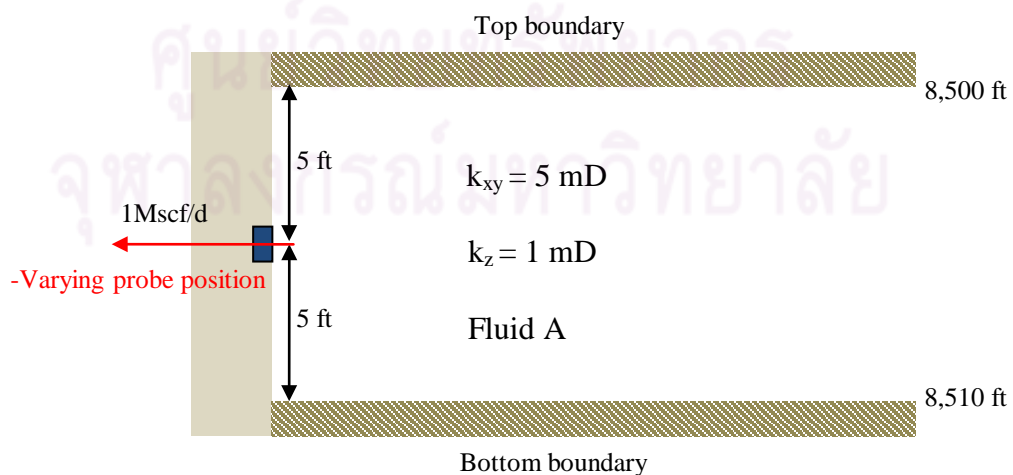


Figure 5.45: Schematic of a single layer reservoir with different probe positions.

Table 5.13: Interpreted results for different probe positions.

Case	ΔP (psia)	Interpreted			Error			Skin	R_{inv} (ft)	k_z/k_{xy} (early time)
		k_{xy} (mD)	k_z/k_{xy}	Calc. k_z (mD)	k_{xy} (%)	k_z/k_{xy} (%)	k_z (%)			
Above4ft	223.6	2.88	0.226	1.07	-5.6	13.00	6.7	1.01	65.2	0.041
Above3ft	223.6	2.88	0.235	1.11	-5.6	17.50	11	0.99	65.2	0.041
Above2ft	223.6	2.90	0.230	1.09	-4.9	15.00	9.3	1.00	65.4	0.040
Above1ft	223.7	2.93	0.226	1.09	-3.9	13.00	8.6	1.02	65.8	0.039
Above0.5ft	223.7	2.87	0.244	1.15	-5.9	22.00	14	1.02	65.1	0.041
Middle	223.8	2.93	0.226	1.09	-3.9	13.00	8.6	1.02	65.7	0.039
Below0.5ft	223.8	2.90	0.240	1.14	-4.9	20.00	14	1.03	65.4	0.040
Below1ft	223.9	2.91	0.237	1.13	-4.6	18.50	13	1.02	65.6	0.040
Below2ft	224.0	2.86	0.245	1.15	-6.2	22.50	14	1.04	65.0	0.042
Below3ft	224.0	2.90	0.229	1.09	-4.9	14.50	8.9	1.02	65.4	0.040
Below4ft	224.1	2.90	0.217	1.03	-4.9	8.50	3.2	1.00	65.4	0.040

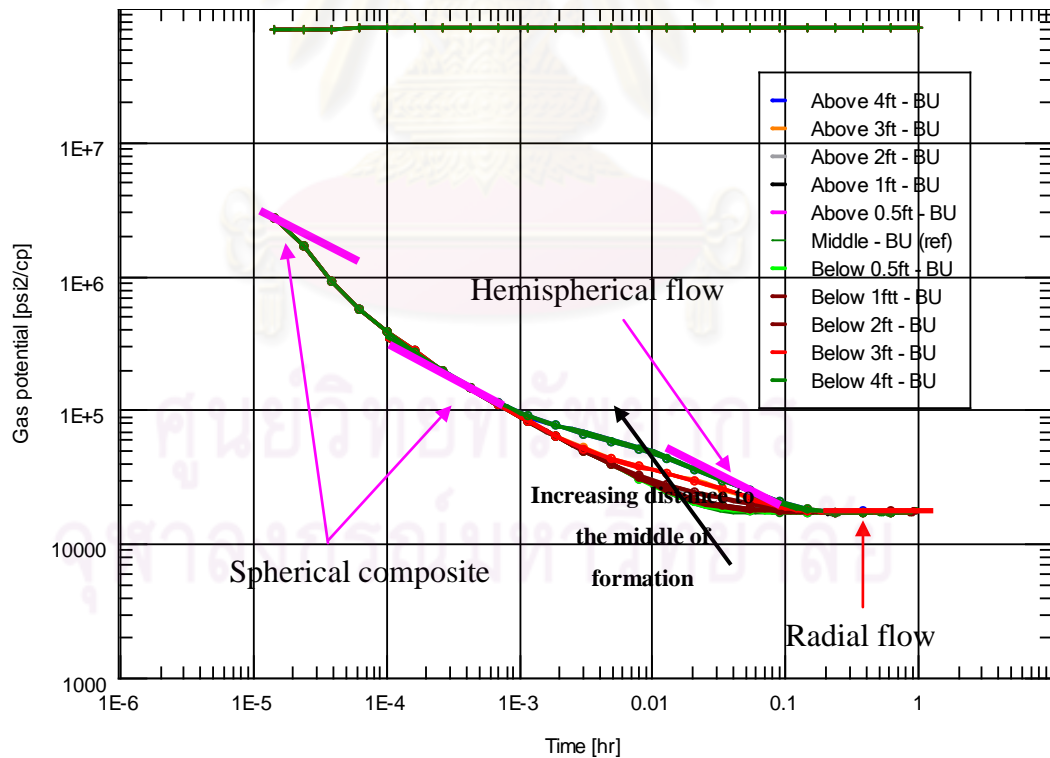


Figure 5.46: Derivative plot for different probe positions.

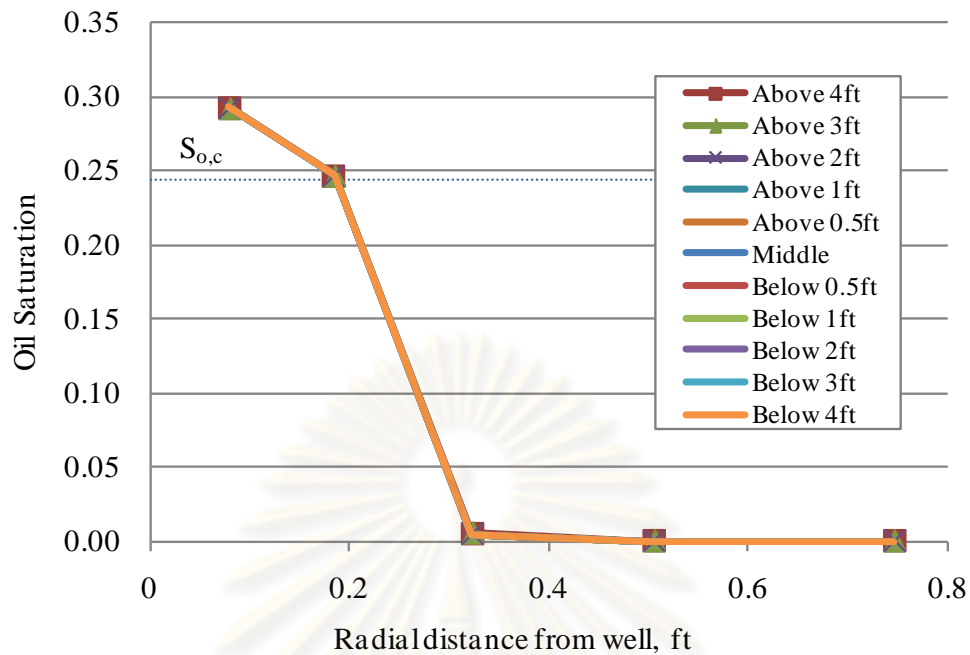


Figure 5.47: Condensate saturation profile at the end of drawdown for different probe positions.

If the probe is not centered in the formation, the spherical flow regime ends when the closest upper or lower boundary is reached. Then, hemispherical flow geometry develops until the second boundary is seen. The log-log derivative plots of all tests are shown in Figure 5.46. The arrow in the plot shows the increase in distance to the middle of formation. As expected, the derivative plot shows one more negative half-unit slope straight line, where the last one is a result of the hemispherical flow. The probe at the same distance from either the top or the bottom boundary results in the same pressure derivative behavior because of symmetry.

However, it can be seen that position of the probe doesn't affect the upper negative half slope straight line which is condensate banking effect since the change in position still results in the same pressure drop and also the same condensate saturation as shown in Table 5.13. There is only an influence on the lower negative half slope line due to the hemispherical flow as explained earlier. The longer the distance to the middle of the formation the probe is, the more noticeable the hemispherical flow, hence the shorter the spherical flow regime. This will affect the determination of spherical permeability. It should be noted that the hemispherical

flow may affect the upper negative half slope line if the size of condensate bank is larger than the spherical flow regime due to the increase of test duration or the increase of drawdown rate or the rich of the initial fluid. The interpreted results in Table 5.13 show acceptable values of estimated permeabilities. The error of estimated horizontal permeability (k_{xy}) is less than 6%, and the error of estimated vertical permeability (k_z) is no larger than 15%.

5.8 Effects of Permeability Anisotropy

In any model where there is a vertical contribution to flow, there must also be a pressure drop in the vertical direction, and vertical permeability has to be considered along with the radial permeability. The pressure drop due to the spherical flow is a near-wellbore effect caused by the anisotropy. To observe the effect of permeability anisotropy on the pressure behavior and condensate drop-out, five simulation cases were conducted for different permeability anisotropies starting from a k_z/k_{xy} ratio of 0.1 to 1 with intermediate ratios of 0.2, 0.5 and 0.8. The radial and theta permeabilities were controlled at 5 mD and the vertical permeability was changed from case to case corresponding to permeability anisotropy ratio as shown in Table 5.14. Fluid A was drawn at 2 Mscf/d, and the flow period consists of a 60-minute drawdown and a 60-minute build-up. The probe position was set at the middle of the formation. The schematic of reservoir description is shown in Figure 5.54.

After running reservoir simulation, the pressure response was then interpreted by Saphir. The interpreted results can be seen in Table 5.15. The diagnostic plots of the tests are shown in Figure 5.49. The condensate saturation profile is shown in Figure 5.50. The analytical model used for interpretation matched well with the data on log-log diagnostic plot for all cases as shown in Figures D41 to D45 in Appendix D, which an analytical model is shown as a green line and the pressure derivative is shown as a red line.

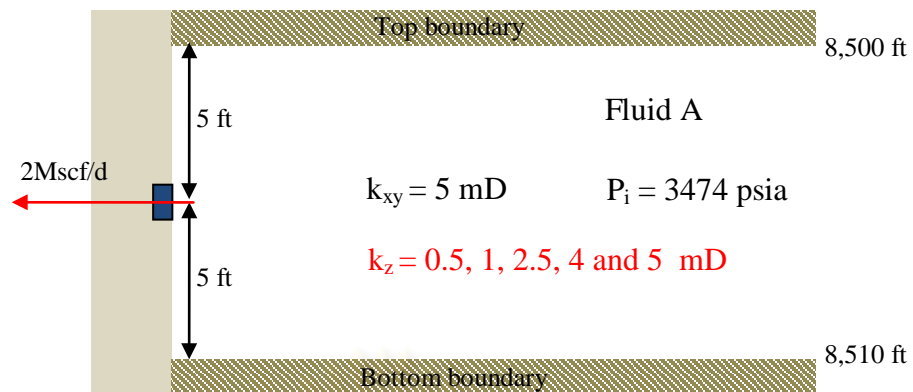


Figure 5.48: Schematic of a single layer reservoir for different permeability anisotropies.

Table 5.14: Case definition for different permeability anisotropies.

Case	k_{xy} (mD)	k_z/k_{xy}	k_z (mD)	Drawdown rate (Mscf/d)	ΔP^* (psia)
A-0.5kz	5	0.1	0.5	2.0	643.6
A-1kz	5	0.2	1.0	2.0	544.3
A-2.5kz	5	0.5	2.5	2.0	373.0
A-4kz	5	0.8	4.0	2.0	296.9
A-5kz	5	1.0	5.0	2.0	263.2

* pressure drop at the end of drawdown

Table 5.15: Interpreted results for different permeability anisotropies.

Case	Interpreted			Error			Skin	R_{inv} (ft)	k_z/k_{xy} (early time)
	k_{xy} (mD)	k_z/k_{xy}	Calc. k_z (mD)	k_{xy} (%)	k_z/k_{xy} (%)	k_z (%)			
A-0.5kz	3.12	0.113	0.58	2.3	13.00	15.6	1.25	67.9	0.0023
A-1kz	2.92	0.232	1.11	-4.3	16.00	11.1	1.20	65.7	0.0109
A-2.5kz	2.9	0.583	2.77	-4.9	16.60	10.9	1.05	65.4	0.0893
A-4kz	2.96	0.828	4.02	-3.0	3.50	0.4	0.93	66.1	0.1934
A-5kz	2.89	1.140	5.40	-5.2	14.00	8.0	0.87	65.3	0.2955

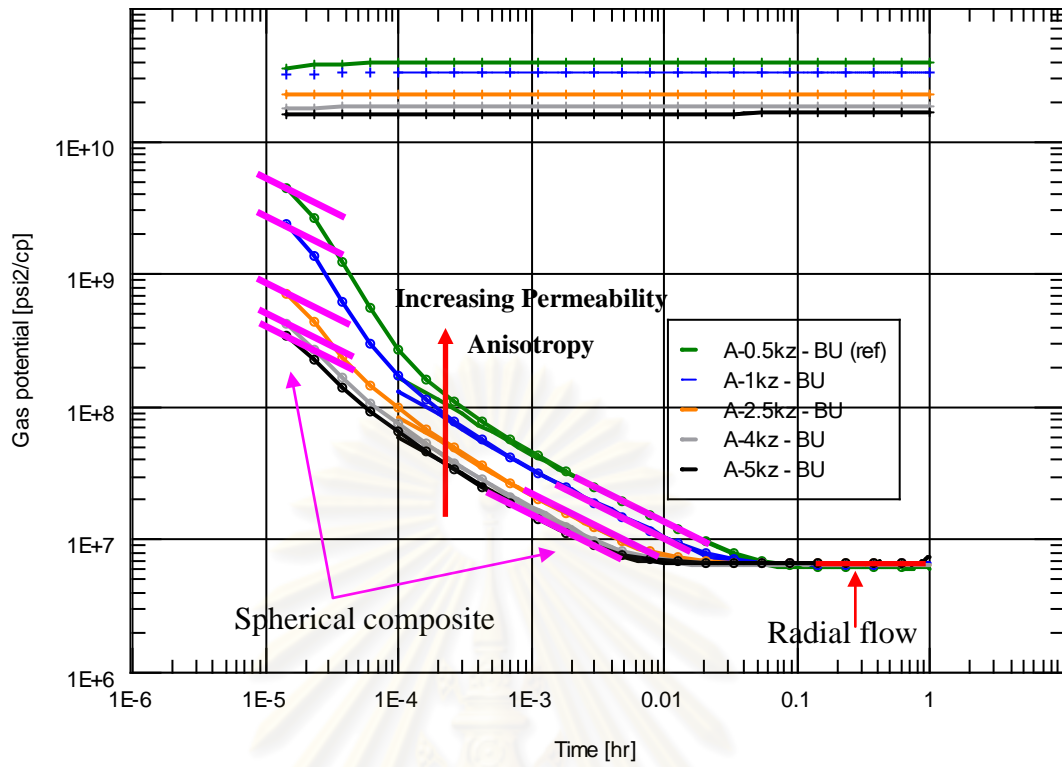


Figure 5.49: Derivative plot for different permeability anisotropies.

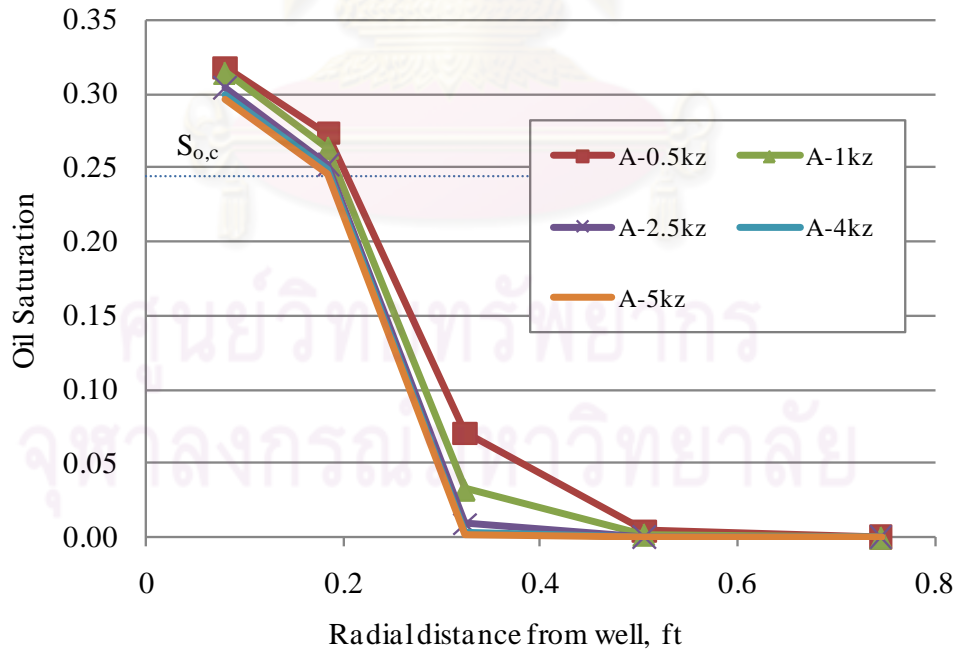


Figure 5.50: Condensate saturation for different permeability anisotropies.

The log-log derivative plots of all these tests are shown in Figure 5.49. The arrow in the plot shows the decrease in permeability anisotropy. It can be seen that the period of spherical flow regime is longer as a permeability anisotropy ratio decreases. Therefore, in order to see the radial flow regime in very low permeability anisotropy reservoir, the test needs to be conducted for a longer drawdown time or longer build-up time or higher drawdown rate.

As k_z decreases, the upper negative half slope straight line becomes increasingly evident. Since the pressure drop due to the spherical flow is a near-wellbore effect caused by the anisotropy, the pressure drop increases as the permeability ratio, k_z/k_{xy} , decreases (permeability anisotropy increases). This results in an increase in total skin as shown in Table 5.15, an increase in condensate saturation as shown in Figure 5.50 and also an increase in clarity of the upper negative half slope straight line as shown in Figure 5.49. It should be noted that the spherical composite behavior may not be seen if the permeability ratio is too high as shown in case A-5kz.

The interpreted results in Table 5.15 show acceptable values of estimated permeabilities. The error of estimated horizontal permeability (k_{xy}) is less than 5%, and the error of estimated vertical permeability (k_z) is no larger than 16%.

5.9 Effects of Horizontal Permeability

To study the effect of horizontal permeability on the pressure behavior and condensate drop-out, five simulation cases were conducted for different horizontal permeabilities while keeping the permeability anisotropy ratio at 0.2. The radial and theta permeabilities were varied from 1 mD to 100 mD with intermediate value of 3, 5, 8, 10 and 50 mD while the vertical permeability was changed from case to case to obtain permeability anisotropy of 0.2 as shown in Table 5.16. Fluid A was drawn at 1 Mscf/d and the flow period consists of a 60-minute drawdown and a 60-minute build-up. The probe position was set at the middle of the formation. The schematic of reservoir description is shown in Figure 5.51. After running simulation, the pressure response was then interpreted by Saphir. The analytical model used for interpretation shows good matches on log-log diagnostic plots for all cases except for the case A-1k which cannot match with an analytical model as shown in Figures D46 to D52 in

Appendix D, which an analytical model is shown as a green line and the pressure derivative is shown as a red line. The interpreted results can be seen in Table 5.17.

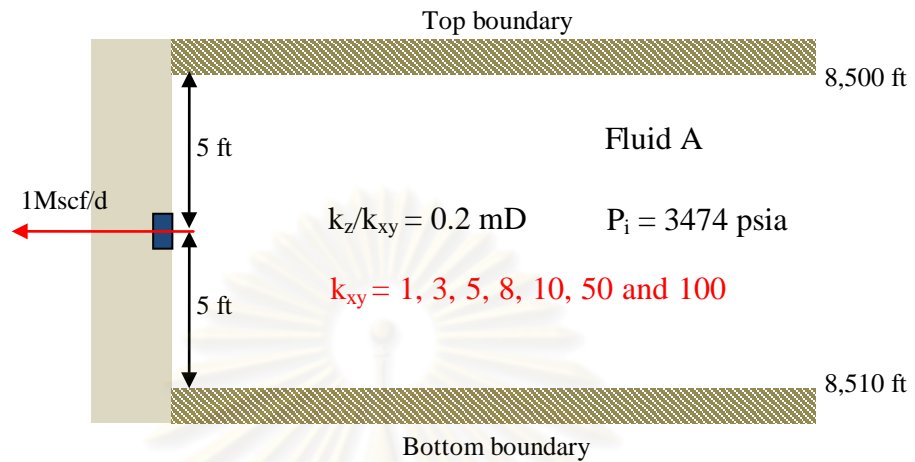


Figure 5.51: Schematic of a single layer reservoir for different horizontal permeabilities.

Table 5.16: Case definition for different horizontal permeabilities.

Case	k_{xy} (mD)	k_z (mD)	$k_{xy, \text{eff}}$ (mD)	Drawdown rate (Mscf/d)	ΔP^* (psia)
A-1k	1	0.2	0.61	1.0	485.5
A-3k	3	0.6	1.83	1.0	420.2
A-5k	5	1.0	3.05	1.0	223.8
A-8k	8	1.6	4.88	1.0	109.1
k-10k	10	2.0	6.10	1.0	78.1
A-50k	50	10	30.5	1.0	7.5
A-100k	100	20	61.0	1.0	3.7

* pressure drop at the end of drawdown

Table 5.17: Interpreted results for different horizontal permeabilities.

Case	Interpreted			Error			Skin	R _{inv} (ft)	k _z /k _{xy} (early time)
	k _{xy} (mD)	k _z /k _{xy}	Calc. k _z (mD)	k _{xy} (%)	k _z /k _{xy} (%)	k _z (%)			
A-1k	-	-	-	-	-	-	-	-	-
A-3k	1.74	0.234	0.67	-4.9	17.00	11.2	1.1	50.8	0.0082
A-5k	2.93	0.226	1.09	-3.9	13.00	8.6	1.0	65.7	0.0394
A-8k	4.73	0.222	1.72	-3.1	11.00	7.6	0.8	83.6	0.0910
k-10k	5.82	0.230	2.19	-4.6	15.00	9.7	0.7	92.7	0.1124
A-50k	28.1	0.240	11.06	-7.9	20.00	10.6	0.0	204	-
A-100k	60.2	0.224	22.11	-1.3	12.00	10.5	0.0	298	-

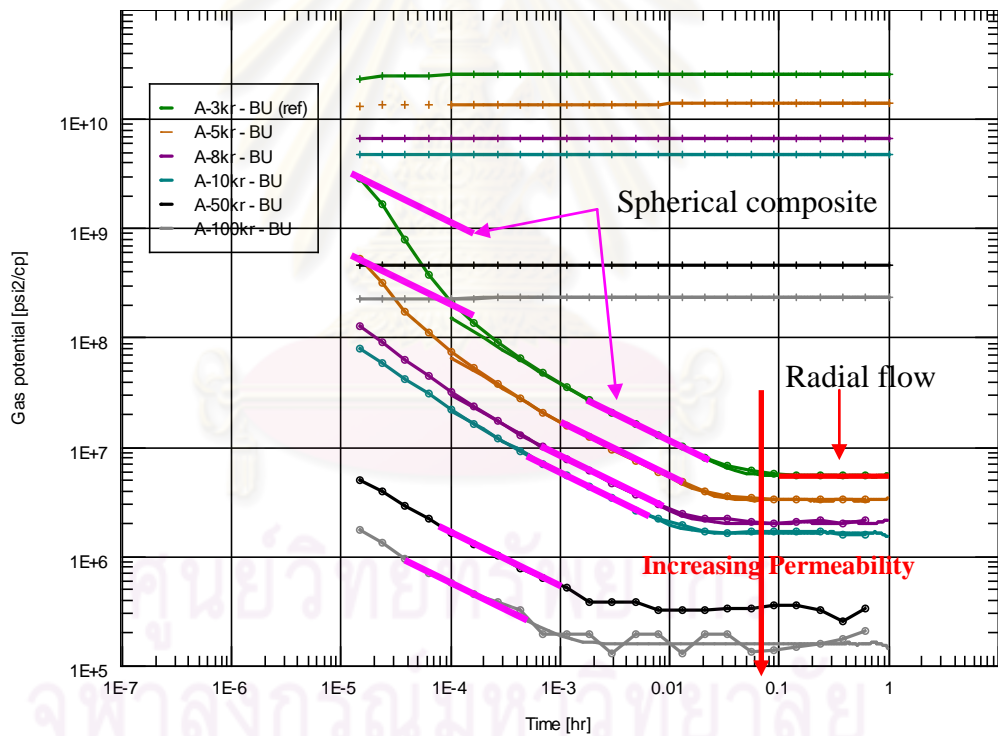


Figure 5.52: Derivative plots for different horizontal permeabilities.

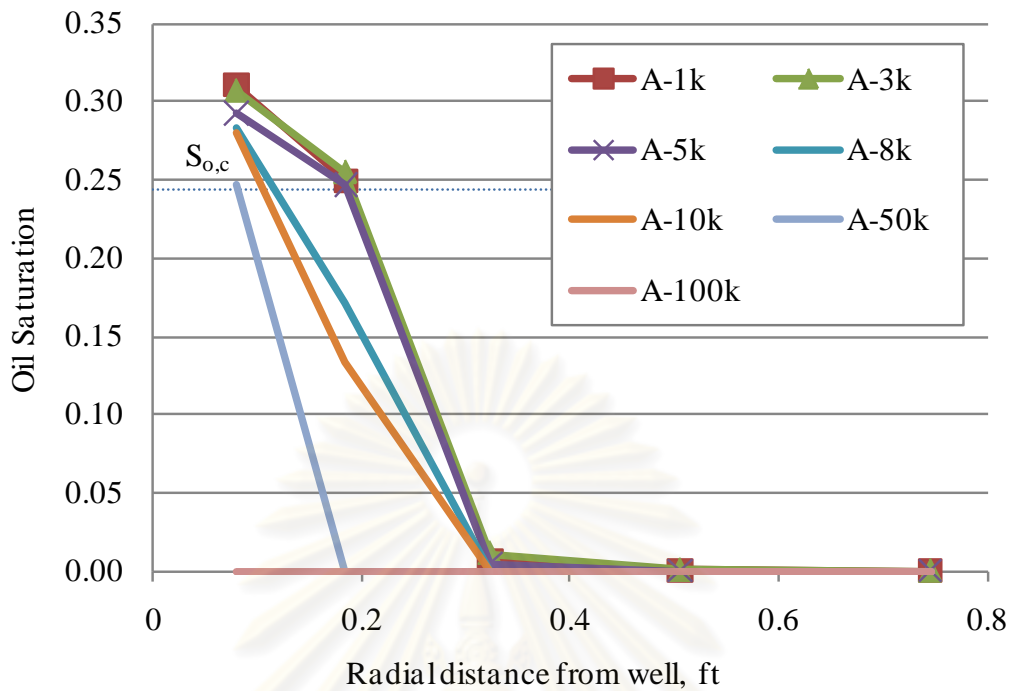


Figure 5.53: Condensate saturation for different horizontal permeabilities.

The permeability indicates how easy fluid can flow through the rock. As horizontal permeability increases, the fluid can flow through the reservoir easier, resulting in lower pressure drop as shown in Table 5.16, longer radius of investigation of the formation test as shown in Table 5.17, and also higher fluid mobility as can be observed as lower derivative curve in Figure 5.52. This is why the stabilization lines corresponding to radial flow regime are observed earlier as permeability increases.

The derivative plots of all tests except case A-1k are shown in Figure 5.52. The derivative plot of case A-1k cannot be interpreted because the formation is too tight resulting in the uncontrollable flow rate and also the unstable pressure response. The arrow in the plot shows the increase in horizontal permeability. As can be seen from the figure, spherical composite behavior can be observed on derivative plot in low permeability reservoir. However, it's difficult to notice condensate banking effect when the horizontal permeability is too high.

As k_{xy} decreases, the upper negative half slope straight line due to condensate banking effect becomes increasingly noticeable. The pressure drop increases as the permeability decreases. This results in the increase in total skin, higher condensate

saturation due to more condensate drop-out as shown in Figure 5.53, and also clearer upper negative half slope straight line. It should be noted that the spherical composite behavior may not be seen if the permeability is too high (higher than 8 mD in this study).

The interpreted results in Table 5.17 show acceptable values of estimated permeabilities. The error of estimated horizontal permeability (k_{xy}) is less than 8%, and the error of estimated vertical permeability (k_z) is no larger than 11%.

5.10 Effects of Initial Reservoir Pressure

To understand the effect of reservoir pressure on the pressure behavior and condensate saturation, seven simulation cases were carried out at different reservoir pressures: 3474, 3468, 3460, 3400, 3000, 2600 and 2200 psia. The dew point pressure of Fluid A is at 3468 psia. The condensate saturation is not zero when the reservoir pressure is below the dew point pressure. Fluid A was drawn at 1 Mscf/d, and the flow period consists of a 60-minute drawdown and a 60-minute build-up. The probe position was set at the middle of the formation. The radial and theta permeabilities are 5 mD, and the vertical permeability is 1 mD. The schematic of reservoir description is shown in Figure 5.54. After running reservoir simulation, the pressure response was then interpreted by Saphir. The interpreted results can be seen in Table 5.18. The analytical model used for interpretation matched well with the data on log-log diagnostic plot for all cases as shown in Figures D53 to D59 in Appendix D

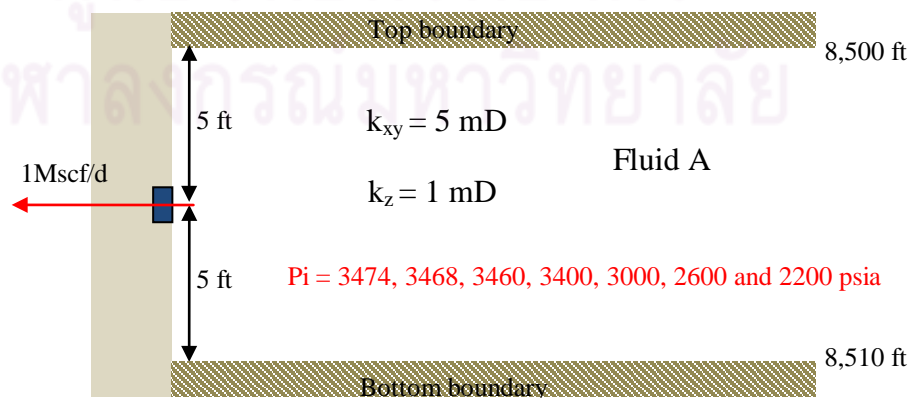
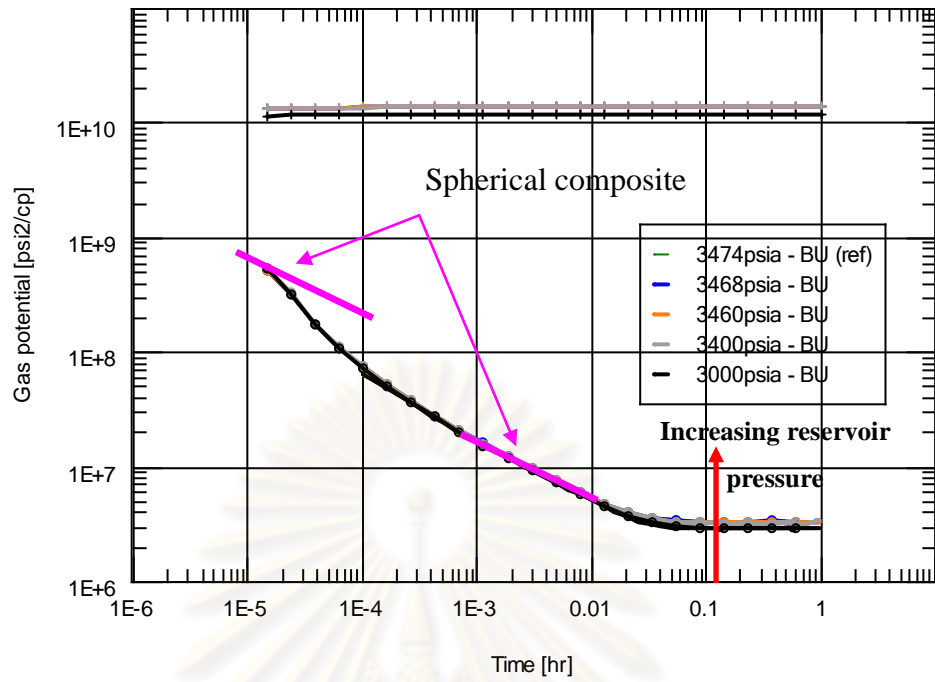
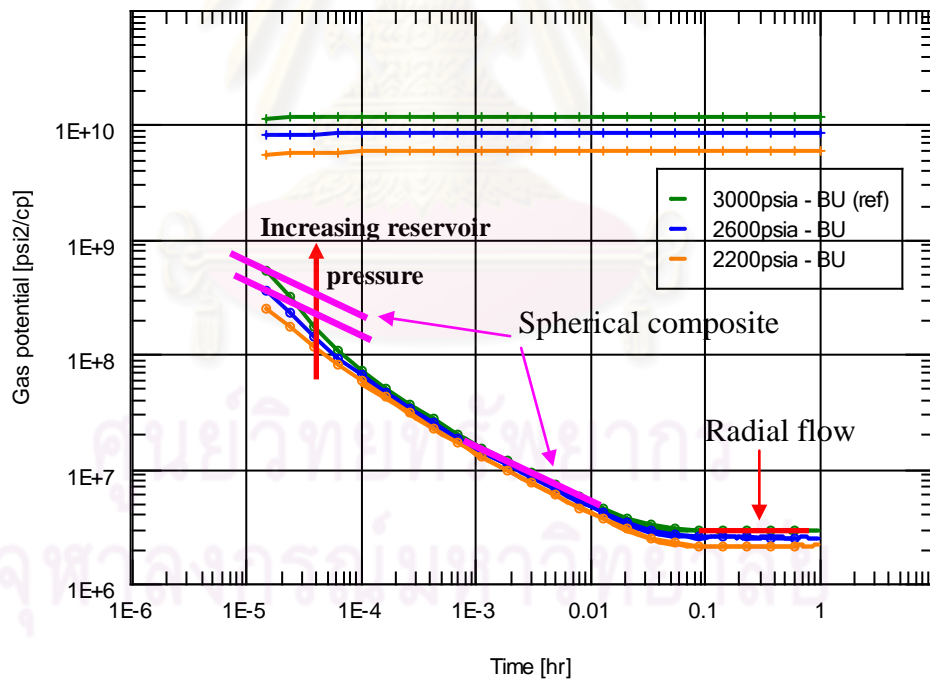


Figure 5.54: Schematic of a single layer reservoir with different reservoir pressures.



(a): For reservoir pressure above 3,000 psia.



(b): For reservoir pressure below 3,000 psia.

Figure 5.55: Derivative plot for different reservoir pressures.

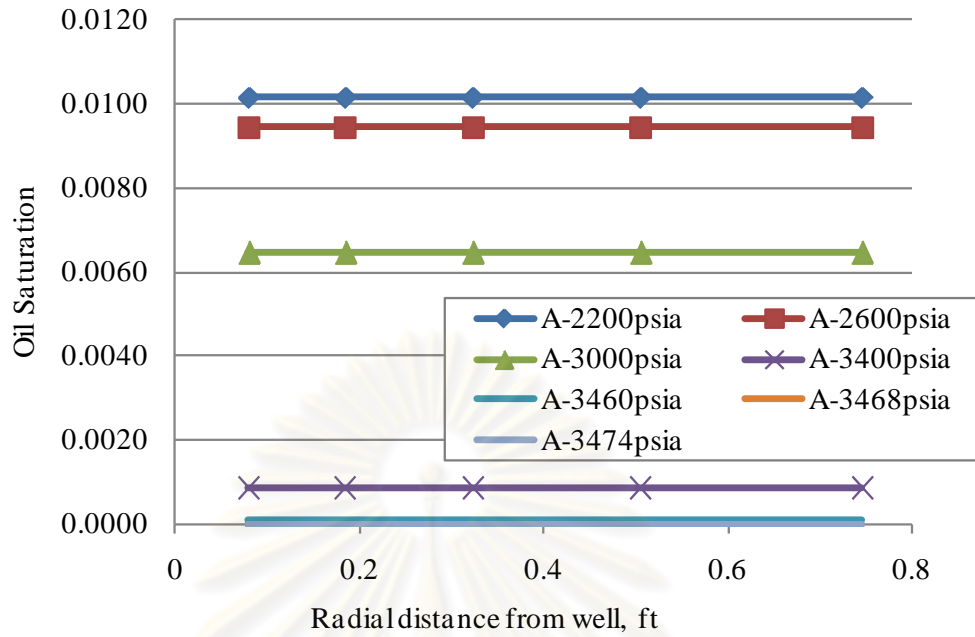


Figure 5.56: Initial condensate saturation for different reservoir pressures.

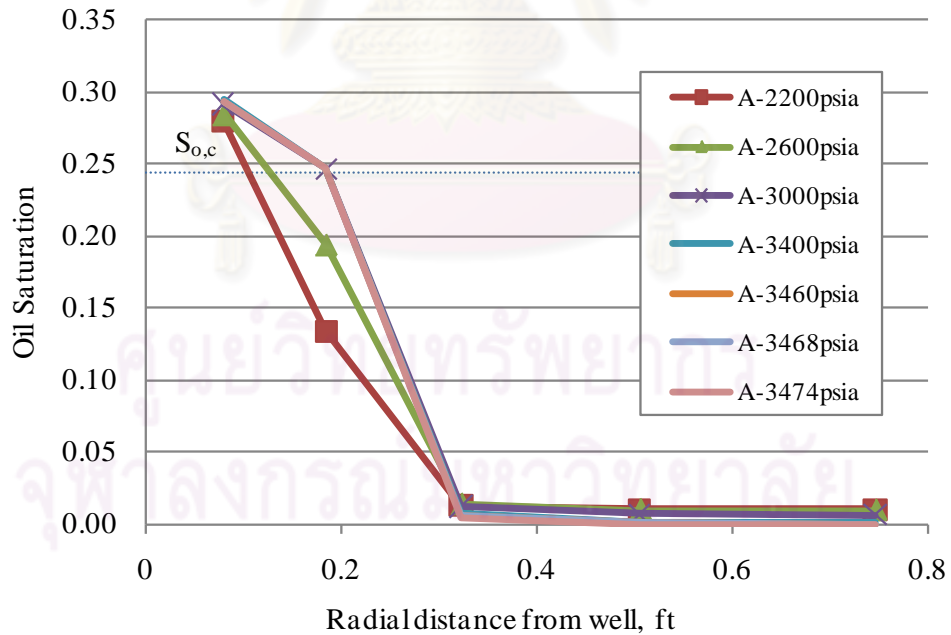


Figure 5.57: Condensate saturation profile at the end of drawdown for different reservoir pressures.

Table 5.18: Interpreted results for different reservoir pressure.

Case	ΔP below P_{dew} (psia)	Interpreted			Error			Skin	R_{inv} (ft)	k_z/k_{xy} (early time)
		k_{xy} (mD)	k_z/k_{xy}	Calc. k_z (mD)	k_{xy} (%)	k_z/k_{xy} (%)	k_z (%)			
A-2200	176.4	2.91	0.236	1.13	-4.6	18.00	12.6	0.63	54.0	0.0689
A-2600	195.7	2.89	0.230	1.09	-5.2	15.00	9.0	0.81	57.8	0.0528
A-3000	224.7	2.91	0.219	1.04	-4.6	9.50	4.5	0.99	61.7	0.0346
A-3400	222.5	2.92	0.224	1.07	-4.3	12.00	7.2	1.03	65.1	0.0367
A-3460	218.7	2.91	0.228	1.09	-4.6	14.00	8.8	1.02	65.5	0.0393
A-3468	218.2	2.91	0.230	1.10	-4.6	15.00	9.7	1.03	65.4	0.0400
A-3474	217.8	2.93	0.226	1.09	-3.9	13.00	8.6	1.02	65.7	0.0394

The log-log derivative plots of all these tests are shown in Figure 5.55. The arrow in the plot shows the increase in initial reservoir pressure. The different in initial reservoir pressure causes the different in initial condensate saturation as shown in Figure 5.56. It shows that spherical composite behavior can be seen clearly when the initial reservoir pressure is above 2,600 psia as shown in Figure 5.55. The derivative plots are approximately the same when the reservoir pressure is more than 3,000 psia as shown in Figure 5.55(a) because drawdown pressures are approximately the same and resulting in the same condensate saturation profiles as shown in Figure 5.57.

When comparing between reservoir pressure of 2200 psia and 2600 psia, Figure 5.55(b) shows that the upper negative half slope straight line can be seen clearer when the reservoir pressure is 2600 psia whereas the condensate saturations at the probe cell are approximately the same as shown in Figure 5.57. However, the condensate saturation at the block adjacent to the probe block in case of 2600 psia initial reservoir pressure is higher because of higher pressure drop. This is why the spherical composite behavior can be seen clearer as the reservoir pressure increases.

The interpreted results in Table 5.18 show that WFT pressure response in gas condensate reservoir can be used to estimate reservoir permeability with an acceptable error even when the reservoir pressure is below the dew point pressure. The error of estimated horizontal permeability (k_{xy}) is less than 6%, and the error of estimated vertical permeability (k_z) is no larger than 13%.

CHAPTER VI

CONCLUSIONS AND RECOMMENDATIONS

In this chapter, the conclusions of simulated wireline formation test in gas condensate reservoir under certain reservoir conditions are presented. The recommendations for future works are also outlined.

6.1 Conclusions

In this study, a reservoir simulator was used to simulate pressure response in a single layer homogeneous gas condensate reservoir when tested with a wireline formation test. A number of simulations were run to investigate condensate bank on the pressure behavior and also on the phase behavior under different reservoir conditions. After that, a pressure transient analysis software was used to interpret the pressure response from the simulation by using formation test model option.

Initially, a single probe formation test was simulated in a single layer homogeneous reservoir using lean gas condensate in order to investigate the pressure behavior, derivative behavior and also phase behavior when the flowing probe pressure is above and below the dew point pressure.

Then, the model was modified to examine the effects of important parameters. The influences of drawdown rate, initial reservoir fluid, test duration, probe size, probe position, initial reservoir pressure, permeability anisotropy and horizontal permeability are investigated.

From the simulation and interpretation results shown in Chapter 5, it can be concluded as follows:

1. When the flowing probe pressure is higher than the dew point pressure, the derivative plot exhibits two responses which are (1) a negative half slope straight line corresponding to spherical flow near the wellbore and (2) a zero slope straight line stabilized at the effective gas permeability corresponding to radial flow regime.

2. When the flowing probe pressure is lower than the dew point pressure, a spherical composite behavior (parallel negative half-unit slope straight lines) and radial flow behavior (zero slope straight line) can be observed from derivative plot obtained from wireline formation test data in gas condensate reservoir as condensate bank develops in the reservoir.
 - a. The upper negative half slope straight line (condensate drop out effect) on the derivative plot corresponds to the spherical mobility of condensate bank while the lower negative half slope straight line corresponds to the spherical mobility of original gas in spherical flow regime.
 - b. The zero-slope straight line corresponds to the mobility of original gas in radial flow regime.
 - c. The level of upper negative half slope straight line varies with the condensate saturation which is dependent on the pressure drop of the test.
3. As the pressure drops below the dew point, the component composition changes which the intermediate and heavy component drops out of the gas, Hence, the mixture fluid becomes heavier and heavier while the gas phase becomes leaner and leaner. The phase behavior gradually changes from gas condensate behavior to volatile oil behavior.
4. The effects of condensate drop out on pressure response is dependent on
 - a. Drawdown rate
 - b. Initial Reservoir fluid
 - c. Drawdown duration
 - d. Probe size
 - e. Permeability anisotropy
 - f. Horizontal permeability
 - g. Initial reservoir pressure
5. Wireline formation test pressure response can be used to identify condensate banking by PTA technique and also can be used to estimate reservoir permeability with an acceptable value even when condensate banking occurs.

6.2 Recommendations

1. The relative permeability curves have an impact on the condensate banking; therefore, the effects of relative permeability should be studied.
2. The spherical composite behavior is early time response. Therefore, the effects of tool storage should further be studied.
3. There is no an analytical model of spherical composite behavior in the interpretation software. A comprehensive study is needed to derive the solution for interpretation of this kind of pressure response.
4. In this study, only a single layered reservoir is considered. Therefore, the multilayer reservoir should be investigated.
5. Only a single probe formation tester was simulated in this report. Therefore, the new formation test tool, i.e., dual packer or quicksilver probe, should be further studied.
6. In this study, only the pressure responses from the simulation were analyzed. Therefore, the actual WFT pressure data should be observed to compare with this study.

References

- [1] Muskat, M. Physical Principles of Oil Production. New York: McGraw-Hill Book, 1949.
- [2] Fussell, D.D. Single-well performance predictions for gas condensate reservoirs. Journal of Petroleum Technology (1973): 860-870.
- [3] Afidick, D., Kaczorowski, N.J., and Bette, S. Production Performance of a Retrograde Gas Reservoir: A Case Study of Arun Field. paper SPE 28749 presented at the SPE Asia Pacific Oil and Gas Conference, Australia. 7-10 November, 1994.
- [4] Fevang, Ø. and Whitson, C.H. Modelling gas condensate well deliverability. paper SPE 30714 presented at the SPE Annual Technical Conference and Exhibition, Dallas, Texas. 22-25 October, 1995.
- [5] Barnum, R.S., Brinkman, F.P., Richardson, T.W., and Spillette, A.G. Gas condensate reservoir behaviour: productivity and recovery reduction due to condensation. paper SPE 30767 presented at the SPE Annual Technical Conference and Exhibition, Dallas, Texas. 22-25 October, 1995.
- [6] Kniazeff, V.J. and Naville, S.A. Two-phase flow of volatile hydrocarbons. Journal Society of Petroleum Engineer (1965): 37.
- [7] Gondouin, M., Iffly, R., and Husson, J. An attempt to predict the time dependence of well deliverability in gas-condensate fields. Journal Society of Petroleum Engineer (1967): 112-124.
- [8] Kalaydjian, F.J.-M., Bourbiaux, B.J., and Lambard, J.-M. Predicting Gas-Condensate Reservoir Performance: How flow parameters are altered when approaching Production Wells. paper SPE 36715 presented at the 1996 SPE Annual Conference and Exhibition, Colorado. 6-9 October, 1996.

- [9] Ali, J.K., McGauley, P.J., and Wilson, C.J. Experimental Studies and Modelling of Gas Condensate Flow Near the Wellbore. paper SPE 39053 presented at the Fifth Latin American and Caribbean Petroleum Engineering Conference and Exhibition, Brazil. 1997.
- [10] Novosad, Z. Compositional and phase changes in testing and producing retrograde gas wells. paper SPE 35645 presented at the Gas Technology Conference, Calgary, Alberta, Canada. 28 April - 1 March, 1996.
- [11] Roussenac, B. Gas Condensate Well Analysis. M.S. Thesis Department of Petroleum Engineering Stanford University, 2001.
- [12] Wheaton, R.J. and Zhang, H.R. Condensate Banking Dynamics in Gas Condensate Fields: Compositional Changes and Condensate Accumulation Around Production Wells. paper SPE 62930 presented at 2000 SPE Annual Technical Conference and Exhibition held in Dallas, Texas. 1-4 October, 2000.
- [13] Bengherbia, M., Tiab, D., and Zhu, T. Gas-Condensate Well Performance Using Compositional Simulator - A Case Study. paper SPE 75531 presented at SPE Gas Technology Symposium, Calgary, Alberta, Canada. 30 April - 2 May, 2002.
- [14] Economides, M.J., Dehghani, K., Ogbe, D.O., and Ostermann, R.D. Hysteresis Effects for Gas Condensate Wells Undergoing Build-up Tests below the Dew Point Pressure. paper SPE16748 presented at the 62nd Annual Technical Conference and Exhibition of the Society of Petroleum Engineers, Texas. 27-30 September, 1987.

- [15] Danesh, A., Khazam, M., Henderson, G.M., Therani, D.H., and Peden, J.M. Gas Condensate Recovery Studies. DTI Improve Oil Recovery and Research Dissemination Seminar presented at London. June, 1994.
- [16] Gringarten, A.C., Daungkaew, S., Al-Lamki, A., Mott, R., and Whittle, T.M. Well test analysis in gas-condensate reservoirs. paper SPE 62920 presented at SPE Annual Technical Conference and Exhibition held in Dallas, Texas. 1-4 October, 2000.
- [17] Daungkaew, S. and Gringarten, A.C. The Effect of Capillary Number on a Condensate Blockage in Gas-Condensate Reservoirs. Walailak Journal of Science and Technology (2004): 91-116.
- [18] Gringarten, A.C., Bozorgzadeh, M., Daungkaew, S., and Hashemi, A. Well Test Analysis in Lean Gas Condensate Reservoirs: Theory and Practice. paper SPE 100993 presented at SPE Russian Oil and Gas Technical Conference and Exhibition, Moscow, Russia. 3-6 October, 2006.
- [19] Aluko, O.A. and Gringarten, A.C. Well Test Dynamics in Rich Gas Condensate Reservoirs under Gas Injection. paper SPE 121848 presented at SPE EUROPEC/EAGE Annual Conference and Exhibition, Amsterdam, Netherlands. 8-11 June, 2009.
- [20] Doll, H.-G., Method and Apparatus for Determining Hydraulic Characteristics of Formations Traversed by a Borehole, U.S. Patent, No. 2747401, 29-May, 1956.
- [21] Moran, J.H. and Finklea, E.E. Theoretical Analysis of Pressure Phenomena Associated with the Wireline Formation Test Data. paper SPE 177 presented at 36th Annual Fall Meeting of SPE in Dallas, Nevada, U.S.A.: 8-11 October, 1962.

- [22] Horner, D.R. Pressure Build-ups in Wells. World Petroleum Congress presented at 3rd World Petroleum Congress, Hague, Netherlands. 28 May - 6 June, 1951.
- [23] Culham, W.W. Pressure Buildup Equations for Spherical Flow Regime Problems. paper SPE 4053 presented at the SPE-AIME 47th Annual Fall Meeting, San Antonio, Texas, U.S.A.: 8-11 October 1974.
- [24] Stewart, G. and Wittman, M. Interpretation of the Pressure Response of the Repeat Formation Tester. paper SPE 8362 presented at the 54th Annual Fall Conference and Exhibition, Las Vegas, Nevada, U.S.A.: 23-26 September, 1979.
- [25] Dussan, E.B. and Sharma, Y. An Analysis of the Pressure Response of a Single Probe Formation tester. paper SPE 16801 presented at the 62nd Annual Fall Conference and Exhibition, Dallas, Texas, U.S.A.: 27-30 September, 1987.
- [26] Goode, P.A. and Thambynayagam, R.K.M. Influence of an Invaded Zone on a Multiprobe Formation Tester. paper SPE 23030 presented at the SPE Asia Pacific Conference, Perth, Australia. 4-7 November, 1991.
- [27] Kuchuk, F.J., Ramakrishnan, T.S., and Dave, Y., I. Interpretation of Wireline Formation Tester Packer and Probe Pressures. paper SPE 28404 presented at the 69th Annual Technical Conference and Exhibition, New Orleans, Louisiana, U.S.A.: 25-28 September, 1994.
- [28] Proett, M.A., Waid, M.C., and Kessler, C. Real Time Pressure Transient Analysis Method Applied to Wireline Formation Test Data. paper SPE 28449 presented at the 69th Annual Technical Conference and Exhibition, New Orleans, Louisiana, U.S.A.: 25-28 September, 1994.

- [29] Frimann-Dahl, C., Irvine-Fortescue, J., Rokke, E., Vik, S., and O., W. Formation Testers vs. DST The Cost Effective Use of Transient Analysis to Get Reservoir Parameters. paper SPE 48962 presented at the 1998 SPE Annual Technical Conference and Exhibition, New Orleans, Louisiana. 27-31 September, 1998.
- [30] Whittle, T.M., Lee, J., and Gringarten, A.C. Will Wireline Formation Tests Replace Well Tests? paper SPE 84086 presented at SPE Annual Technical Conference and Exhibition, Denver, Colorado, USA.: 5-8 October, 2003.
- [31] Daungkaew, S., Prosser, D., Manescu, A., and Molaes, M. An Illustration of the Information that can be Obtained from Pressure Transient Analysis of Wireline Formation Test Data. paper SPE 88560 presented at SPE Asia Pacific Oil and Gas Conference and Exhibition, Perth, Australia. 18-20 October, 2004.
- [32] Bourdet, D. Well Test Analysis: The Use of Advanced Interpretation Models. Amsterdam: Elsevier, 2002.
- [33] Horne, R.N. Modern Well Test Analysis: A Computer-Aided Approach. U.S.A.: Petroway, 1998.
- [34] Bourdet, D.P., Whittle, T.M., Douglas, A.A., and Pirard, Y.M. A New Set of Type Curves Simplifies Well Test Analysis. World Oil (May 1983): 95-106.
- [35] Schlumberger. Fundamentals of Formation Testing. Texas: Schlumberger Marketing Communications, 2006.
- [36] Schlumberger Wireline Formation Testing and Sampling. MDT Houston DS Interpretation Help Document. Texas: Schlumberger, 1996.

- [37] Daungkaew, S., Harfoushian, J.H., Cheong, B., Akinsanmi, O., Yeo, J., and Toulekima, S. Mini-DST Applications for Shell Deepwater Malaysia. paper SPE 109279 presented at the 2007 SPE Asia Pacific Oil & Gas Conference and Exhibition held in Jakarta, Indonesia. 30 October–1 November, 2007.
- [38] Muruais, J.M. and Young, A.A. Reducing Uncertainty Through Downhole Fluid Analysis: A Field Case Study. paper SPE 101151 presented at the 2006 SPE Asia Pacific Oil & Gas Conference and Exhibition held in Adelaide, Australia. 11-13 September, 2006.
- [39] Schlumberger. LFA Live Fluid Analyzer. Texas: Schlumberger, 2001.
- [40] Schlumberger. CFA Composition Fluid Analyzer. Texas: Schlumberger, 2004.
- [41] McCain, W.D. The Properties of Petroleum Fluids. Oklahoma: PennWell, 1989.
- [42] Bradley, H.B. Petroleum Engineering Handbook. U.S.A.: Society of Petroleum Engineers, 1992.
- [43] Danesh, A. PVT and Phase Behaviour of Petroleum Fluids. Amsterdam: Elsevier, 1998.
- [44] Fan, L., Harris, B.W., Jamaluddin, A.J., Kamath, J., Mott, R., Pope, G.A., Shandrygin, A., and Whitson, C.H. Understanding Gas-Condensate Reservoirs. Oilfield Review (Winter 2005): 14-27.
- [45] Yisheng, F., Baozhu, L., Yongle, H., Zhidao, S., and Yuxin, Z. Condensate Gas Phase Behaviour and Development. paper SPE 509025 presented at the 1998 SPE International Conference and Exhibition in China held in Beijing. 2-6 November, 1998.

- [46] Kyi, K.K., Yahaya, N., Daungkaew, S., Hademi, N.R., Cheong, B., Azam, M.N.H.M., Yusuf, N., Sinnappu, S., Anh, D.Q., Wong, S.B.R., and Minh, N.H. Fluid Identification Challenges in the Near Critical Fluids: Case Studies in Malaysia. paper SPE 123430 presented at the 2009 SPE Asia Pacific Oil and Gas Conference and Exhibition held in Jakarta, Indonesia. 4-6 August 2009.
- [47] Al-Lamki, A. Effect of Rate-Dependent Relative Permeabilities on Interpretation of Gas-Condensate Well Tests. Centre for Petroleum Studies Imperial College, 1999.
- [48] Shi, C. Flow Behavior of Gas-Condensate Wells. Department of Petroleum Engineering Stanford University, 2005.
- [49] Raghavan, R., Chu, W., and Jones, J. Practical considerations in the analysis of gas condensate well test paper SPE 30576 presented at the 70th Annual Technical Conference and Exhibition of the Society of Petroleum Engineers, Dallas, Texas. 22-25 October, 1995.
- [50] Kenyon, D.E. and Behie, G.A. Third SPE Comparative Solution Project: Gas Cycling of Retrograde Condensate Reservoirs. Journal of Petroleum Technology (1987): 981-997.



APPENDICES

ศูนย์วิทยทรัพยากร
จุฬาลงกรณ์มหาวิทยาลัย

APPENDIX A

Additional Simulation Data Used.

Table A1: Time step used in the simulation.

n	Δt , day	t, day	t, hr
T1	0.00000000010	0.00000000010	0.00000000240
T2	0.00000000016	0.00000000026	0.00000000630
T3	0.00000000026	0.00000000053	0.00000001262
T4	0.00000000043	0.00000000095	0.00000002288
T5	0.00000000069	0.00000000165	0.00000003954
T6	0.00000000113	0.00000000277	0.00000006658
T7	0.00000000183	0.00000000460	0.00000011047
T8	0.00000000297	0.00000000757	0.00000018171
T9	0.00000000482	0.00000001239	0.00000029735
T10	0.00000000782	0.00000002021	0.00000048504
T11	0.00000001269	0.00000003290	0.00000078970
T12	0.00000002060	0.00000005351	0.00000128420
T13	0.00000003344	0.00000008695	0.00000208686
T14	0.00000005428	0.00000014124	0.00000338969
T15	0.00000008811	0.00000022935	0.00000550439
T16	0.00000014302	0.00000037237	0.00000893688
T17	0.00000023214	0.00000060451	0.00001450834
T18	0.00000037681	0.00000098132	0.00002355167
T19	0.00000061161	0.00000159293	0.00003823040
T20	0.00000099274	0.00000258568	0.00006205625
T21	0.00000161138	0.00000419705	0.00010072927
T22	0.00000261551	0.00000681257	0.00016350157
T23	0.00000424538	0.00001105795	0.00026539070
T24	0.00000689091	0.00001794885	0.00043077249
T25	0.00001118501	0.00002913386	0.00069921268
T26	0.00001815500	0.00004728886	0.00113493257
T27	0.00002946836	0.00007675722	0.00184217325
T28	0.00004783170	0.00012458892	0.00299013410
T29	0.00007763824	0.00020222716	0.00485345186
T30	0.00012601885	0.00032824602	0.00787790436
T31	0.00020454806	0.00053279408	0.01278705789
T32	0.00033201310	0.00086480718	0.02075537228

n	Δt, day	t, day	t, hr
T33	0.00053890854	0.00140371572	0.03368917720
T34	0.00087473179	0.00227844751	0.05468274016
T35	0.00141982479	0.00369827230	0.08875853523
T36	0.00230459493	0.00600286723	0.14406881351
T37	0.00374071350	0.00974358073	0.23384593763
T38	0.00607175576	0.01581533649	0.37956807581
T39	0.00985539736	0.02567073385	0.61609761235
T40	0.01599593282	0.04166666667	1.00000000000
T41	0.00000000010	0.04166666677	1.00000000240
T42	0.00000000016	0.04166666693	1.00000000630
T43	0.00000000026	0.04166666719	1.00000001262
T44	0.00000000043	0.04166666762	1.00000002288
T45	0.00000000069	0.04166666831	1.00000003954
T46	0.00000000113	0.04166666944	1.00000006658
T47	0.00000000183	0.04166667127	1.00000011047
T48	0.00000000297	0.04166667424	1.00000018171
T49	0.00000000482	0.04166667906	1.00000029735
T50	0.00000000782	0.04166668688	1.00000048504
T51	0.00000001269	0.04166669957	1.00000078970
T52	0.00000002060	0.04166672018	1.00000128420
T53	0.00000003344	0.04166675362	1.00000208686
T54	0.00000005428	0.04166680790	1.00000338969
T55	0.00000008811	0.04166689602	1.00000550439
T56	0.00000014302	0.04166703904	1.00000893688
T57	0.00000023214	0.04166727118	1.00001450834
T58	0.00000037681	0.04166764799	1.00002355167
T59	0.00000061161	0.04166825960	1.00003823040
T60	0.00000099274	0.04166925234	1.00006205625
T61	0.00000161138	0.04167086372	1.00010072927
T62	0.00000261551	0.04167347923	1.00016350157
T63	0.00000424538	0.04167772461	1.00026539070
T64	0.00000689091	0.04168461552	1.00043077249
T65	0.00001118501	0.04169580053	1.00069921268
T66	0.00001815500	0.04171395552	1.00113493257
T67	0.00002946836	0.04174342389	1.00184217325
T68	0.00004783170	0.04179125559	1.00299013410
T69	0.00007763824	0.04186889383	1.00485345186
T70	0.00012601885	0.04199491268	1.00787790436
T71	0.00020454806	0.04219946075	1.01278705789
T72	0.00033201310	0.04253147384	1.02075537228

n	Δt, day	t, day	t, hr
T73	0.00053890854	0.04307038238	1.03368917720
T74	0.00087473179	0.04394511417	1.05468274016
T75	0.00141982479	0.04536493897	1.08875853523
T76	0.00230459493	0.04766953390	1.14406881351
T77	0.00374071350	0.05141024740	1.23384593763
T78	0.00607175576	0.05748200316	1.37956807581
T79	0.00985539736	0.06733740051	1.61609761235
T80	0.01599593282	0.08333333333	2.00000000000



ศูนย์วิทยทรัพยากร
จุฬาลงกรณ์มหาวิทยาลัย

Table A2: Grid size for large probe.

Radial direction		Theta direction		Vertical direction	
grid	grid size (ft)	grid	grid size (degree)	grid	grid size (ft)
1	0.0796	1	17.6029	1	1.6293
2	0.1050	2	8.5832	2	1.1150
3	0.1384	3	9.8907	3	0.7528
4	0.1825	4	11.3975	4	0.5082
5	0.2406	5	13.1338	5	0.3431
6	0.3172	6	15.1347	6	0.2317
7	0.4183	7	17.4403	7	0.1564
8	0.5515	8	20.0972	8	0.1056
9	0.7271	9	23.1589	9	0.0713
10	0.9587	10	26.6869	10	0.0481
11	1.2640	11	25.6753	11	0.07681
12	1.6665	12	25.6753	12	0.0481
13	2.1973	13	26.6869	13	0.0713
14	2.8971	14	23.1589	14	0.1056
15	3.8197	15	20.0972	15	0.1564
16	5.0362	16	17.4403	16	0.2317
17	6.6401	17	15.1347	17	0.3431
18	8.7548	18	13.1338	18	0.5082
19	11.5430	19	11.3975	19	0.7528
20	15.2191	20	9.8907	20	1.1150
21	20.0661	21	8.5832	21	1.6293
22	26.4567	Sum	360.0000	Sum	10.0000
23	34.8825				
24	45.9917				
25	60.6390				
26	79.9510				
27	105.4135				
28	138.9852				
29	183.2487				
30	241.6091				
Sum	1000.0000				

Table A3: Grid size for extra-large probe.

Radial direction		Theta direction		Vertical direction	
grid	grid size (ft)	grid	grid size (degree)	grid	grid size (ft)
1	0.0796	1	27.0837	1	1.6086
2	0.1050	2	8.5832	2	1.1150
3	0.1384	3	9.8907	3	0.7528
4	0.1825	4	11.3975	4	0.5082
5	0.2406	5	13.1338	5	0.3431
6	0.3172	6	15.1347	6	0.2317
7	0.4183	7	17.4403	7	0.1564
8	0.5515	8	20.0972	8	0.1056
9	0.7271	9	23.1589	9	0.0713
10	0.9587	10	26.6869	10	0.0481
11	1.2640	11	20.9349	11	0.11817
12	1.6665	12	20.9349	12	0.0481
13	2.1973	13	26.6869	13	0.0713
14	2.8971	14	23.1589	14	0.1056
15	3.8197	15	20.0972	15	0.1564
16	5.0362	16	17.4403	16	0.2317
17	6.6401	17	15.1347	17	0.3431
18	8.7548	18	13.1338	18	0.5082
19	11.5430	19	11.3975	19	0.7528
20	15.2191	20	9.8907	20	1.1150
21	20.0661	21	8.5832	21	1.6086
22	26.4567	Sum	360.0000	Sum	10.0000
23	34.8825				
24	45.9917				
25	60.6390				
26	79.9510				
27	105.4135				
28	138.9852				
29	183.2487				
30	241.6091				
Sum	1000.0000				

Table A4: Grid size to set standard probe at 3 ft below the middle of the formation.

Radial direction		Theta direction		Vertical direction	
grid	grid size (ft)	grid	grid size (degree)	grid	grid size (ft)
1	0.0796	1	7.4485	1	4.6515
2	0.1050	2	8.5832	2	1.1150
3	0.1384	3	9.8907	3	0.7528
4	0.1825	4	11.3975	4	0.5082
5	0.2406	5	13.1338	5	0.3431
6	0.3172	6	15.1347	6	0.2317
7	0.4183	7	17.4403	7	0.1564
8	0.5515	8	20.0972	8	0.1056
9	0.7271	9	23.1589	9	0.0713
10	0.9587	10	26.6869	10	0.0481
11	1.2640	11	30.7525	11	0.0325
12	1.6665	12	30.7525	12	0.0481
13	2.1973	13	26.6869	13	0.0713
14	2.8971	14	23.1589	14	0.1056
15	3.8197	15	20.0972	15	0.1564
16	5.0362	16	17.4403	16	0.2317
17	6.6401	17	15.1347	17	0.3431
18	8.7548	18	13.1338	18	0.5082
19	11.5430	19	11.3975	19	0.5192
20	15.2191	20	9.8907	20	0.0000
21	20.0661	21	8.5832	21	0.0000
22	26.4567	Sum	360.0000	Sum	10.0000
23	34.8825				
24	45.9917				
25	60.6390				
26	79.9510				
27	105.4135				
28	138.9852				
29	183.2487				
30	241.6091				
Sum	1000.0000				

APPENDIX B

Script Example Used in ECLIPSE Simulator.

RUNSPEC

TITLE

title

START

1 'NOV' 2009 /

FIELD

MULTIN

RADIAL

MULTOUT

GAS

OIL

WATER

FULLIMP

COMPS

11 /

NOFREEZE



ศูนย์วิทยทรัพยากร
จุฬาลงกรณ์มหาวิทยาลัย

ISGAS

MONITOR

RSSPEC

NOINSPEC

MSGFILE

1 /

EOS

ZJ /

SCFDIMS

5 3 3 /

DIMENS

30 21 21 /

SCDPDIMS

0 0 0 0 1 0 /

EQLDIMS

1 100 100 1 20 /

REGDIMS

1 1 0 0 0 1 /

TABDIMS

1 1 50 50 1 20 20 1 1 1 1 1 1 0 0 1 /



ศูนย์วิทยทรัพยากร
ศาลงกรณ์มหาวิทยาลัย

WELLDIMS

2 2 2 2 5 10 5 4 3 0 1 1 /

GRID

GRIDFILE

2 /

--

ECHO

--

GRIDUNIT

--

-- Grid data units

--

'FEET' /

--

MAPAXES

--

-- Grid Axes wrt Map Coordinates

--

0 0 0 0 0 0 /

DRV

0.0796 0.105 0.1384 0.1825 0.2406 0.3172 0.4183 0.5515 0.7271 0.9587 1.264

1.6665 2.1973 2.8971 3.8197 5.0362 6.6401 8.7548 11.543 15.2191 20.0661 26.4567

34.8825 45.9917 60.639 79.951 105.4135 138.9852 183.2487 241.6091

/

DTHETAV

7.4485 8.5832 9.8907 11.3975 13.1338 15.1347 17.4403 20.0972 23.1589 26.6869

30.7525 30.7525 26.6869 23.1589 20.0972 17.4403 15.1347 13.1338 11.3975 9.8907
8.5832

/

DZV

1.6515 1.115 0.7528 0.5082 0.3431 0.2317 0.1564 0.1056 0.0713 0.0481 0.0325
0.0481 0.0713 0.1056 0.1564 0.2317 0.3431 0.5082 0.7528 1.115 1.6515

/

INRAD

--

-- Inner Radius

--

0.25 /

BOX

1 30 1 21 1 1 /

TOPS

630*8500

/

ENDBOX

CIRCLE

--

-- Requests Completion of the Circle

--

PERMR

13230*5

/

PERMTHT

13230*5



ศูนย์วิทยุโทรพยากร
จุฬาลงกรณ์มหาวิทยาลัย

/

PERMZ

13230*1

/

PORO

13230*0.1

/

PROPS

ECHO

--

STCOND

--

-- Standard Conditions

--

59.99999999999999 15

/

--

NCOMPS

--

-- Number of Components

--

11

/



ศูนย์วิทยทรัพยากร
จุฬาลงกรณ์มหาวิทยาลัย

```

--
CNAMES
--
-- Component Names
--
'N2'
'CO2'
'C1'
'C2'
'C3'
'NC4'
'NC5'
'PC1'
'PC2'
'PC3'
'PC4'
/
ECHO
--
PVTW
--
-- Water PVT Properties
--
2000 1 3e-006 0.42 1*
/
--
DENSITY
--
-- Fluid Densities at Surface Conditions
--
40 63 0.001

```



ศูนย์วิทยทรัพยากร
จุฬาลงกรณ์มหาวิทยาลัย

/

ECHO

ROCK

--

-- Rock Properties

--

3550 4e-006

/

ECHO

ZI

--

-- Overall Composition

--

0.0158

0.0241

0.796

0.0687

0.0357

0.0189

0.0088

0.026155

0.004584

0.001235

2.6e-005

/

EOS

--



ศูนย์วิทยทรัพยากร
จุฬาลงกรณ์มหาวิทยาลัย

-- Equation of State (Reservoir EoS)

--

SRK

/

PARACHOR

--

-- Component Parachors

--

41

79.7

77

108

150.3

189.9

231.5

326.044

516.904

769.015

1225.779

/

BIC

--

-- Binary Interaction Coefficients (Reservoir EoS)

--

-0.055

0.028 0.0762

0.061 0.1405 0

0.107 0.1365 0 0

0.1 0.1 0 0 0

0.197 0.1365 0 0 0 0

0.169	0.1365	0	0	0	0	0		
0.08	0.1365	0	0	0	0	0	0	
0.019	0.1365	0	0	0	0	0	0	0
0.1	0.1365	0	0	0	0	0	0	0

/

OMEGAB

--

-- EoS Omega-b Coefficient (Reservoir EoS)

--

0.08664

0.08664

0.08664

0.08664

0.08664

0.08664

0.08664

0.08664

0.08664

0.08664

0.08664

/

OMEGAA

--

-- EoS Omega-a Coefficient (Reservoir EoS)

--

0.42748

0.42748

0.42748

0.42748

0.42748

0.42748

0.42748

0.42748

0.42748

0.42748

0.42748

/

SSHIFT

--

-- EoS Volume Shift (Reservoir EoS)

--

0

0

0

0

0

0

0

0

0

0

0

/

ZCRIT

--

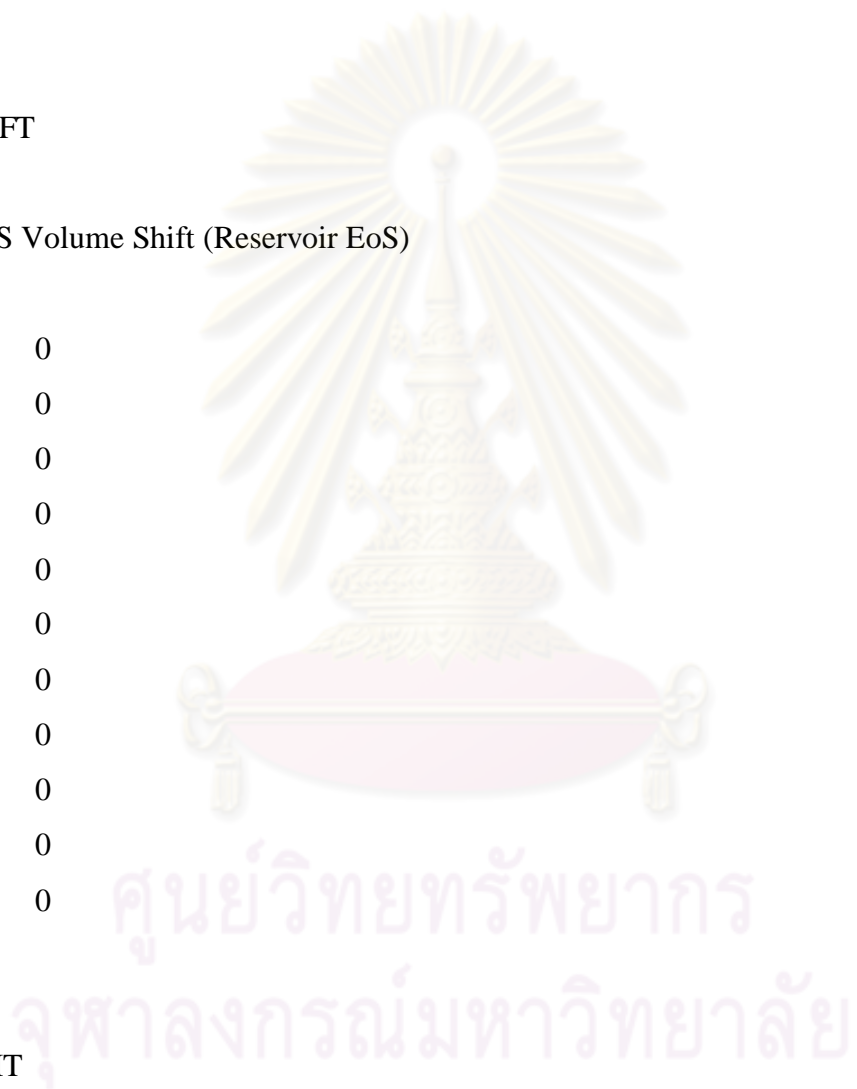
-- Critical Z-Factors (Reservoir EoS)

--

0.2907

0.2747

0.2875



0.2838

0.2828

0.2729

0.2653

0.2685

0.256

0.1879

0.1403

/

ACF

--

-- Acentric Factors (Reservoir EoS)

--

0.0403

0.2376

0.0111

0.099

0.1499

0.1977

0.2498

0.3256

0.592

0.773

1.23

/

TCRIT

--

-- Critical Temperatures (Reservoir EoS)

--

227.2



ศูนย์วิทยทรัพยากร
จุฬาลงกรณ์มหาวิทยาลัย

547.6

343

549.8

665.6

765.2

845.4

1005.2

1222.6

1411.5

1664.9

/

PCRIT

--

-- Critical Pressures (Reservoir EoS)

--

493.1

1071

666.7

707.8

615

548.8

488.1

408

302

172

95

/

MW

--

-- Molecular Weights (Reservoir EoS)



ศูนย์วิทยทรัพยากร
 จุฬาลงกรณ์มหาวิทยาลัย

--
 28.01
 44.01
 16.04
 30.07
 44.1
 58.12
 72.15
 109.03
 175.59
 263.51
 422.8

/

RTEMP

--
 -- Initial Reservoir Temperature

--
 251

/

ECHO

ZMFVD

--
 -- Total Composition vs Depth

--
 1000 0.0158
 0.0241
 0.796
 0.0687
 0.0357



ศูนย์วิทยทรัพยากร
 จุฬาลงกรณ์มหาวิทยาลัย

0.0189
 0.0088
 0.026155
 0.004584
 0.001235
 2.6e-005

/

ECHO

SWOF

--

-- Water/Condensate saturation Functions

--

0.297	0	0.897	21
0.319026	1.76e-005	0.769065	9.729116
0.341051	0.000141	0.653913	4.323714
0.363077	0.000476	0.55087	1.834439
0.385102	0.001128	0.459264	0.738872
0.407128	0.002203	0.378422	0.280633
0.429154	0.003807	0.307671	0.099699
0.451179	0.006045	0.246339	0.032803
0.473205	0.009024	0.193752	0.009874
0.49523	0.012849	0.149238	0.002677
0.517256	0.017625	0.112125	0.000641
0.539282	0.023459	0.081739	0.000132
0.561307	0.030456	0.057408	2.25e-005
0.583333	0.038722	0.038459	3.04e-006
0.605358	0.048363	0.024219	3.01e-007
0.627384	0.059484	0.014016	1.96e-008
0.64941	0.072192	0.007176	7e-010
0.671435	0.086592	0.003027	0

0.693461	0.102789	0.000897	0
0.715486	0.12089	0.000112	0
0.737512	0.141	0	0
1	1	0	0

/

SGOF

--

-- Gas/Condensate saturation Functions

--

0	0	0.897	0
0.03515	7.63e-005	0.705922744	0
0.0703	0.00061	0.544104174	0
0.10545	0.002059	0.409125388	0
0.1406	0.00488	0.298553376	0
0.17575	0.009531	0.20994098	0
0.2109	0.01647	0.140865082	0
0.24605	0.026154	0.088899992	0
0.2812	0.03904	0.051602703	0
0.31635	0.055586	0.026534281	0
0.3515	0.07625	0.011275309	0
0.38665	0.101489	0.003397664	0
0.4218	0.13176	0.000433119	0
0.45695	0.167521	0	0
0.4921	0.20923	0	0
0.52725	0.257344	0	0
0.5624	0.31232	0	0
0.59755	0.374616	0	0
0.6327	0.44469	0	0
0.66785	0.522999	0	0
0.703	0.61	0	0

/

SOLUTION

ECHO

EQUIL

--

-- Equilibration Data Specification

--

8505 3474 8600 0 8600 0 1* 1* 1* 1* 1*

/

SUMMARY

RUNSUM

EXCEL

BXMF

1 1 11 1 /

/

BXMF

2 1 11 1 /

/

BXMF

3 1 11 1 /

/

BXMF

4 1 11 1 /

/

BXMF

5 1 11 1 /



ศูนย์วิทยทรัพยากร
จุฬาลงกรณ์มหาวิทยาลัย

/
 BYMF
 1 1 11 1 /
 /
 BYMF
 2 1 11 1 /
 /
 BYMF
 3 1 11 1 /
 /
 BYMF
 4 1 11 1 /
 /
 BYMF
 5 1 11 1 /
 /
 BVMF
 1 1 11 1 /
 /
 BVMF
 2 1 11 1 /
 /
 BVMF
 3 1 11 1 /
 /
 BVMF
 4 1 11 1 /
 /
 BVMF
 5 1 11 1 /
 /
 BGKR



ศูนย์วิทยทรัพยากร
 จุฬาลงกรณ์มหาวิทยาลัย

1 1 11 /

/

BGKR

2 1 11 /

/

BGKR

3 1 11 /

/

BGKR

4 1 11 /

/

BGKR

5 1 11 /

/

BOKR

1 1 11 /

/

BOKR

2 1 11 /

/

BOKR

3 1 11 /

/

BOKR

4 1 11 /

/

BOKR

5 1 11 /

/

BOSAT

1 1 11 /

/



ศูนย์วิทยทรัพยากร

จุฬาลงกรณ์มหาวิทยาลัย

BOSAT

2 1 11 /

/

BOSAT

3 1 11 /

/

BOSAT

4 1 11 /

/

BOSAT

5 1 11 /

/

BPR

1 1 11 /

/

BPR

2 1 11 /

/

BPR

3 1 11 /

/

BPR

4 1 11 /

/

BPR

5 1 11 /

/

FGPR

FOPR

FPR

FWPR

WBHP



ศูนย์วิทยทรัพยากร
จุฬาลงกรณ์มหาวิทยาลัย

/

WBP

/

WGPR

/

WOPR

/

WWPR

/

SCHEDULE

ECHO

RPTRST

'BASIC=2' 'SGAS' 'SOIL' 'SWAT' /

WELSPECS

'WELL1' '1' 1 1 8505 'GAS' 1* 'STD' 'SHUT' 'YES' 1* 'SEG' 3* 'STD' /

/

COMPDAT

'WELL1' 1 1 11 11 'OPEN' 1 1* 0.5 3* 'Z' 1* /

/

WCONPROD

'WELL1' 'OPEN' 'GRAT' 2* 1 2* 20 9* /

/

TSTEP

1e-010 /

TSTEP

1.6e-010 /

TSTEP

2.6e-010 /

TSTEP

4.3e-010 /

TSTEP

6.9e-010 /

TSTEP

1.13e-009 /

TSTEP

1.83e-009 /

TSTEP

2.97e-009 /

TSTEP

4.82e-009 /

TSTEP

7.82e-009 /

TSTEP

1.269e-008 /



ศูนย์วิทยทรัพยากร
จุฬาลงกรณ์มหาวิทยาลัย

TSTEP

2.06e-008 /

TSTEP

3.344e-008 /

TSTEP

5.428e-008 /

TSTEP

8.811e-008 /

TSTEP

1.4302e-007 /

TSTEP

2.3214e-007 /

TSTEP

3.7681e-007 /

TSTEP

6.1161e-007 /

TSTEP

9.9274e-007 /

TSTEP

1.61138e-006 /

TSTEP

2.61551e-006 /



ศูนย์วิทยทรัพยากร
จุฬาลงกรณ์มหาวิทยาลัย

TSTEP

4.24538e-006 /

TSTEP

6.89091e-006 /

TSTEP

1.118501e-005 /

TSTEP

1.8155e-005 /

TSTEP

2.946836e-005 /

TSTEP

4.78317e-005 /

TSTEP

7.763824e-005 /

TSTEP

0.00012601885 /

TSTEP

0.00020454806 /

TSTEP

0.0003320131 /

TSTEP



ศูนย์วิทยทรัพยากร
จุฬาลงกรณ์มหาวิทยาลัย

0.00053890854 /

TSTEP

0.00087473179 /

TSTEP

0.00141982479 /

TSTEP

0.00230459493 /

TSTEP

0.0037407135 /

TSTEP

0.00607175576 /

TSTEP

0.00985539736 /

TSTEP

0.01599593282 /

WCONPROD

'WELL1' 'OPEN' 'GRAT' 2* 0 2* 20 9* /

/

TSTEP

1e-010 /

TSTEP

1.6e-010 /



ศูนย์วิทยทรัพยากร
จุฬาลงกรณ์มหาวิทยาลัย

TSTEP
2.6e-010 /

TSTEP
4.3e-010 /

TSTEP
6.9e-010 /

TSTEP
1.13e-009 /

TSTEP
1.83e-009 /

TSTEP
2.97e-009 /

TSTEP
4.82e-009 /

TSTEP
7.82e-009 /

TSTEP
1.269e-008 /

TSTEP
2.06e-008 /

TSTEP



ศูนย์วิทยทรัพยากร
จุฬาลงกรณ์มหาวิทยาลัย

3.344e-008 /

TSTEP

5.428e-008 /

TSTEP

8.811e-008 /

TSTEP

1.4302e-007 /

TSTEP

2.3214e-007 /

TSTEP

3.7681e-007 /

TSTEP

6.1161e-007 /

TSTEP

9.9274e-007 /

TSTEP

1.61138e-006 /

TSTEP

2.61551e-006 /

TSTEP

4.24538e-006 /



ศูนย์วิทยทรัพยากร
จุฬาลงกรณ์มหาวิทยาลัย

TSTEP

6.89091e-006 /

TSTEP

1.118501e-005 /

TSTEP

1.8155e-005 /

TSTEP

2.946836e-005 /

TSTEP

4.78317e-005 /

TSTEP

7.763824e-005 /

TSTEP

0.00012601885 /

TSTEP

0.00020454806 /

TSTEP

0.0003320131 /

TSTEP

0.00053890854 /

TSTEP

0.00087473179 /



ศูนย์วิทยทรัพยากร
จุฬาลงกรณ์มหาวิทยาลัย

TSTEP

0.00141982479 /

TSTEP

0.00230459493 /

TSTEP

0.0037407135 /

TSTEP

0.00607175576 /

TSTEP

0.00985539736 /

TSTEP

0.01599593282 /

END



ศูนย์วิทยทรัพยากร
จุฬาลงกรณ์มหาวิทยาลัย

APPENDIX C

Composition Profile during Drawdown of Fluid A.

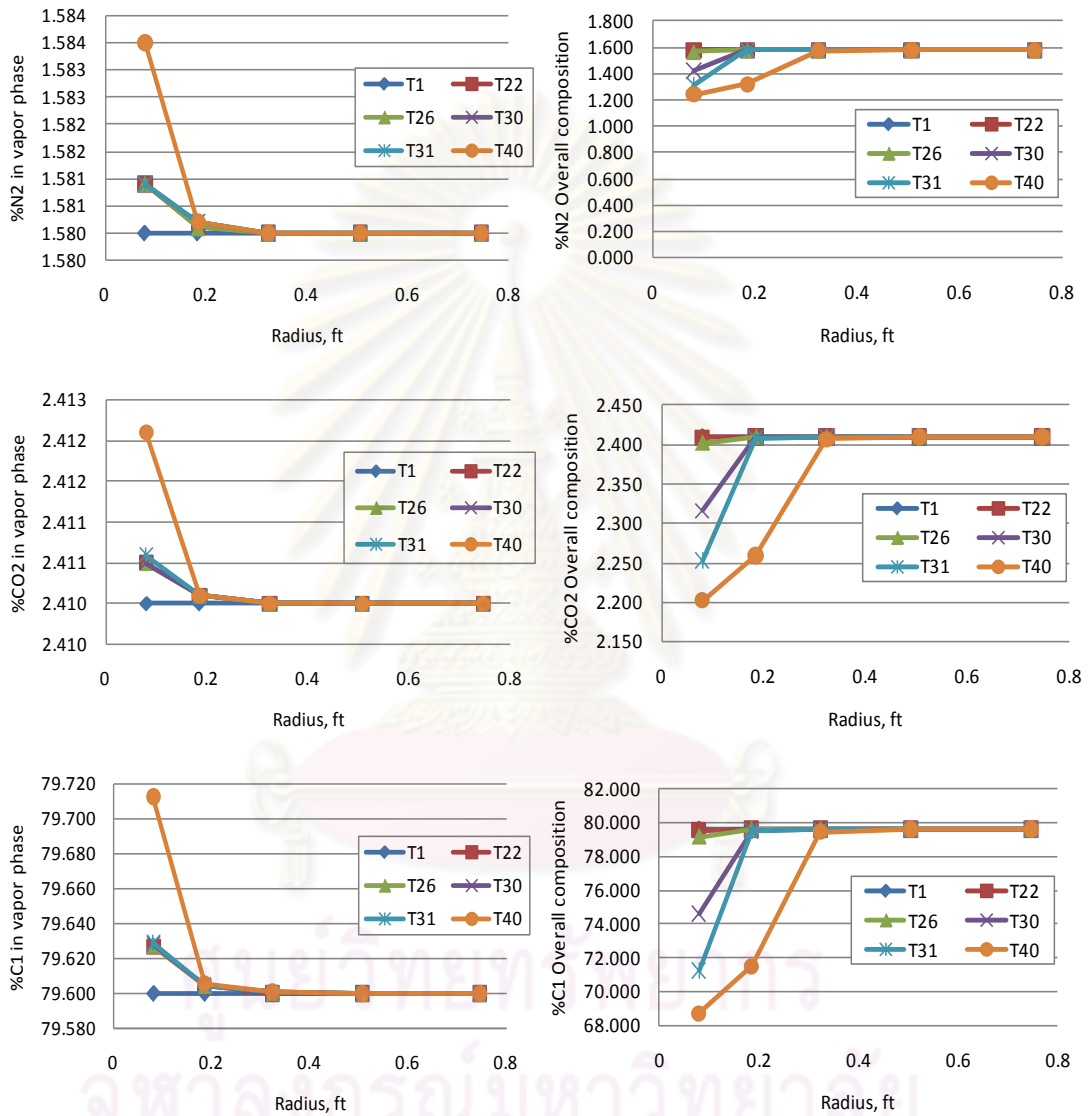


Figure C1: Compositions profile during drawdown of Fluid A with 1 Mscf/d.

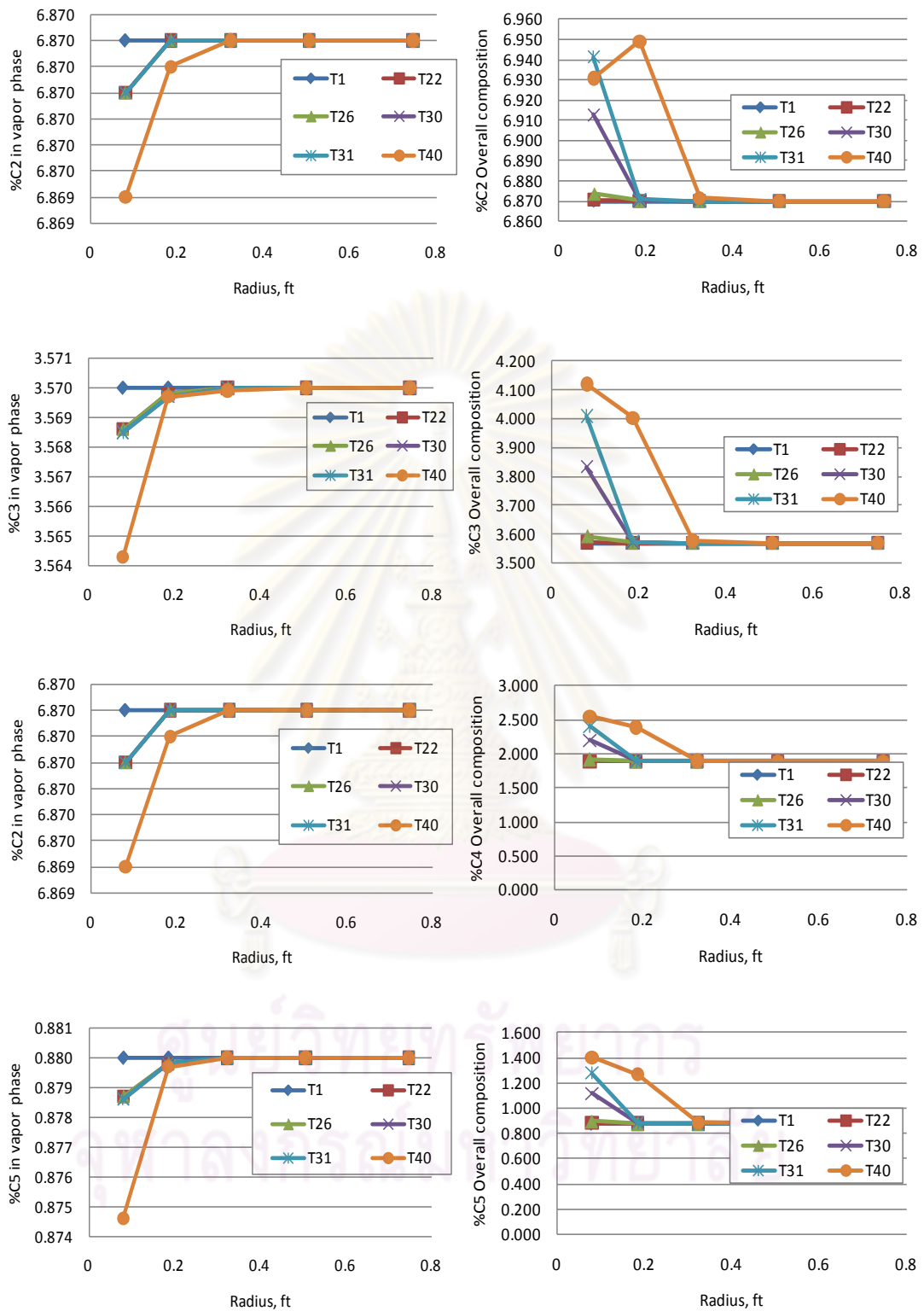


Figure C1: Compositions profile during drawdown of Fluid A with 1 Mscf/d.(Continue)

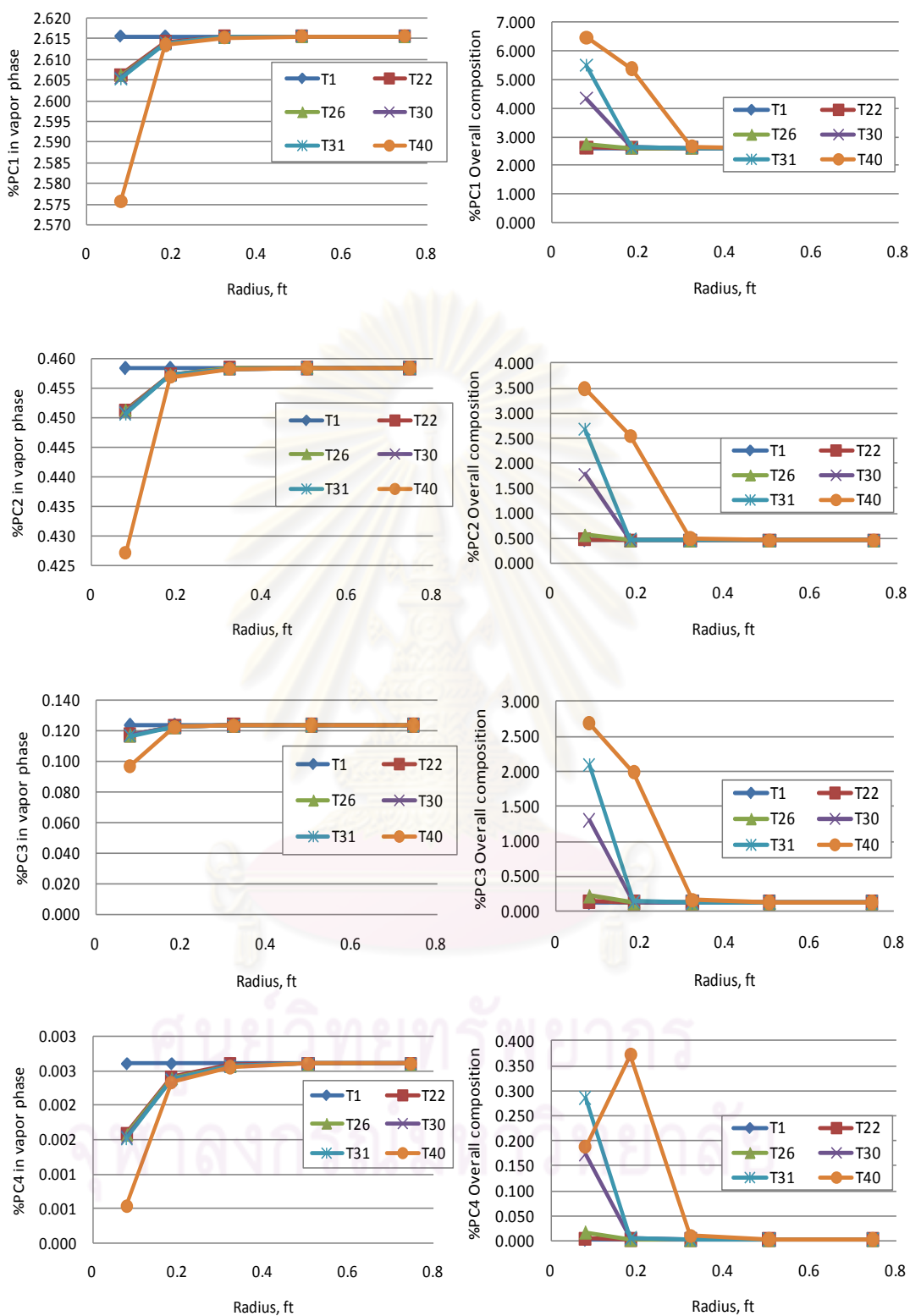


Figure C1: Compositions profile during drawdown of Fluid A with 1 Mscf/d.(Continue)

Composition Profile during Build-up of Fluid A.

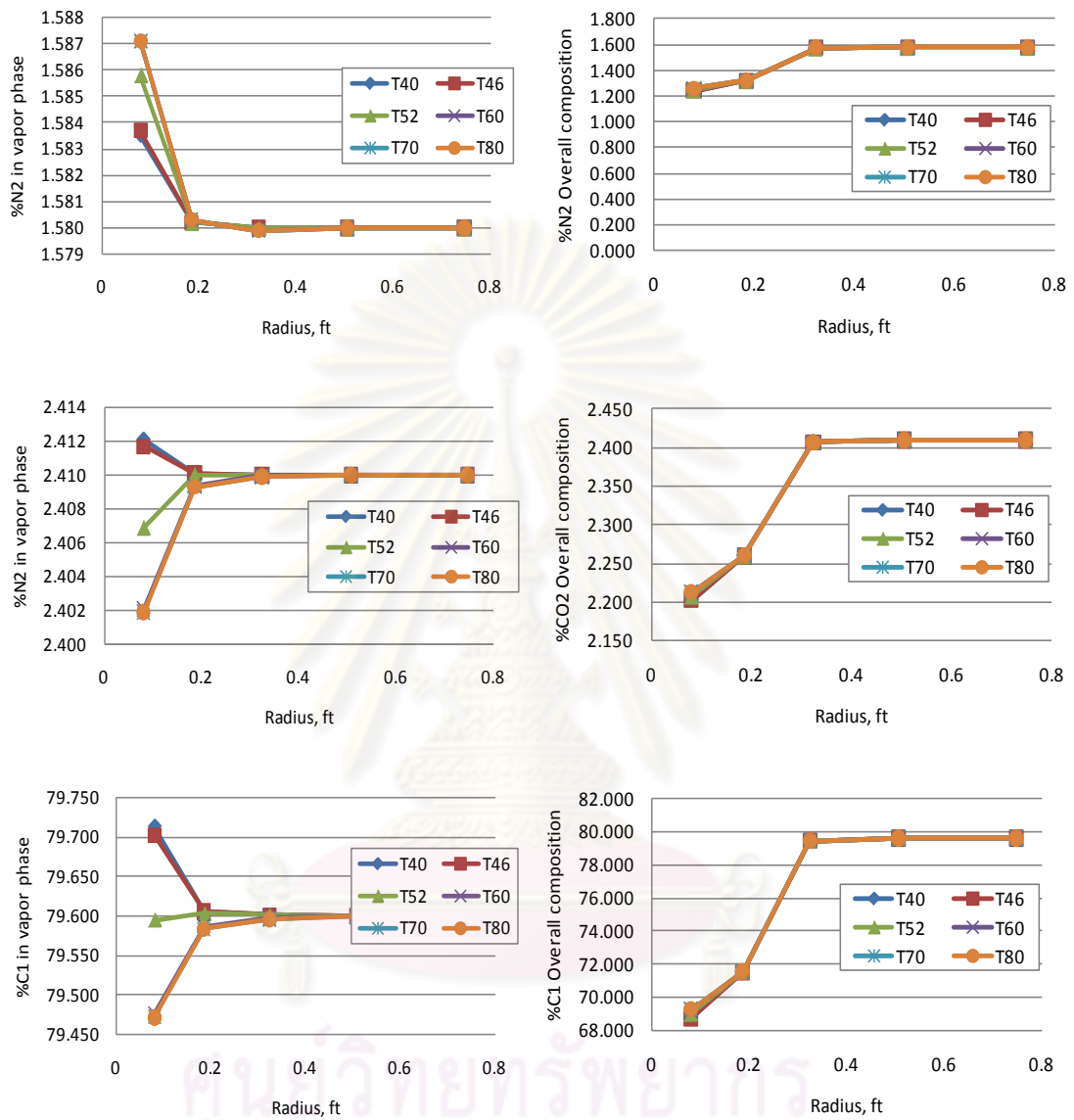


Figure C2: Compositions profile during build-up of Fluid A with 1 Mscf/d.

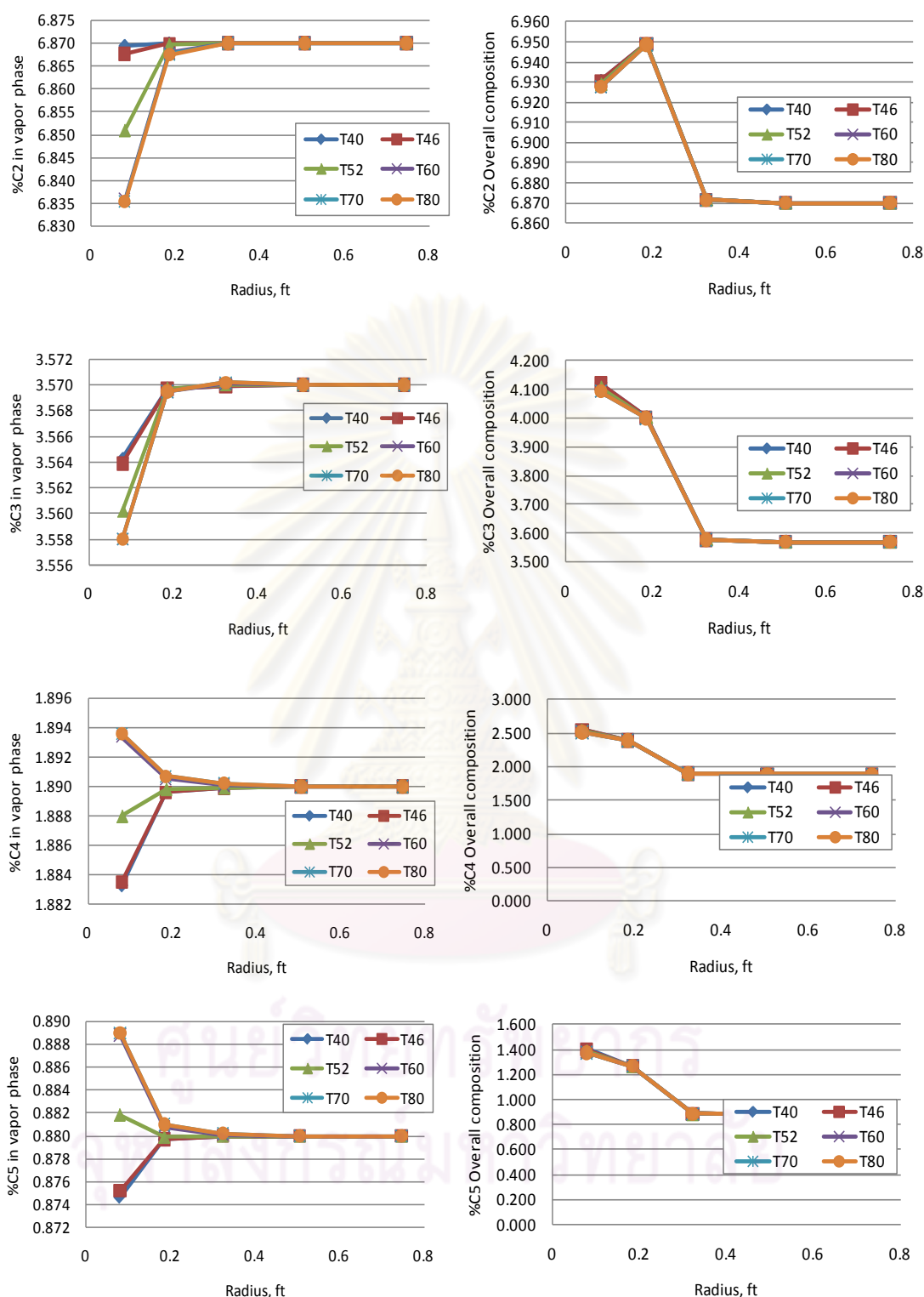


Figure C2: Compositions profile during build-up of Fluid A with 1 Mscf/d.(Continue)

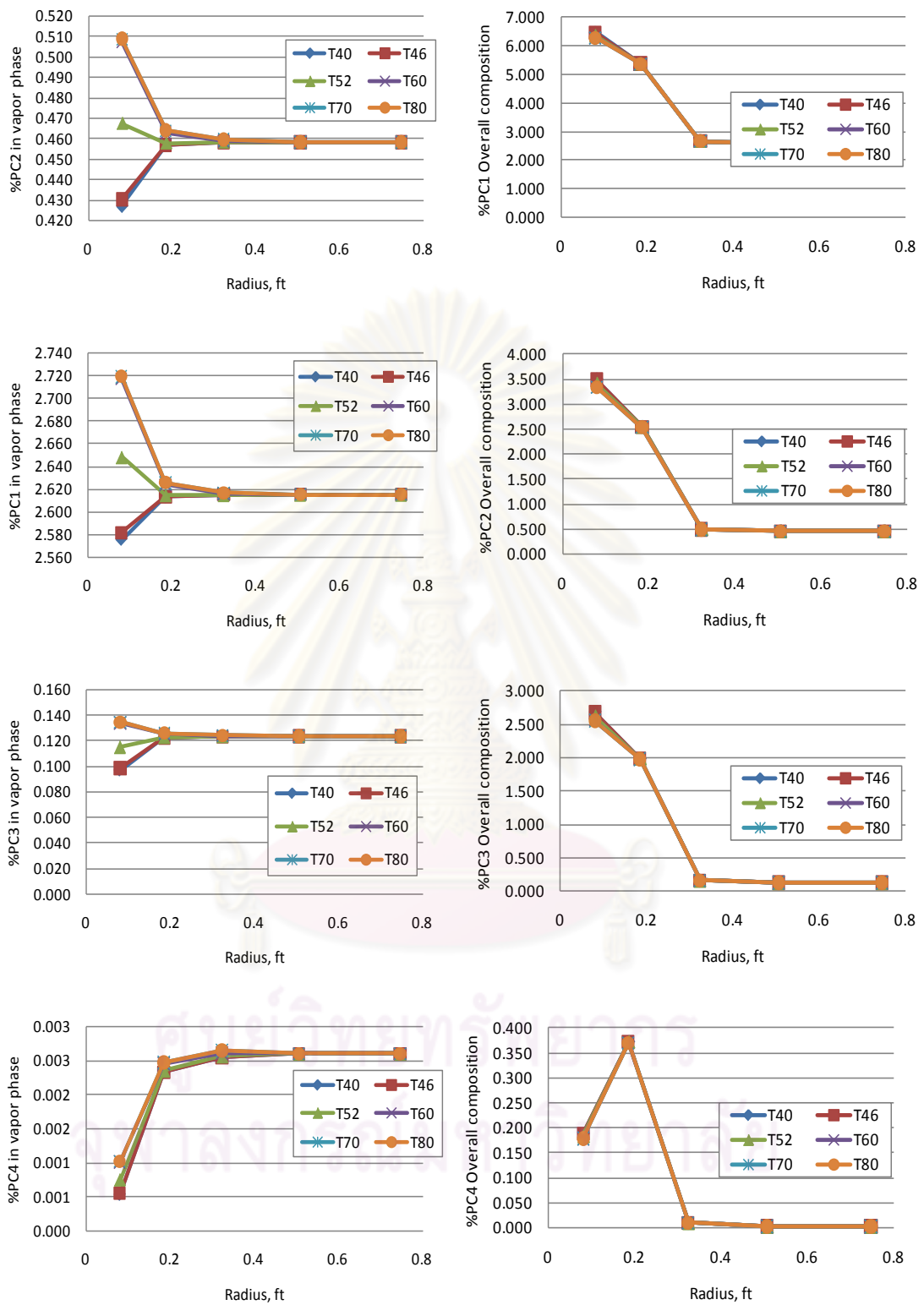


Figure C2: Compositions profile during build-up of Fluid A with 1 Mscf/d.(Continue)

APPENDIX D

Derivative Plot with an Analytical Model.

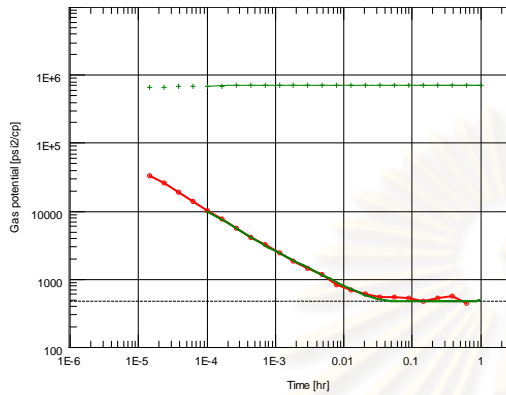


Figure D1: Derivative plot with an analytical model for case A-r1.

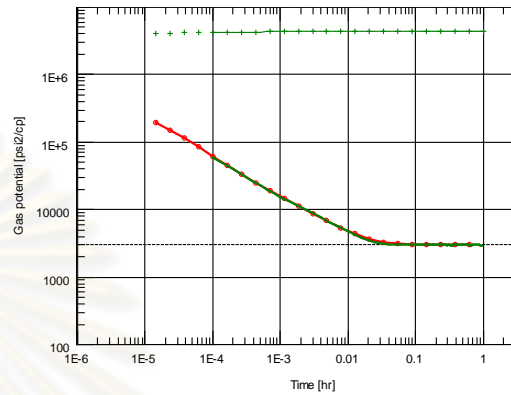


Figure D3: Derivative plot with an analytical model for case A-r3.

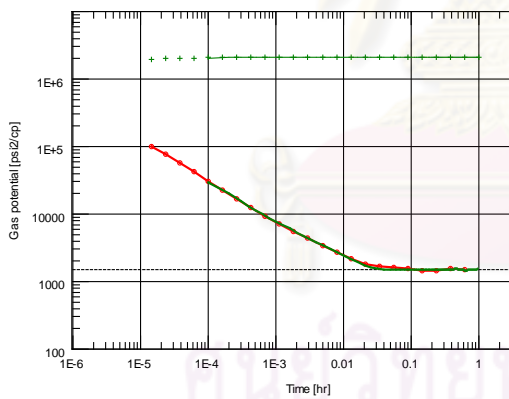


Figure D2: Derivative plot with an analytical model for case A-r2.

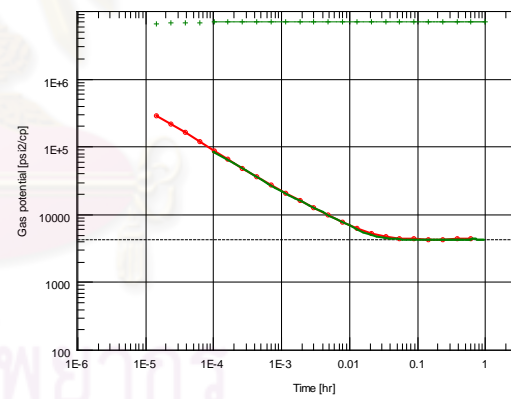


Figure D4: Derivative plot with an analytical model for case A-r4.

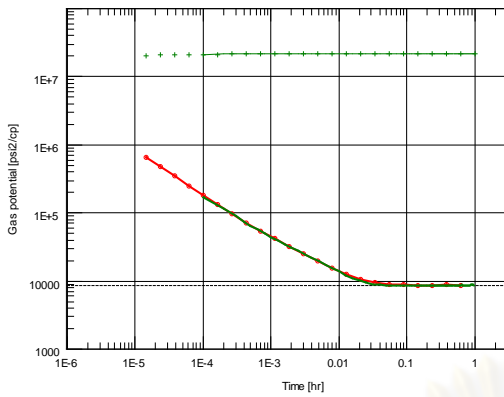


Figure D5: Derivative plot with an analytical model for case A-r5.

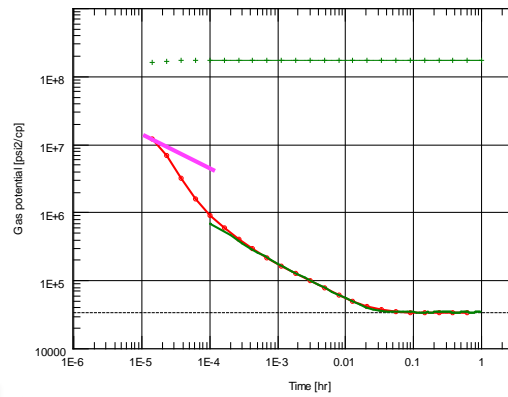


Figure D8: Derivative plot with an analytical model for case A-r8.

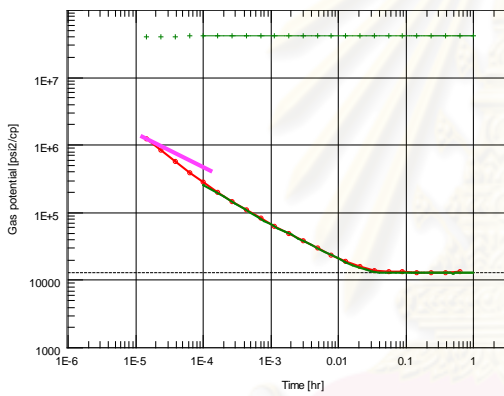


Figure D6: Derivative plot with an analytical model for case A-r6.

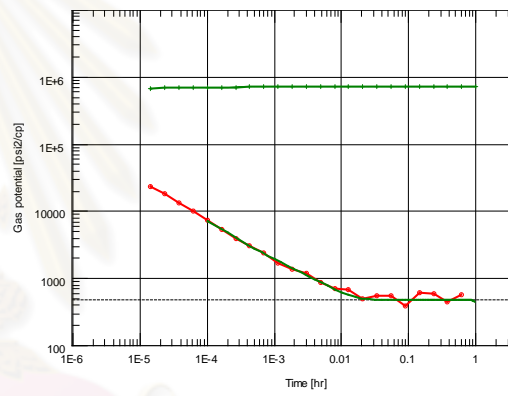


Figure D9: Derivative plot with an analytical model for case B-r1.

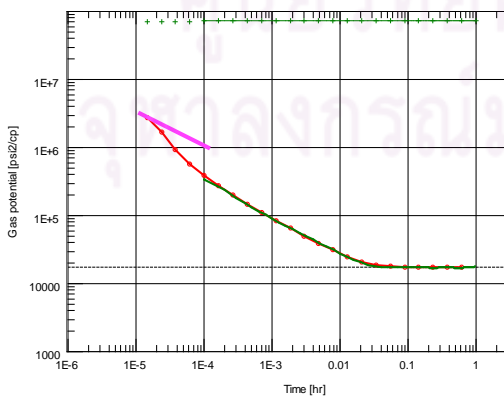


Figure D7: Derivative plot with an analytical model for case A-r7.

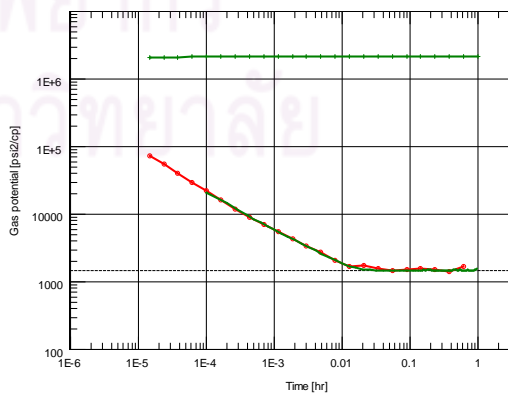


Figure D10: Derivative plot with an analytical model for case B-r2.

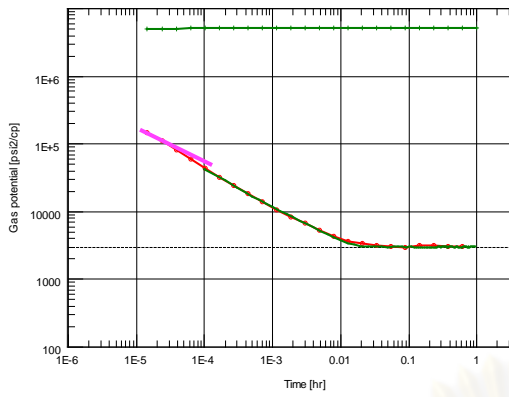


Figure D11: Derivative plot with an analytical model for case B-r3.

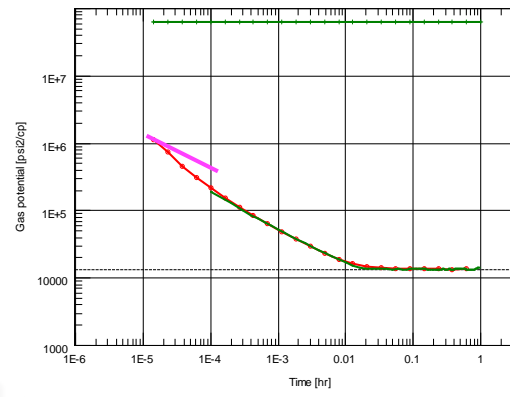


Figure D14: Derivative plot with an analytical model for case B-r6.

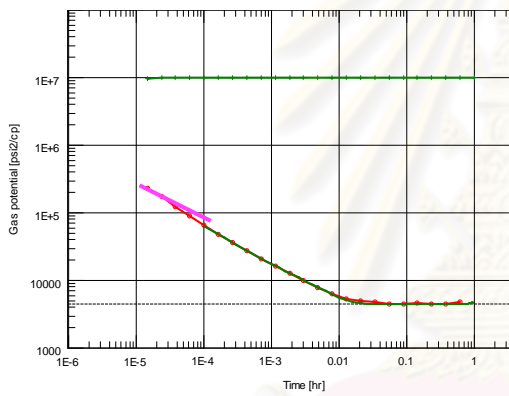


Figure D12: Derivative plot with an analytical model for case B-r4.

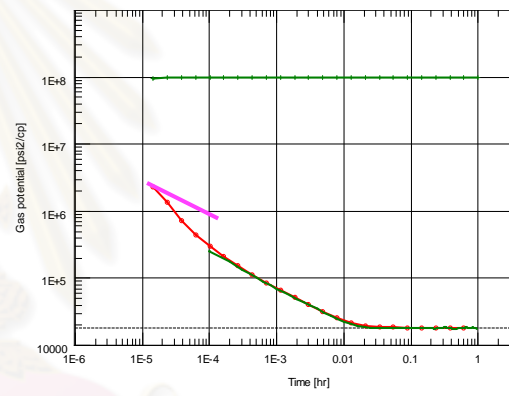


Figure D15: Derivative plot with an analytical model for case B-r7.

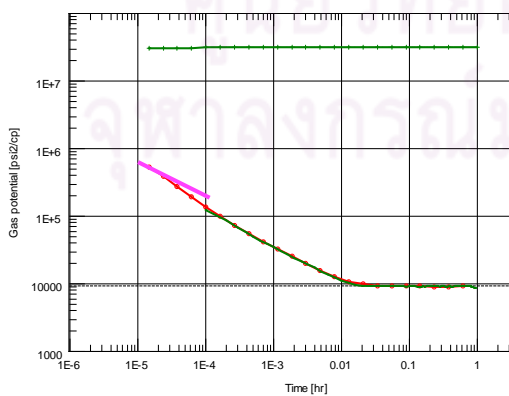


Figure D13: Derivative plot with an analytical model for case B-r5.

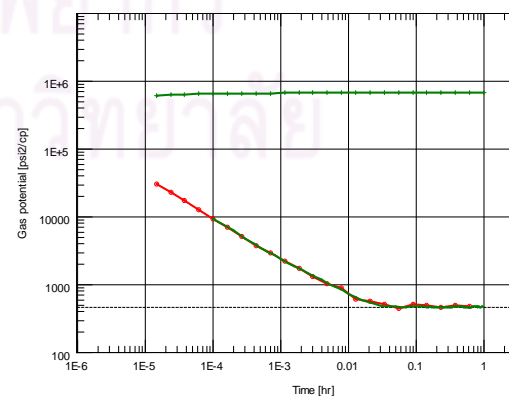


Figure D16: Derivative plot with an analytical model for case C-r1.

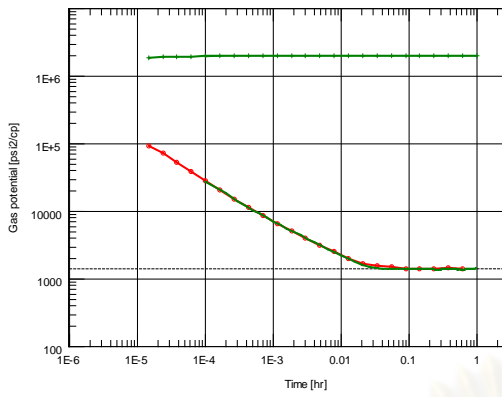


Figure D17: Derivative plot with an analytical model for case C-r2.

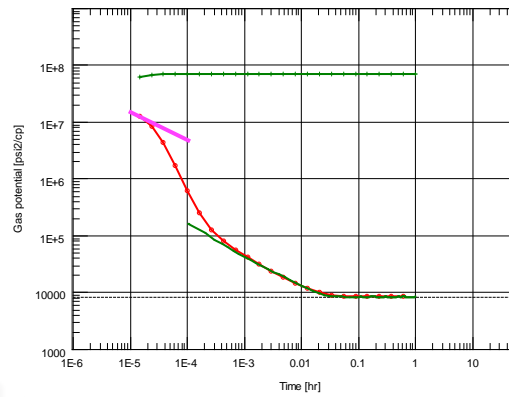


Figure D20: Derivative plot with an analytical model for case C-r5.

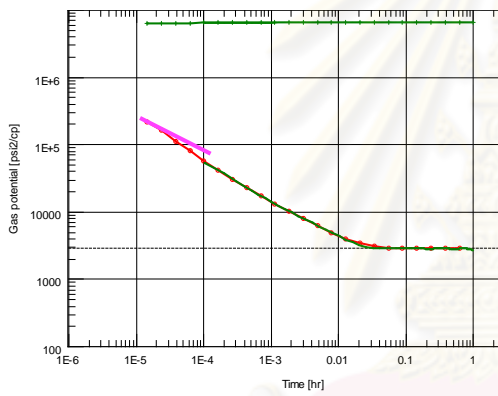


Figure D18: Derivative plot with an analytical model for case C-r3.

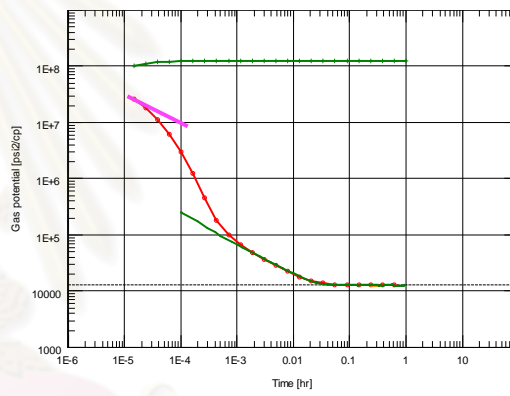


Figure D21: Derivative plot with an analytical model for case C-r6.

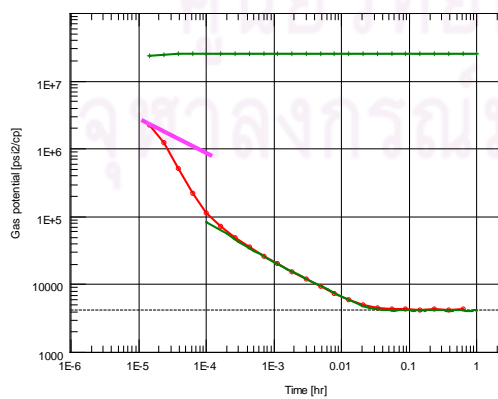


Figure D19: Derivative plot with an analytical model for case C-r4.

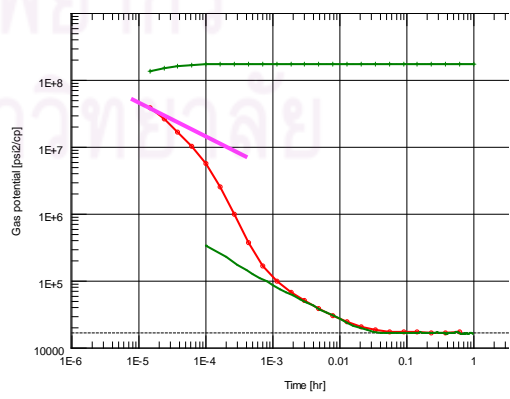


Figure D22: Derivative plot with an analytical model for case C-r7.

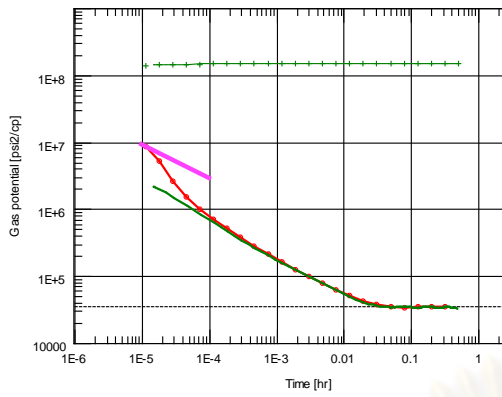


Figure D23: Derivative plot with an analytical model for case A-t1.

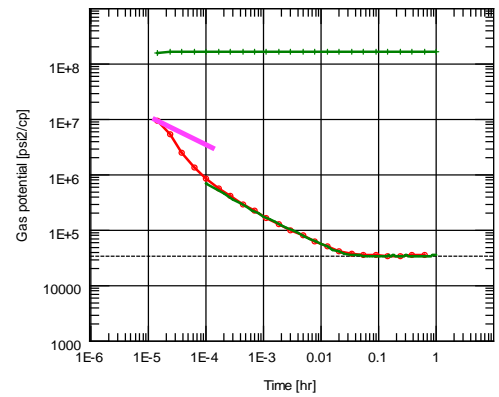


Figure D26: Derivative plot with an analytical model for case A-t4.

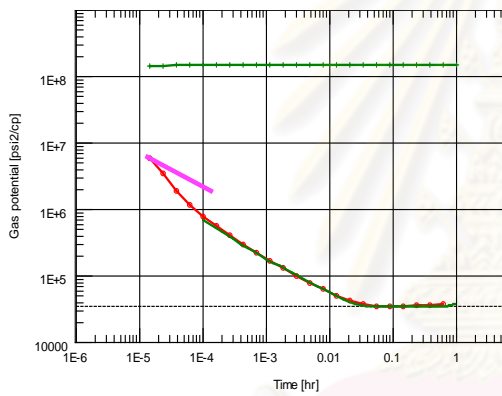


Figure D24: Derivative plot with an analytical model for case A-t2.

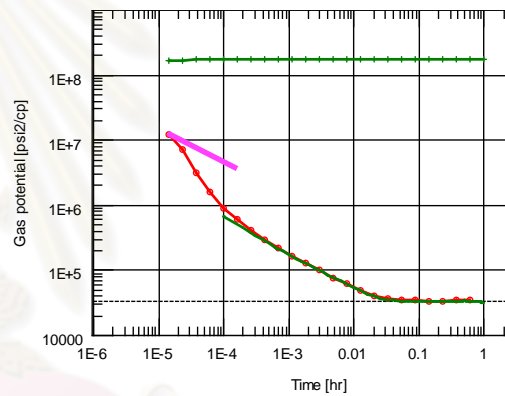


Figure D27: Derivative plot with an analytical model for case A-t5.

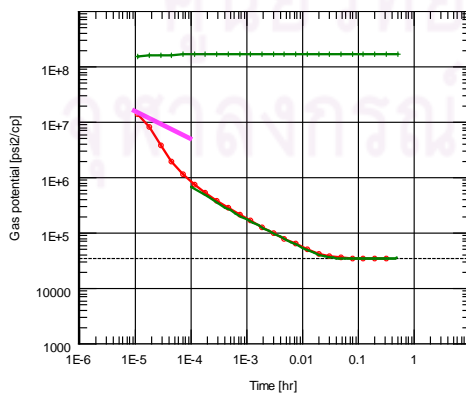


Figure D25: Derivative plot with an analytical model for case A-t3.

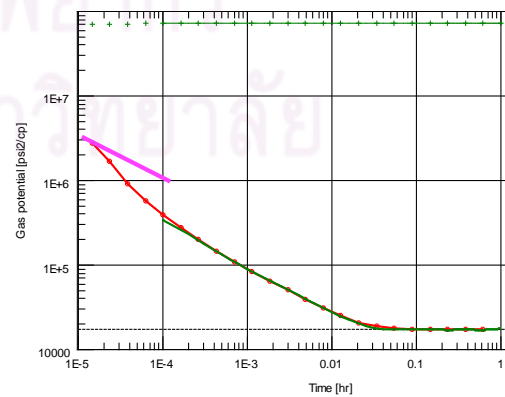


Figure D28: Derivative plot with an analytical model for case A-STD.

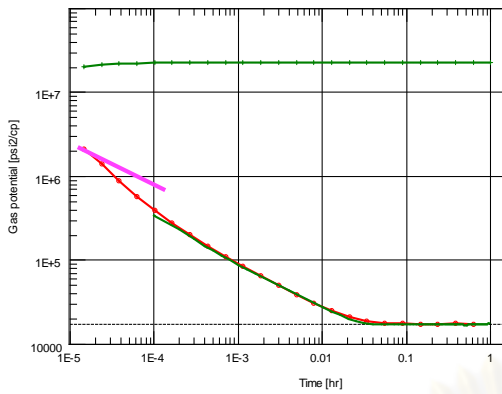


Figure D29: Derivative plot with an analytical model for case A-L.

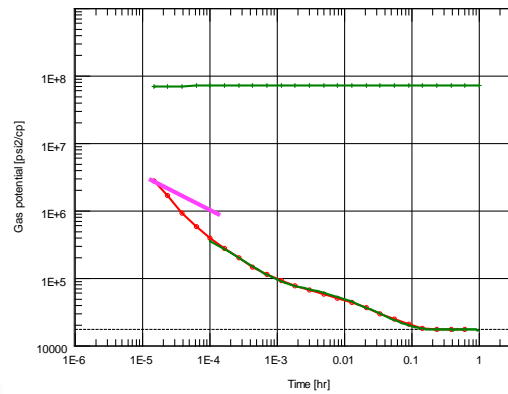


Figure D31: Derivative plot with an analytical model when the probe is set at 4 ft above the middle of the formation.

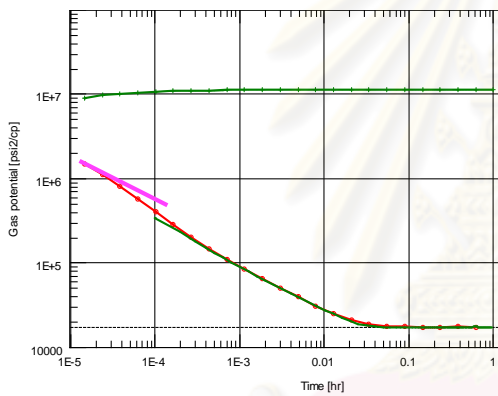


Figure D30: Derivative plot with an analytical model for case A-XL.

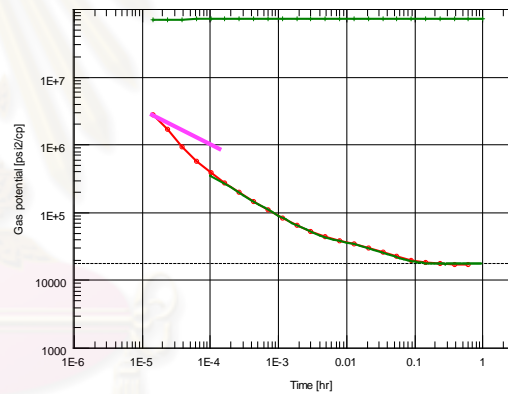


Figure D32: Derivative plot with an analytical model when the probe is set at 3 ft above the middle of the formation.

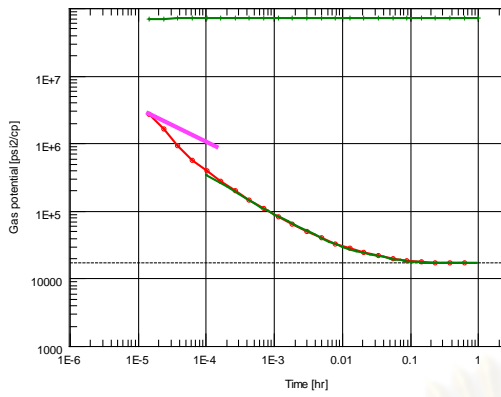


Figure D33: Derivative plot with an analytical model when the probe is set at 2 ft above the middle of the formation.

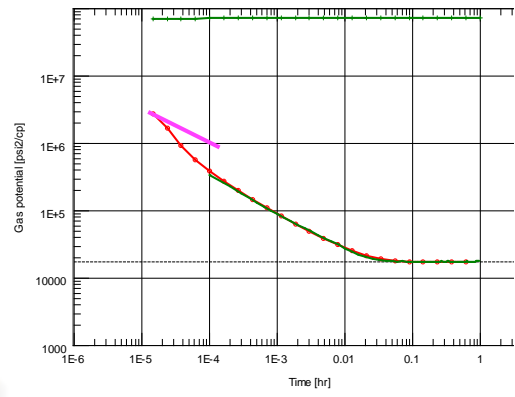


Figure D35: Derivative plot with an analytical model when the probe is set at 0.5 ft above the middle of the formation.

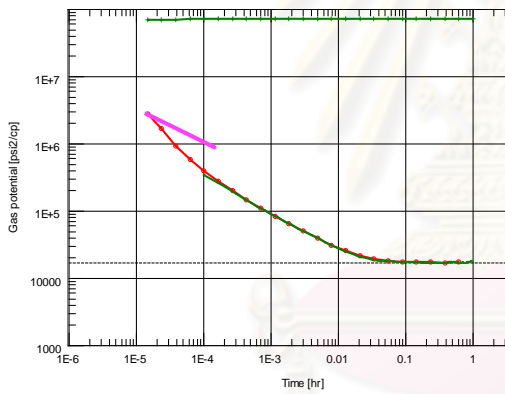


Figure D34: Derivative plot with an analytical model when the probe is set at 1 ft above the middle of the formation.

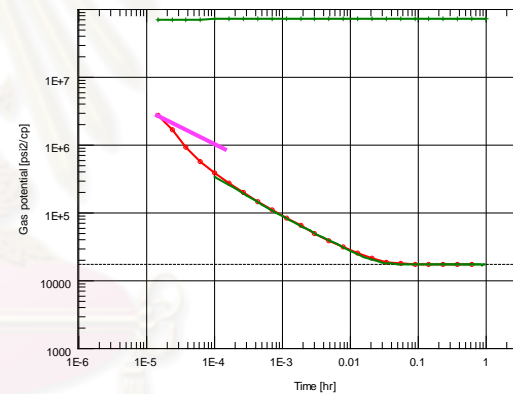


Figure D36: Derivative plot with an analytical model when the probe is set at 0.5 ft below the middle of the formation.

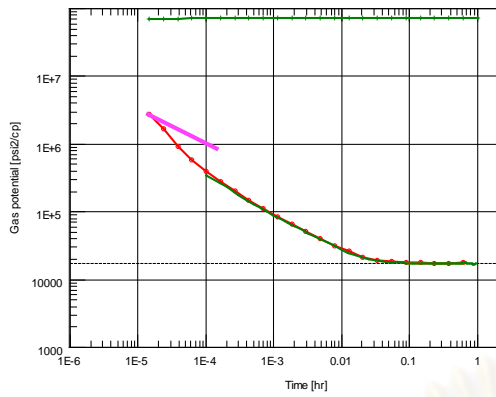


Figure D37: Derivative plot with an analytical model when the probe is set at 1 ft below the middle of the formation.

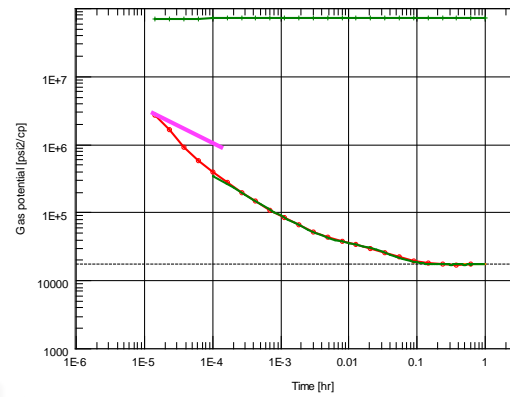


Figure D39: Derivative plot with an analytical model when the probe is set at 3 ft below the middle of the formation.

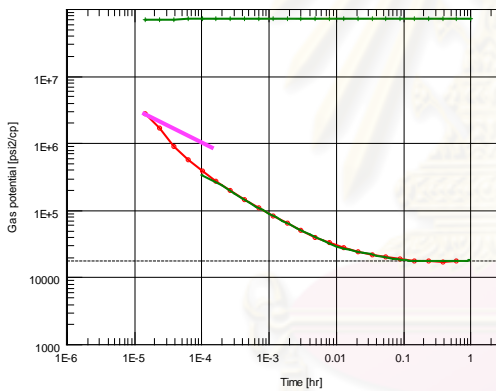


Figure D38: Derivative plot with an analytical model when the probe is set at 2 ft below the middle of the formation.

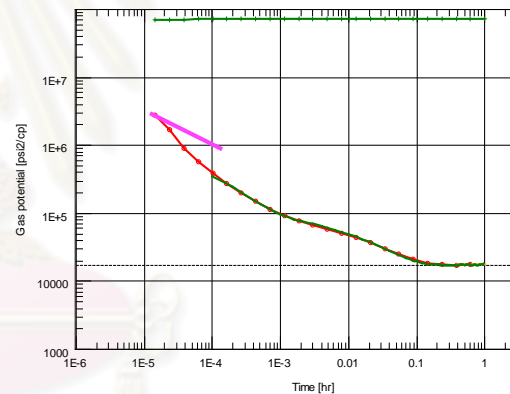


Figure D40: Derivative plot with an analytical model when the probe is set at 4 ft below the middle of the formation.

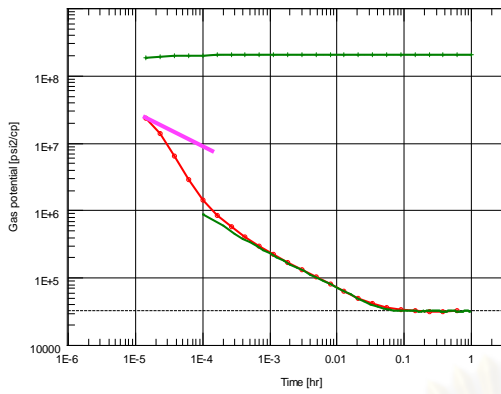


Figure D41: Derivative plot with an analytical model for case A-0.5kz.

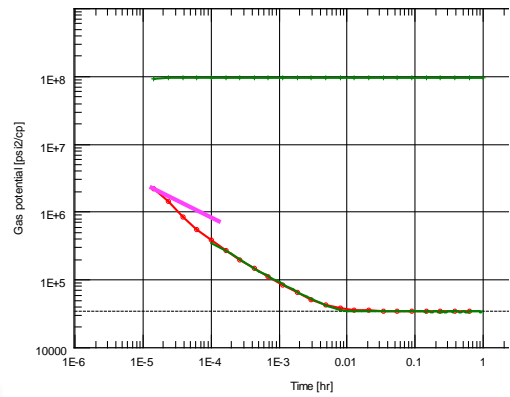


Figure D44: Derivative plot with an analytical model for case A-4kz.

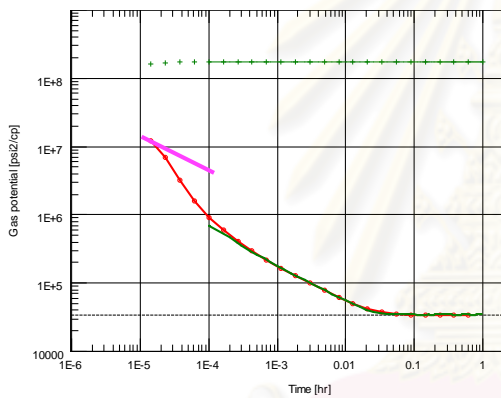


Figure D42: Derivative plot with an analytical model for case A-1kz.

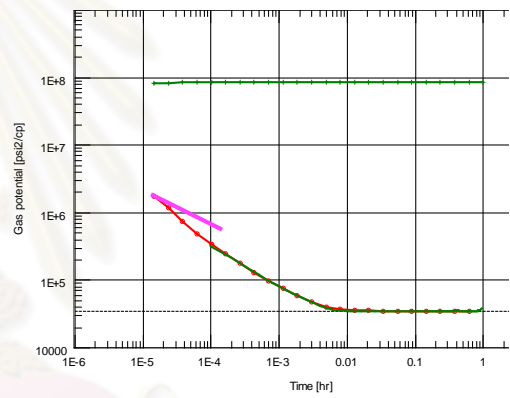


Figure D45: Derivative plot with an analytical model for case A-5kz.

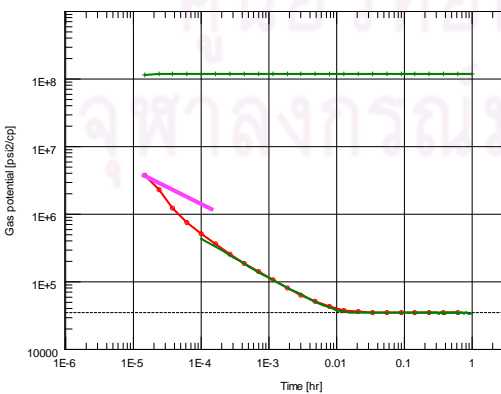


Figure D43: Derivative plot with an analytical model for case A-2.5kz.

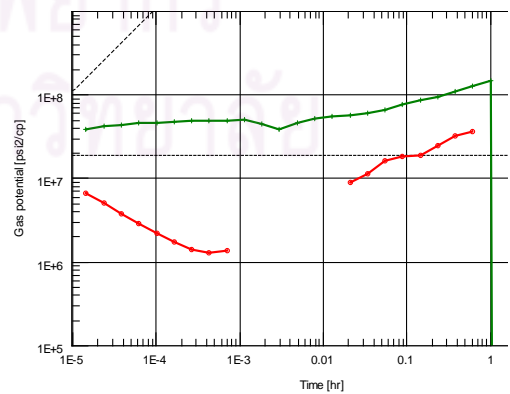


Figure D46: Derivative plot with an analytical model for case A-1k.

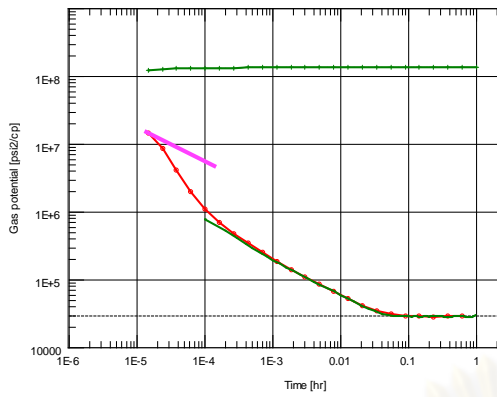


Figure D47: Derivative plot with an analytical model for case A-3k.

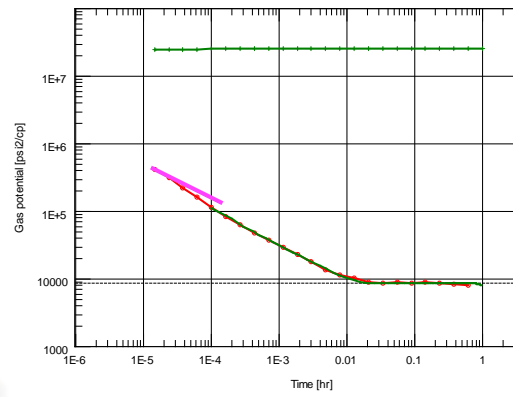


Figure D50: Derivative plot with an analytical model for case A-10k.

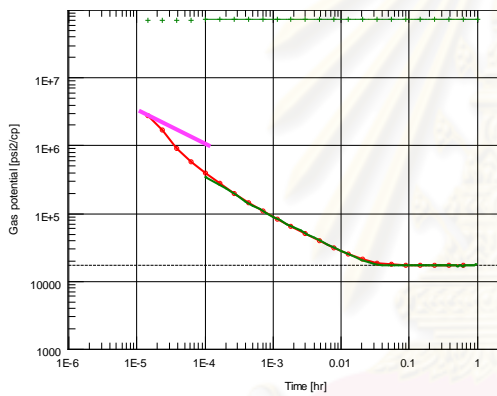


Figure D48: Derivative plot with an analytical model for case A-5k.

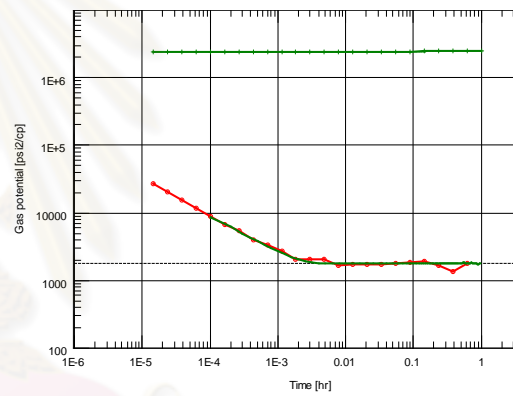


Figure D51: Derivative plot with an analytical model for case A-50k.

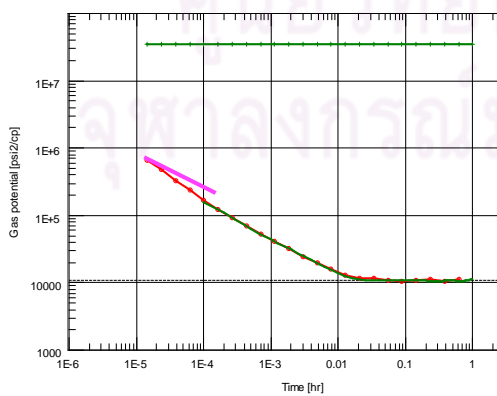


Figure D49: Derivative plot with an analytical model for case A-8k.

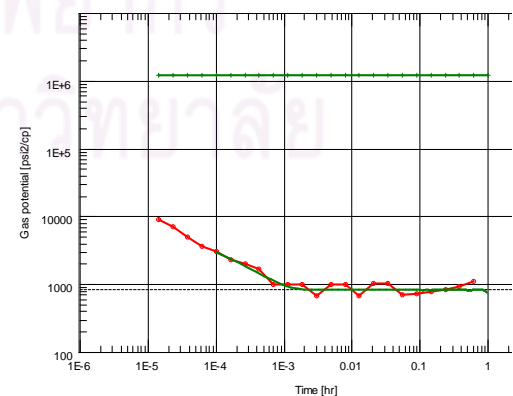


Figure D52: Derivative plot with an analytical model for case A-100k.

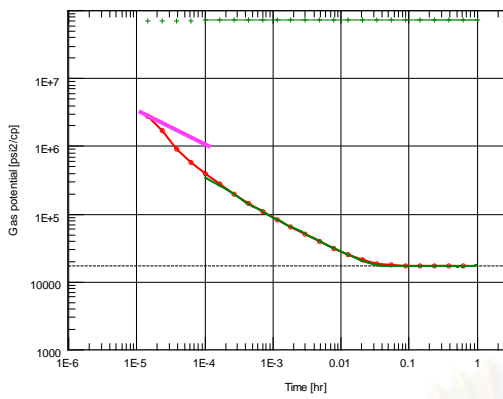


Figure D53: Derivative plot with an analytical model for case A-3474.

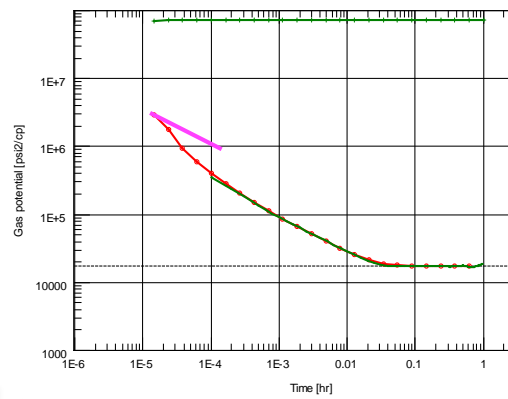


Figure D56: Derivative plot with an analytical model for case A-3400.

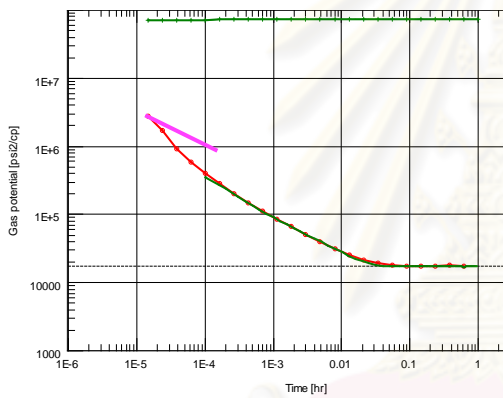


Figure D54: Derivative plot with an analytical model for case A-3468.

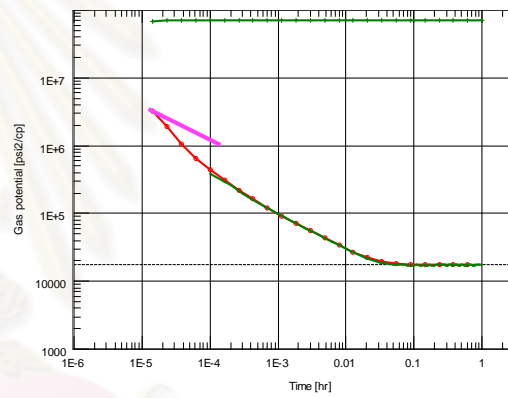


Figure D57: Derivative plot with an analytical model for case A-3000.

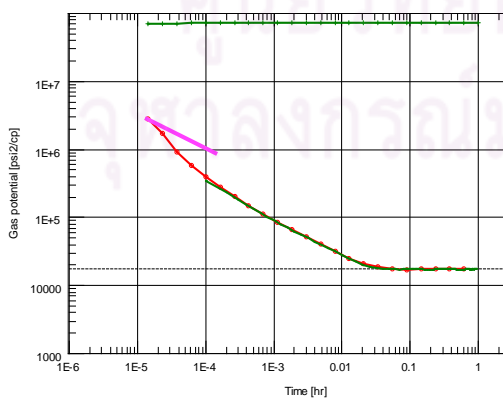


Figure D55: Derivative plot with an analytical model for case A-3460.

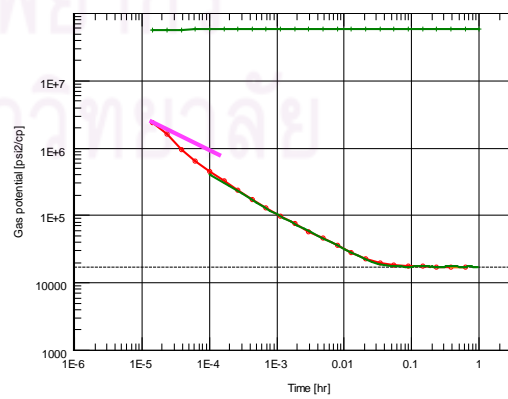


Figure D58: Derivative plot with an analytical model for case A-2600.

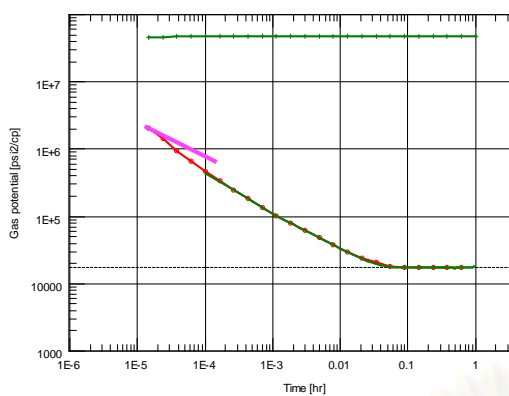


Figure D59: Derivative plot with an analytical model for case A-2200.

ศูนย์วิทยทรัพยากร
จุฬาลงกรณ์มหาวิทยาลัย

VITAE

Wisut Choknakawaro was born on December 18, 1985 in Nakhonpathom, Thailand. He received her B.Eng. in Petrochemical and Polymeric Materials Engineering from the Faculty of Engineering, Silpakorn University in 2007 with the 2nd class honors. After graduating, he continues his studies in the Master of Petroleum Engineering program at the Department of Mining and Petroleum Engineering, Faculty of Engineering, Chulalongkorn University.



ศูนย์วิทยทรัพยากร
จุฬาลงกรณ์มหาวิทยาลัย